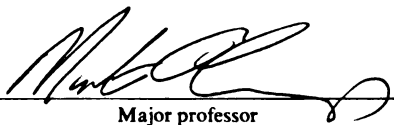This is to certify that the

dissertation entitled

STRUCTURAL STUDIES OF GMR MAGNETIC MULTILAYERS

AND SPIN-VALVES GROWN BY DC SPUTTERING

presented by

Hong Geng

has been accepted towards fulfillment
of the requirements for

___Ph.D.___ degree in _Materials Science_
and Engineering

_____
Major professor

Date _1/27/03_____

0-12771

PLACE IN RETURN BOX to remove this checkout from your record.
TO AVOID FINES return on or before date due.
MAY BE RECALLED with earlier due date if requested.

DATE DUE	DATE DUE	DATE DUE

STRUCTURAL STUDIES OF GMR MAGNETIC MULTILAYERS AND SPIN-VALVES GROWN BY DC SPUTTERING

By

Hong Geng

A DISSERTATION

Submitted to
Michigan State University
in partial fulfillment of the requirements
for the degree of

DOCTOR OF PHILOSOPHY

Department of Chemical Engineering and Materials Science

2002

ABSTRACT

STRUCTURAL STUDIES OF GMR MAGNETIC MULTILAYERS AND SPIN-VALVES GROWN BY DC SPUTTERING

By

Hong Geng

The structures and growth characteristics of sputtered GMR magnetic multilayers and spin-valves have been characterized using conventional and high resolution transmission electron microscopy (CTEM and HRTEM). The first part of this dissertation focused on the characterization of polycrystalline Cu/Py (permalloy™), Ag/Py, and Cu/CoZr spin-valves. For the Cu/Py spin-valves, structures with different Py thicknesses sputtered at different temperatures were examined. All of the spin-valves displayed polycrystalline structures with columnar grains. The grains grew on close packed planes ($\{111\}$ in the bcc Nb contacts and $\{110\}$ in the fcc Cu, FeMn, and Py spin-valve layers) taking up a near Kurdjumov-Sachs $\{111\}_{fcc}//\{110\}_{bcc};<110>_{fcc}//<111>_{bcc}$ orientation relationship. FFT analysis and HRTEM image simulations indicate that in some of the columnar grains, the Cu, FeMn, and Py regions take up non-equilibrium bcc structures, regardless of differences in layer thicknesses and sputtering temperatures. For the Ag/Py spin-valves, in addition to the expected polycrystalline morphology, in one instance an epitaxial single crystal Ag layer was discovered when the spin-valve was grown directly on a Si substrate. HREDS has shown that this single crystal (epitaxial) layer is likely composed of Ag and In in a 4:1 atomic ratio. In all of the other Ag/Py spin-valve samples, polycrystalline morphologies were consistently observed regardless of the substrate. For the Cu/CoZr spin-valves, CTEM observations of two spin-valves

revealed that both samples are polycrystalline with columnar grains similar to the morphologies observed in Cu/Py and Ag/Py spin-valves.

The second part of this dissertation is focused on determining the correct parameters for growing a high quality Cu buffer layer on an epitaxial Nb contact. CTEM observations demonstrate that the quality of epitaxial growth of Cu buffer layers depends strongly on deposition temperatures and post annealing. High quality epitaxial Cu buffer layers were obtained when the Cu layer was grown at low temperatures (100°C and 150°C) without post annealing. Diffraction patterns of multilayers show that twin variants appear in epitaxial Cu and Py layers, consistent with electron backscatter patterns (EBSP) results from thick films. HRTEM images reveal that the Cu buffer layer grown at 150°C appears as twin variants with two stacking sequences of {111} fcc planes. A three-layer periodic contrast observed in the Py layer can be rationalized based on overlapped twins along [110] with {111} twin planes.

TO MY PARENTS,

MY HUSBAND,

AND MY DAUGHTER.

ACKNOWLEDGMENTS

Michigan State University. I also want to extend my thanks to my husband's family, for caring about me.

TABLE OF CONTENTS

LIST OF TABLES

LIST OF FIGURES

xi

CHAPTER I

INTRODUCTION

Giant magnetoresistance (GMR) is a phenomenon in which the resistance of synthetic multilayers changes dramatically in response to an external magnetic field. The GMR effect has been the subject of intense investigation due to its already existing and potential technological applications for magnetic recording devices, magnetoresistive sensors, and magnetic random access memories. This effect is most usually observed in magnetic multilayered structures, where ferromagnetic layers (Fe, Co, NiFe) are closely separated by a non-magnetic layer of a noble metal (Cu, Ag, Au). GMR in magnetic multilayers has been found to be very sensitive to the layer structure and orientation, as well as to the interfacial roughness at the micro and atomic level. Therefore, it is critical to have a fundamental understanding of the details of the layer structures to facilitate the development of magnetic materials associated with GMR for field-sensing applications. This dissertation is an attempt to investigate the microstructures of magnetic multilayers using conventional and high-resolution transmission electron microscopy (CTEM and HRTEM) complemented with image simulations and fast Fourier transform (FFT) analysis. These techniques will be used to further characterize crystallographic epitaxy and texture, layer quality, interfacial roughness, defects, and any changes of microstructure, which can be correlated with the GMR effect.

1.1 THE GMR EFFECT

The GMR effect is the large relative change in resistance with applied external magnetic field in ultra-thin magnetic multilayers composed of alternating ferromagnetic and non-magnetic metallic layers. This effect is due to the quantum mechanical phenomena of spin-dependent scattering, which is a function of the relative orientation of the conduction electron spins and the magnetizations of the ferromagnetic materials.

Early studies of unusual magnetoresistive effects were reported by Pratt et al. in 1987 [1] with Ag/M (M=Fe, Ni, Co) layered structures and by Vélu et al. in 1988 [2] with $(Au/Co)_n$ multilayers. However, the first evidence of the GMR effect was discovered independently by two European research groups in the late 1980s: Baibich et al. [3] with single crystal Fe/Cr multilayers grown by molecular beam epitaxy (MBE) and Binasch et al. [4] with MBE-grown antiferromagnetically coupled single crystal Fe/Cr/Fe sandwiches. While working with large magnetic fields and thin layers of magnetic materials, both of these groups noticed very large resistance changes when these materials were subjected to external magnetic fields. Since these discoveries of the GMR effect, a new chapter has been opened up in understanding the fundamental science underlying the phenomenon of magnetism and magnetic materials. This progress also stimulated an interest in developing applications ranging from automotive sensors to information storage technology.

The most promising application of GMR in magnetic multilayers has been recording heads in magnetic storage devices, enabling greater storage densities and smaller head sizes [5,7]. IBM was the first company to announce GMR magnetic recording read heads in a family of disk drive products in 1997. These drives are capable

of reading extremely small magnetic bits at an areal density of 2.69 gigabytes per square inch. By the year 2001, densities of 10 gigabytes per square inch have been achieved [6]. Another important application of GMR is for magnetic field sensors. In 1994, Non-Volatile Electronics introduced the world's first products using GMR materials, a line of GMR magnetic field sensors that can be used for wheel speed and position sensing, magnetic media and current sensing [7]. Other important applications under study are the use of GMR materials for very low field sensing and magnetoresistive random access memory (MRAM), which is an integrated combination of non-volatile thin film magnetic storage and semiconductor support circuits for high density nonvolatile random access memory. GMR materials show promise to ameliorate one of the most difficult problems which has faced MRAM technology – that of a small signal level, leading to relatively long read access times for memory applications [8].

Conventional magnetoresistance materials such as Permalloy™ (NiFe) exhibit resistance changes at room temperature of just a few percent in magnetic fields of a few oersteds [9], whereas GMR multilayers show sensitivities five times greater than permalloy under the same field conditions [10,11]. Today, the vast majority of GMR studies are devoted to researching magnetic multilayered structures that show large sensitivities in low external fields at room temperature.

1.1.1 Origin of the GMR Effect:

The origin of the GMR effect has been theorized to be the spin-dependent scattering of conduction electrons at ferromagnetic(F)/non-magnetic(N) interfaces and in bulk F layers [3,12]. It is well known that electrons can exist in two quantum states: *spin*

3

up if their spin is parallel to the magnetic field and *spin down* if their spin is anti-parallel to the magnetic field. Electron scattering at the F/N interfaces depends on whether the electron spin is parallel or anti-parallel to the magnetic moment of the magnetic layers. Figure 1.1 illustrates this mechanism for two magnetic states: (a) parallel state (P) with F layer magnetizations parallel to each other and (b) anti-parallel (AP) state with F layer magnetizations anti-parallel to each other. The resistance of the magnetic multilayers can be altered by changing the orientations of the magnetic moments of the F layers to be either parallel or anti-parallel to each other. It is observed that the resistance of the structure is much higher when the magnetic moments of the adjacent magnetic layers are aligned anti-parallel than when they are parallel. Switching from the antiparallel to the parallel configuration can be achieved by applying a magnetic field. This effect is called giant magnetoresistance (GMR), and commonly expressed as a percentage of $\Delta R/R_{sat}$ [13] as shown in figure 1.2.

1.1.2 GMR Measurements

The GMR effect is usually measured with a geometry of electric current flowing in the layer planes (CIP) of the multilayer [3,14], as shown in figure 1.3 (a). With a CIP measurement, it is difficult to separate the bulk and interface contributions to GMR, because the current paths are randomly distributed throughout the interfaces and bulk materials. Measurement of GMR with a geometry of the current flowing perpendicular to the layer planes (CPP) through magnetic multilayers was pioneered by a group at MSU [15] and is shown in figure 1.3 (b). CPP is an advancement over CIP because it allows quantitative determinations of the parameters describing the spin-orientation dependent

(a) P state   (b) AP state

✸ Electron scattering occurred
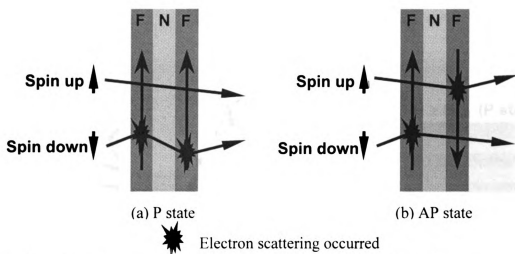
Figure 1.1 Schematic representation of the mechanism of spin-dependent scattering for two magnetic states: (a) parallel (P) state with the F-layer magnetizations parallel to each other; (b) anti-parallel (AP) state with the F-layer magnetizations anti-parallel to each other.

H = 0 (AP

H ≥ H_sat (P state)

H ≥ H_sat (P state)

$\Delta R/R_{sat}$ (100%)

H (KOe)

$$\Delta R/R_{sat} = MR\% = 100 \times [R(AP) - R(P)]/R(P)$$
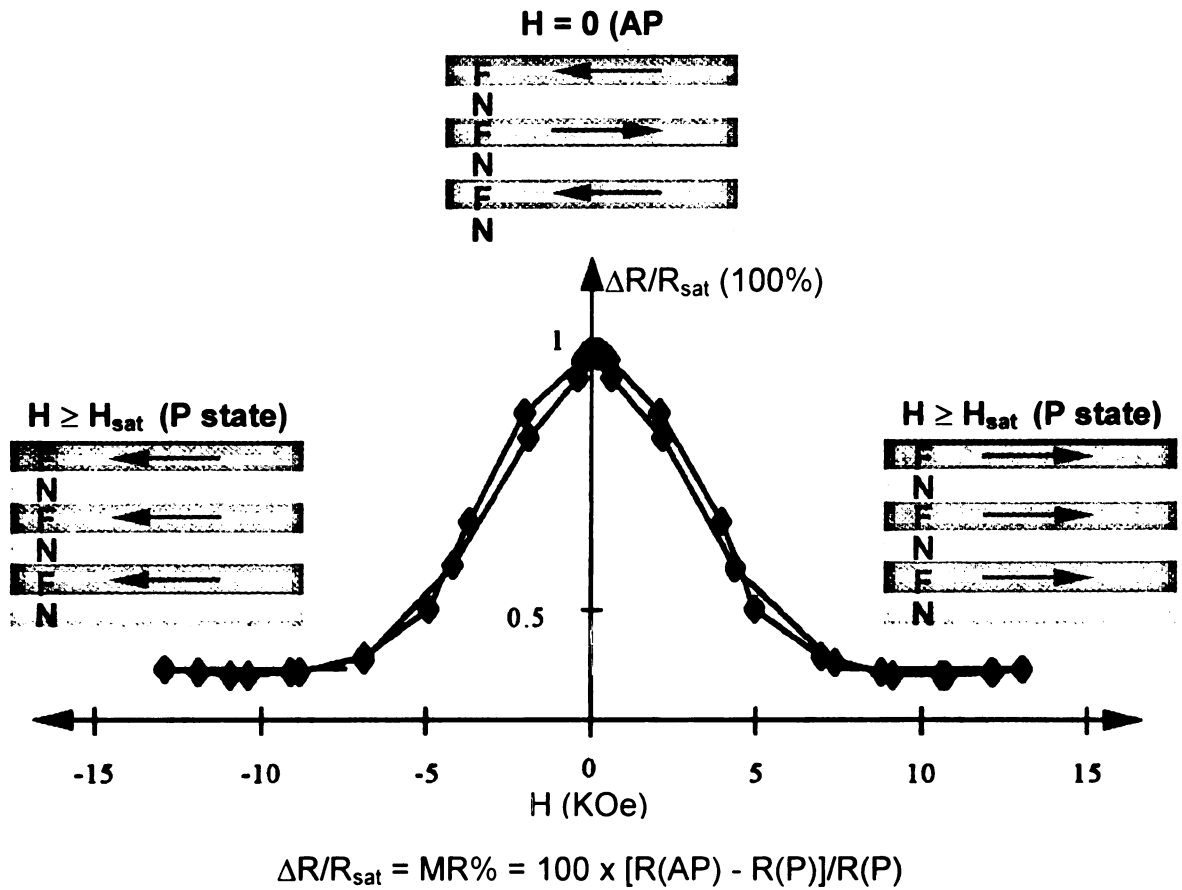
Figure 1.2 A representation of the anti-parallel (AP) and parallel (P) configurations of the ferromagnetic (F) layer moments and the magnetic field dependence of the GMR for a Co/Cu multilayer sample at the first antiferromagnetic coupling peak.
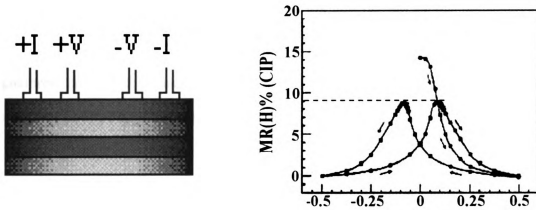
(a) CIP configuration and CIP-MR in a (Co/Ag) magnetic multilayer
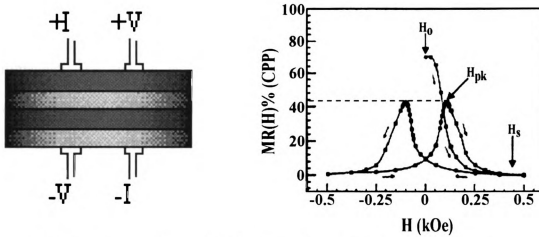
(b) CPP configuration and CPP-MR in a (Co/Ag) magnetic multilayer

Figure 1.3 Schematic diagrams of the (a) CIP and (b) CPP configurations and corresponding examples of the GMR measurements in a (Co/Ag) magnetic multilayer. CPP-MR=45% > CIP-MR=9% [15].

electron scattering in the F layers and at the F/N interfaces. In CPP measurements, superconducting Nb contacts are used as current and voltage leads to ensure uniform current density through the multilayer from the top and bottom of the multilayers. A primary difference between measurements in the two configurations is that the magnetoresistance (MR) is usually greater in a CPP sample than that in a corresponding CIP sample, i.e. CPP MR > CIP MR.

1.2 GMR MAGNETIC MULTILAYERS AND SPIN-VALVES

The GMR effect was first observed in single crystal Fe/Cr multilayers grown by MBE [3] and in polycrystalline Fe/Cr structures grown by the much simpler technique of magnetron sputtering [16]. These types of the multilayers consist of alternating ferromagnetic (Fe) and non-magnetic (Cr) layers. Initially, with a low external field, the magnetic moments of the Fe layers are aligned in an anti-parallel (AP) state to minimize the energy. When a saturating magnetic field is applied, the magnetic moments of the Fe layers are aligned along the field direction (parallel magnetic moments). The maximum GMR effect for this arrangement was observed with single crystal (001)Fe/(001)Cr multilayers of 30 Å and 9 Å thicknesses respectively in a magnetic field at 20kOe as shown in figure 1.4; similar results were also observed in polycrystalline Fe/Cr structures. These experiments also revealed that GMR can be observed in a wide variety of magnetic systems such as Co/Cu [17,18], Fe/Cu [19], NiFe/Cu [18,20], and NiFe/Ag [21] multilayers, and the largest magnetoresistance effect has been observed in Co/Cu based structures [22].

8

Due to the requirement of a high magnetic field to align the magnetic moments parallel to each other (for example: 20 kOe for single crystal Fe/Cr multilayers as shown in figure 1.4), an alternative GMR arrangement, known as the exchange-biased spin-valve (EBSV) configuration, was invented by Dieny et al. [23]. This configuration is desirable because of its high sensitivity in a low magnetic field. Due to this feature, these structures have generated a high level of interest as existing and potential candidates for use in magnetic recording heads of the next generation of hard disk drives in computers.

The typical EBSV structure is in the form of F/N/F/AF [24], which consists of two ferromagnetic (F) layers separated by a non-magnetic (N) layer. An additional anti-ferromagnetic (AF) material is provided either on the top or on the bottom of the trilayer to couple to the adjacent F layer and pin the moment of this layer in a fixed direction. The other F layer is free to rotate in small fields, as shown in Fig. 1.5 [9,10,23,25-32]. This arrangement allows the magnetic moments to be easily switched between parallel and anti-parallel configurations. Another type of spin-valve, the hybrid spin-valve, was also studied. Hybrid spin-valves differ from EBSVs, in that the anti-ferromagnetic materials are no longer needed. This type of spin-valve uses either different thickness of the same type of ferromagnetic layer or different ferromagnetic materials to enable the magnetization of both ferromagnetic layers to be rotated independently [33]. This dissertation will mainly focus on spin-valve structures.

1.3 CORRELATION BETWEEN GMR AND MULTILAYER STRUCTURES

With the size of magnetic devices becoming smaller and smaller (typical dimensions of the single layer thickness are in the nanometer range), there is a greater
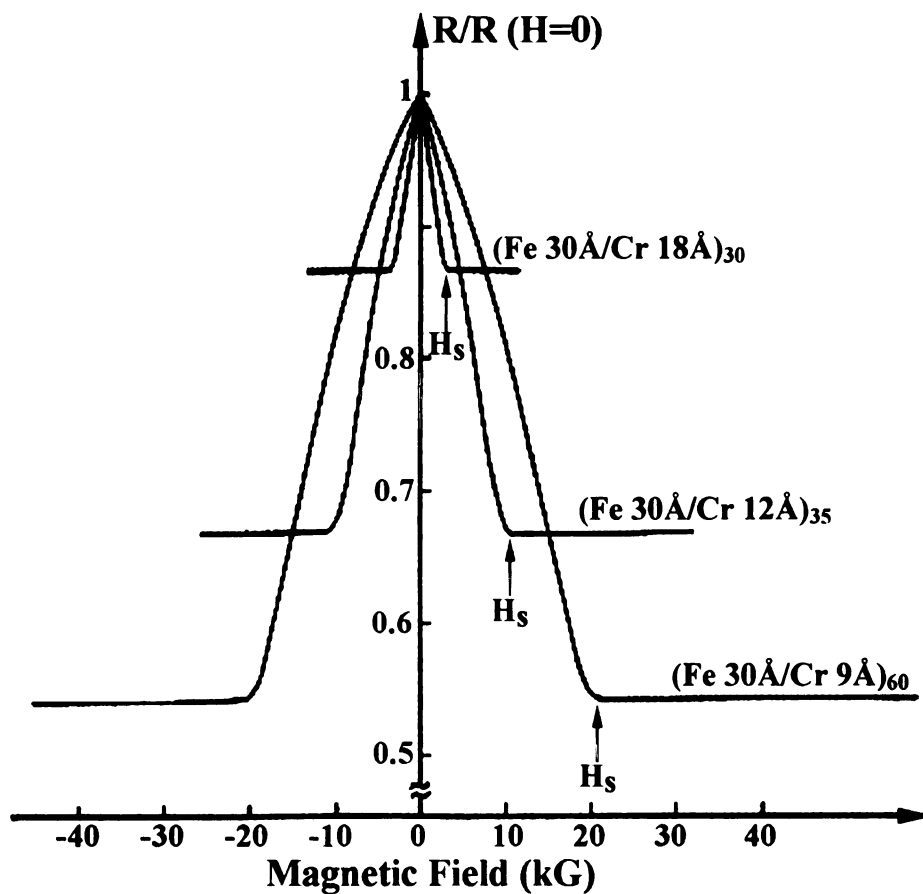
Figure 1.4 The first discovery of the giant magnetoresistance phenomena in single crystal Fe/Cr superlattice. The maximum GMR was observed with (Fe 30Å /Cr 9 Å)$_{60}$ superlattice [3].
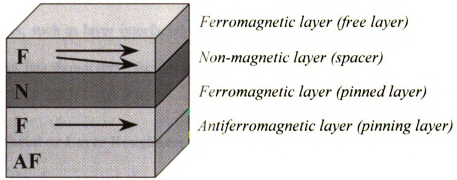
(a)
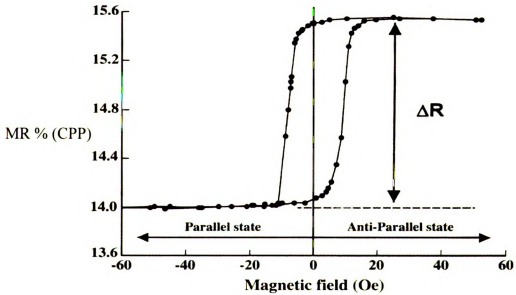
(b)

Figure 1.5 Schematic representation of (a) an EBSV structure and (b) the magnetoresistance response of a spin-valve $[NiFe_{24}/Ag_{20}/NiFe_{24}/FeMn_8]_{nm}$ (NiFe-denoted as Py) [34].

interest in establishing the correlation between the structures of magnetic multilayers/spin-valves and the GMR effect. For example, it has been found that the GMR effect varies with layer thickness [29]. A broad range of studies on microstructures, such as layer interfacial roughness, layer quality, crystal orientation, and layer thickness, has shown these factors to have important relations with the GMR effect.

1.3.1 Interfacial or Layer Roughness

Since the discovery of the GMR effect in magnetic multilayers or spin-valves, numerous observations have indicated that interfacial roughness plays a significant role in the GMR effect [31,35-41]. Some studies conclude that in (Fe/Cr) and (Co/Cu) multilayers, the interfacial roughness produces very strong spin-dependent scattering of conduction electrons and therefore tends to increase GMR [40]. In contrast, in (NiFe/Cu) multilayers or spin-valves, the interfacial spin-dependent scattering appears to be not as critical as the bulk scattering, and that an increase in the interfacial roughness was observed to lead to a systematic decrease in GMR [31,36]. Recently, a quantitative structural study of Fe/Cr superlattices showed that the interfacial or layer roughness is correlated and increases cumulatively with the number of the bilayers [37] as shown in figure 1.6 and with sputtering pressure [38] and as shown in figure 1.7 (a) and (b); the GMR were also increased with both factors. Reports from different groups on the correlation between the interfacial roughness and GMR effect are not conclusive and require further theoretical and experimental investigation [39-41].

1.3.2 Layer Quality

Another variable influencing the GMR effect is the crystallographic quality of the
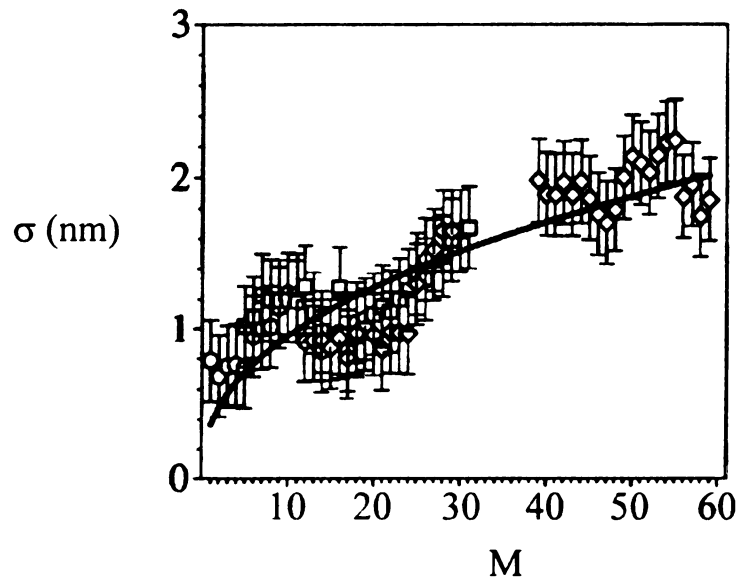
Figure 1.6 The quantitative roughness of each individual Cr layer inside a series of superlattices [Fe(3nm)/Cr(1.2nm)]$_N$ with the number of the bilayers N = 20, 40, and 60. Roughness of each individual bilayer as a function of the bilayer index M for N = 20 (o), N = 40 (□), and N = 60 (◊). σ represents the roughness. Note that the roughness increases with the bilayer index [37].

(a)   **(b)**
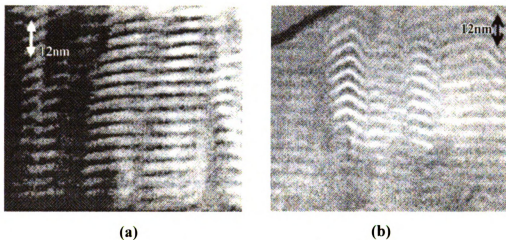
Figure 1.7 Cr mapping taken on [Fe(30Å)/Cr(12Å)]×20 multilayer grown at (a) 4 mTorr and (b) 10 mTorr showing the layer roughness increased with sputtering pressure [38].

overall multilayered structure and in particular of the interfaces. Some studies have reported that high-quality Co/Cu multilayer structures grown on Fe buffer layers result in high GMR, as shown in figure 1.8 [42]. Other studies state that Fe(001) and Cr(001) have similar bulk crystallographic structures (bcc), with lattice parameters of 2.88 and 2.87 Å. This good crystallographic matching allows for the epitaxial growth of (Fe/Cr) multilayers, and in turn leads to a larger GMR amplitude, although Fe and Cr tend to interdiffuse to one or two monolayers at the interfaces [43]. Lower GMR has been observed in Fe/Cu systems due to the different bulk crystal structures of these two elements (bcc vs. fcc) [44].

1.3.3 Crystal Orientation or Growth Direction

Using x-ray diffraction techniques, Nakatani et al. [45,46] found that the preferred orientation of the multilayer changes with the thickness of the non-magnetic material in certain magnetic multilayers. They reported that the highest GMR ratios are obtained when the orientation is <100> in NiFe/Cu multilayers grown by ion beam sputtering on a Si (100) substrate. Pardavi-Horvath [13] has also been established that certain orientations of the non-magnetic layers are related to the observed GMR effect. Jungblut et al. [47] found that the exchange-biasing field and coercive field strongly depend on the crystal orientation for highly oriented MBE grown NiFe/FeMn exchange-biased spin-valves.

1.3.4 Layer Thickness

The dependence of the GMR effect on layer thickness in various multilayer
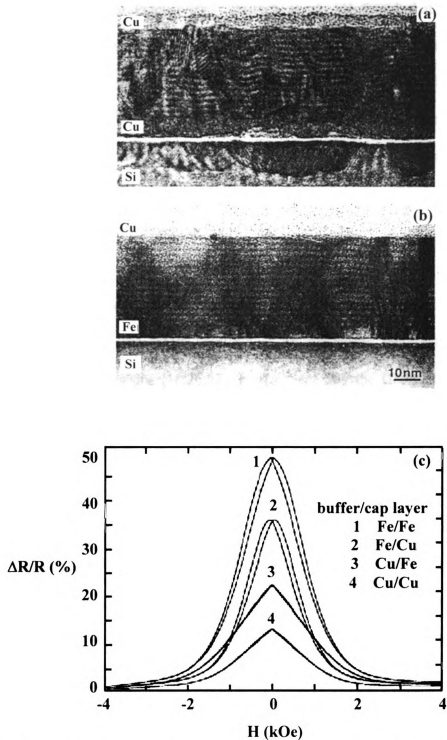
Figure 1.8 Cross-section transmission electron micrographs of (a) Si//[Cu/(Co/Cu)$_{16}$/Cu] with Cu buffer layer and (b) Si//[Fe/(Co/Cu)$_{16}$/Cu] with Fe buffer layer, which show considerable waviness and buckling of the layers in (a) and comparatively smooth and flat layers in (b). (c) An illustration of the relationship between GMR and Co/Cu superlattices [42]. Note that the Co/Cu grown on the Fe buffer layer has a much larger magnetoresistance, indicating high-quality structure results high GMR value.

systems has been studied extensively. Baibich et al. [4] found that the GMR of antiferromagnetically coupled Fe/Cr multilayers decreases with increasing the non-magnetic Cr thickness. The variation of GMR with the magnetic layer thickness was also studied. Dieny et al. [29] demonstrated that the magnetoresistance amplitude always shows a maximum when the thickness of the magnetic layers is varied from a monolayer thickness to a few tens of angstroms (Å). It has also been shown that grain or column size increases with increasing layer thickness [29].

1.3.5 Growth and Deposition Conditions

The variation of the GMR amplitude with deposition temperature has been investigated by various groups [18,26,27,48,49]. Generally the GMR effect decreases monotonically with increasing temperature. Experiments by W.F. Egelhoff Jr. et al. [50] have shown that the GMR effect in Co/Cu/Co spin-valves was 14% for a growth temperature of 150 K, 10% for a growth temperature of 300 K, and 0% for a growth temperature of 450 K.

As discussed previously, the GMR effect is critically affected by interfacial roughness. Further studies have shown that roughness depends strongly on growth conditions and deposition parameters [51]. This topic is still not yet well understood, mainly due to the non-thermodynamic growth conditions of most deposition techniques.

1.4 CHARACTERIZATION TECHNIQUES

There are a number of characterization techniques that have been applied to study the microstructures of magnetic multilayers and spin-valves. X-ray diffraction (XRD) is

most commonly used to determine structural information averaged over multilayer structures [35,45,46]. Reflection high-energy electron diffraction (RHEED) is utilized for determining the growth features of magnetic multilayers [52,53]. More recently, electron backscattered patterns (EBSP) have begun to be used for measuring crystallographic orientations of the magnetic materials [54]. Additional details about the surface roughness morphology is available from atomic force microscopy (AFM) [55] and scanning tunneling microscopy (STM) [56]. Other techniques, such as low-energy electron diffraction (LEED) [57], high-resolution energy dispersive x-ray spectroscopy (HREDS) [58], and X-ray absorption fine structure (XRAFS) spectroscopy [59], have also been performed.

Cross-sectional transmission electron microscopy including conventional and high-resolution transmission electron microscopy (CTEM and HRTEM) was the primary tool used to investigate the structural information in this thesis [60-62]. The main advantage of using cross-sections instead of planar sections is that it allows investigation of interface structures between the layers, or any changes in orientation and new phases that may be present. CTEM images can provide useful information about overall layered microstructures and has been used to characterize microstructural features of the multilayers, such as the uniformity of the layers, grain or crystallite size, the orientation and texture of the grains, and the propagating roughness of the layers as a function of growth. Additional details about microstructural features at the atomic level are available from high-resolution transmission electron microscopy (HRTEM). When complemented with image simulations and fast Fourier transform (FFT) image analysis techniques, HRTEM has the ability to extract accurate structural information concerning crystal

structures and interplanar spacings [63]. To get additional analytical information energy dispersive x-ray spectroscopy (EDXS) and electron energy loss spectroscopy (EELS) have also been used [58].

1.5 OBJECTIVES OF THIS RESEARCH

It is known that the GMR effect in magnetic multilayers and spin-valves depends on structure at the micro and atomic level, where interfacial or layer roughness, layer quality, and layer orientation are important factors. Therefore, the initial objective of this study was to characterize the interfacial structures of polycrystalline spin-valves using cross-sectional CTEM and HRTEM.

Polycrystalline Cu/Py and Ag/Py multilayers and spin-valves were first studied. In the Cu/Py spin-valves, non-equilibrium bcc structures appeared in addition to the equilibrium fcc Cu, FeMn, and $L1_2$ Py structures in the layers. In one of the Ag/Py spin-valves, the first Ag layer grew as an epitaxial single crystal although the remaining layers displayed the expected polycrystalline morphology. It was found that indium contamination existed in this sample when the spin-valve was grown directly on the Si substrate.

Because of the non-equilibrium phases that were found in polycrystalline Cu/Py and Ag/Py multilayers and spin-valves, and because of the difficulties in imaging interfaces in polycrystalline samples, the initial objective of this study was modified to focus on the interfacial structures in epitaxial multilayers which diminishes the effects of structural defects associated with grain boundaries. However, as the program progressed, it became clear that growing such samples was not a trivial matter. Thus, the final

objective of this study was to assess the structures of samples grown to be epitaxial. Through an iterative process, success has now been achieved in growing smooth epitaxial samples using a sputter deposition technique.

CHAPTER II

EXPERIMENTAL PROCEDURES

2.1 GMR MATERIALS AND FABRICATION:

The magnetic multilayers and spin-valves described in this study were fabricated by Dr. Reza Loloee of the department of Physics and Astronomy at Michigan State University. Details of the fabrication system and sputtering procedures have been described elsewhere [33]. Two sets of multilayer/spin-valve samples were produced by d.c. magnetron sputtering: one set included as-grown polycrystalline multilayers and spin-valves sputtered onto Si substrates; the other set included attempts to grow epitaxially multilayers and spin-valves on sapphire (Al_2O_3) substrates.

2.1.1 Polycrystalline Multilayers/Spin-Valves And Fabrication

All of the polycrystalline multilayer/spin-valve samples were sputtered onto the Si substrates in the temperature range of –67°C to +56°C as shown in table 2.1. Figure 2.1 shows the duplex design [15] used for sputtering polycrystalline samples that allows both current-in-plane (CIP) and current-perpendicular-to-plane (CPP) measurements simultaneously. Both Nb contact layers and spin-valves were produced by sequential d.c. magnetron sputtering onto a p-type (001) Si substrate, while masking as appropriate for the different layers. Spin-valve multilayer structures were sandwiched between 1.1 mm wide, 250 nm thick, crossed Nb strips. The strips overlapped in a small area of the spin-valve ~ 1.2 mm^2. When cooled in liquid helium at 4.2 K, these thick Nb strips become superconducting and form equipotential surfaces above and below the multilayer,

Table 2.1 Polycrystalline Spin-Valve Samples and Sputtering Temperatures

No.	Sample Composition and Thickness (nm)	Sputtering T (°C)	SV Type
761-4	$Nb_{250}//Cu_{10}/FeMn_8/Py_3/Cu_{20}/Py_3//Nb_{250}$	-33	EBSV
763-11	$Nb_{250}//Cu_{10}/FeMn_8/Py_{30}/Cu_{20}/Py_{30}//Nb_{250}$	6.5	
826-12	$Nb_{250}//Cu_{10}/FeMn_8/Py_3/Cu_{20}/Py_3//Nb_{10}$	18	
826-13	$Nb_{250}//Cu_{10}/FeMn_8/Py_{24}/Cu_{20}/Py_{24}//Nb_{10}$	22	
881-1a	$Nb_{250}//Cu_{10}/FeMn_8/Py_{30}/Cu_{20}/Py_{30}//Nb_{10}$	-65	
881-2a	$Nb_{250}//Cu_{10}/FeMn_8/Py_3/Cu_{20}/Py_3//Nb_{10}$	-56	
719-1	$Nb_{250}//Ag_{10}/Py_3/Ag_{20}/Py_3/FeMn_8//Nb_{250}$	-67	
719-1	$Ag_{10}/Py_3/Ag_{20}/Py_3/FeMn_8$	-67	
990-8b	$Ag_{10}/Py_3/Ag_{20}/Py_3//Nb_{10}$	-14	
990-8a	$Ag_{10}/Py_6/Ag_{20}/Py_6//Nb_{10}$	-14	
990-7b	$Ag_{10}/Py_{24}/Ag_{20}/Py_{24}//Nb_{10}$	-31	
1042-3	$Nb_{250}//Cu_{10}/(Py_{24}/Cu_{20}/CoZr_{20}/Cu_{20})\times10/Cu_{10}//Nb_{250}$	8	Hybrid SV
1043-7	$Nb_{250}//Cu_{10}/FeMn_8/CoZr_{20}/Cu_{20}/CoZr_{20}/Cu_{10}//Nb_{250}$	-7	EBSV

22
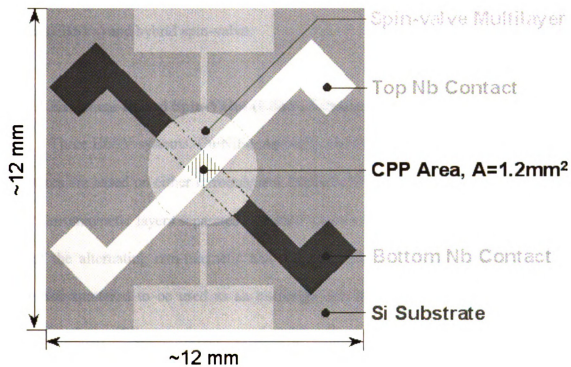
Figure 2.1 Top view of the duplex designed CIP and CPP measurement configuration.

which ensure a uniform current distribution through the layers for CPP resistance measurements [64]. The sputtering took place using a chilled substrate stage which tends to increase a few degrees in temperature during the sputtering. The direction of magnetization of the pinned ferromagnetic layer was fixed by annealing the samples in an external magnetic field at about 170°C for about 10 to 15 minutes. The following section will introduce two kinds of polycrystalline spin-valve samples: exchange-biased spin-valves (EBSVs) and hybrid spin-valve.

2.1.1.1 Exchange-Biased Spin-Valve (EBSV) Samples

Three EBSV systems, Cu/NiFe, Ag/NiFe, and Cu/CoZr were investigated. These structures are based on either ferromagnetic Permalloy™ (Py = $Ni_{1-x}Fe_x$ with x ≈ 0.16) or CoZr ferromagnetic layers separated by either a Cu or a Ag non-magnetic layer. At the end of the alternating non-magnetic and magnetic layers, an anti-ferromagnetic FeMn layer was sputtered to be used as an exchange bias material for pinning the magnetic moments of one of the two ferromagnetic (either Py or CoZr) layers in a fixed direction. The magnetic moment of the other ferromagnetic layer remained free to rotate under the influence of an external applied magnetic field. This arrangement allows the magnetizations of the ferromagnetic layers to easily switch between parallel and anti-parallel configurations. If the thicknesses of both magnetic layers are identical, the EBSV structure is referred to as a symmetrical EBSV.

The first set of samples included six Cu/Py EBSVs with configurations of $[Nb_{250}//Cu_{10}/FeMn_8/Py_x/Cu_{20}/Py_x//Nb_{250}]_{nm}$ (where x varies from 3 nm to 30 nm) layer arrangements, which were deposited by d.c. magnetron sputtering at different

temperatures onto p-type (100) Si substrates with natural thin oxide coatings at different temperatures. Three spin-valve samples with t_{Py} = 3 nm were deposited at substrate temperatures of approximately -56°C, -33°C and 18°C. The other three spin-valve samples with t_{Py} = 24 or 30 nm were deposited at substrate temperatures of approximately -65°C, 6.5°C and 22°C.

The second set of polycrystalline spin-valve samples examined in this study consisted of Ag/Py EBSVs. The first sample studied was in the form of $[Ag_{10}/Py_3/Ag_{20}/Py_3/FeMn_8]$ sandwiched between crossed Nb contacts and in adjacent uncrossed areas. Three additional Ag/Py spin-valve samples in the form of $[Ag_{10}/Py_3/Ag_{20}/Py_3/FeMn_8//Nb_{20}]_{nm}$ and $[Ag_{10}/Py_x/Ag_{20}/Py_x//Nb_{10}]_{nm}$ with x = 6 nm or 24 nm were fabricated under the same conditions as the first sample, but sputtered directly onto an area of approximately 1 cm^2 of Si substrate.

The third set consisted of one CoZr based symmetrical EBSV in the form of $[Cu_{10}/FeMn_8/CoZr_{20}/Cu_{20}/CoZr_{20}/Cu_{10}]_{nm}$ between crossed Nb contacts.

2.1.1.2 Hybrid Spin-Valve Sample

One hybrid spin-valve structure, based on different ferromagnetic materials Py and CoZr separated by a non-magnetic Cu layer, was studied. The reason for using two different magnetic layers is to allow independent rotation of the direction of the magnetizations in these layers. This CoZr based hybrid spin-valve was in the form of $[Nb_{250}//Cu_{10}/(Py_{24}/Cu_{20}/CoZr_{20}/Cu_{20})\times10/Cu_{10}//Nb_{250}]_{nm}$. The Py layer rotates first and easier than CoZr in this sample.

2.1.2 Epitaxial Multilayers/Spin-Valves And Fabrication

The substrates for epitaxial GMR multilayer fabrication were $(11\bar{2}0)$ oriented sapphire (Al_2O_3) single crystal wafers that had been pre-deposition annealed at 1200°C. Single-crystal $(1\bar{1}0)$ Nb contact layers were sputter deposited on these annealed sapphire substrates at a substrate temperature of 750°C, and annealed at 950°C for about 10 minutes [54]. Cu buffer layers were then deposited onto the Nb contact layers at temperatures ranging from room temperature to 500°C; some of these buffer layers were then annealed at 350°C. Subsequent Co or Py or FeMn films were deposited onto the Cu buffer layer at various temperatures; and the rest of the multilayers were deposited at 80~100°C. The top Nb layers were applied at room temperature. All films were grown with a 0.325 Pa Ar chamber pressure (base pressure ~ 1.3×10^{-6} Pa). The deposition rate was 0.3 nm/s for Nb, Co and Py; 0.4 nm/s for Cu as determined by Loloee [33]. Table 2.2 shows the epitaxial samples in this study.

2.2 CROSS-SECTIONAL TEM SAMPLE PREPARATION:

The technique used for cross-section TEM thin foil preparation was the slab-on-ring method developed by Romano et al. [65,66] and Shaapur and Park [67], and modified by Howell [68] and Geng, et al. [63]. In this method, a composite slab was formed by using Gatan™ G-1 epoxy to join two pieces of the multilayer face-to-face. Cross sections of this slab were made normal to the layer plane. The individual pieces were then epoxied onto molybdenum rings and pre-thinned using a dimpler and low angle ion milled to electron transparency. Figure 2.2 shows an overview of the cross-section TEM sample preparation sequence. The detailed procedure to form a cross-

Table 2.2 Epitaxial Samples and Growth Temperatures

No.	Sample Composition and Thickness (nm)	Cu (buffer layer)		Py	Co
		Growth T (°C)	Annealing T (°C)	Growth T (°C)	Growth T (°C)
20-1	$Nb_{250}//Cu_{20}/(Co_6/Cu_6)\times6//Nb_{100}$	150	350	N/A	80~100
20-3	$Nb_{250}//Cu_{20}/(Co_6/Cu_6)\times6//Nb_{100}$	450	---	N/A	80~100
20-4	$Nb_{250}//Cu_{20}/(Co_6/Cu_6)\times6//Nb_{100}$	450	---	N/A	550 (1st Co)
27-3	$Nb_{250}//Cu_{20}/Py_{24}/Cu_{20}/Py_{24}/FeMn_8//Au_{15}/Nb_{100}/Au_{15}$	350	---	80~100	N/A
27-4	$Nb_{250}//Cu_{20}/Py_{24}/Cu_{20}/Py_{24}/FeMn_8//Au_{15}/Nb_{100}/Au_{15}$	450	---	80~100	N/A
28-3	$Nb_{250}//Cu_{20}/Co_{1.5}/(Cu_2/Co_{1.5})\times20//Au_{15}/Nb_{100}/Au_{15}$	350	---	---	400 (1st Co)
31-2	$Nb_{250}//Cu_{100}/Py_{100}/FeMn_{50}//Nb_{100}$	150	350	350	N/A
37-3	$Nb_{250}//Cu_{20}/Py_{24}/Cu_{20}/Py_{24}/FeMn_8//Au_{15}/Nb_{100}/Au_{15}$	150	350	80~100	N/A
40-3	$Nb_{250}//Cu_{20}/FeMn_8/Py_6/Cu_{24}/Py_{24}//Au_{15}/Nb_{100}/Au_{15}$	350	---	---	N/A
41-2	$Nb_{200}//Cu_{10}/Nb_{10}$	500	---	N/A	N/A
41-3	$Nb_{200}//Cu_{100}/Py_{200}$	500	---	80~100	N/A
43-1	$Nb_{200}//Cu_{20}/Py_{20}//Nb_{20}$	100	---	RT	N/A
43-2	$Nb_{200}//Cu_{20}/Py_{20}//Nb_{20}$	150	---	RT	N/A
43-3	$Nb_{200}//Py_{20}/Cu_{20}//Nb_{20}$	RT	---	350	N/A
43-4	$Nb_{200}//Py_{20}/Cu_{20}//Nb_{20}$	RT	---	150	N/A

section TEM sample was as follows:

Form a composite slab:

1. Section multilayer sample on substrate into about 2.2 mm wide slabs with a Struers™ Accuton-5 diamond saw operated at 3000-rpm wheel speed with a 5 μm/sec feed speed.

2. Clean slabs in acetone, followed by a rinse with ethanol.

3. Glue two slabs of the multilayer face-to-face with a thin layer of Gatan™ G-1 epoxy.

4. Clamp multilayer sample with gentle pressure in a spring-loaded Teflon™ lined clamp.

5. Cure epoxy on a hot plate for about 10 minutes at 130°C, then cool it down.

6. Mount the resulting stack on a 3 x 1 inch micro slide with Crystalbond™ mounting wax.

7. Slice the stack perpendicular to the growth plane into 800~1000 μm thin slabs with a diamond saw using Struers Accuton-5 operated under the same conditions as in step 1. This step prepares the cross-section interfaces of the slabs to be polished.

8. Dissolve Crystalbond™ mounting wax in acetone and rinse the slabs by ethanol.

Grind and polish slabs to ~100 μm thick:

9. Mount a composite slab onto a 19 mm diameter sapphire flat with Crystalbond™ mounting wax and attach it into a sapphire flat holder that fits into the polishing block. (The use of the polishing block grinder allowed the slabs to be uniformly polished to a thickness of 100 μm while maintaining parallel top and bottom

1
Specimen slab

2
Score
and Break

3
G1 Glue

4
Saw
cross-sections

5
Glue on
Mo-ring

6
Dimpling

7
Ar⁺
Ar⁺
Low-Angle
Ion milling
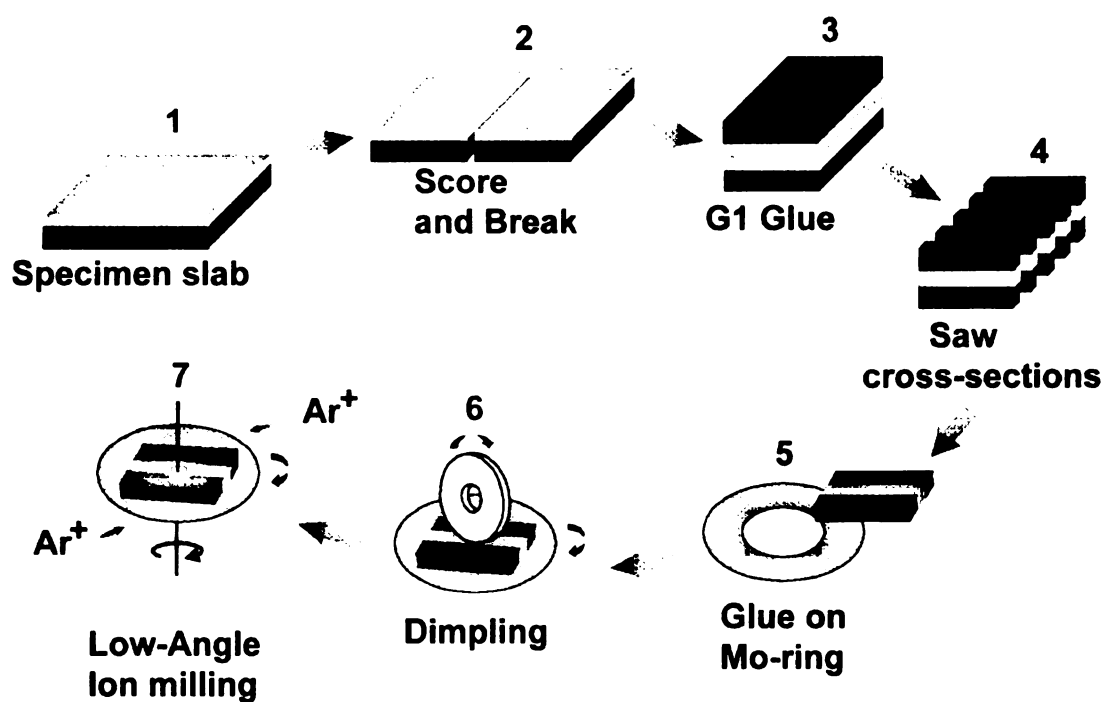
Figure 2.2 Schematic representation of the cross-section TEM samples preparation.

surfaces.)

10. Grind and polish one side of a slab with a series of diamond lapping films (15, 9, 6, 3, 1, 0.5 mm Allied™ Diamond Lapping Film).

11. Separate the slab from the sapphire flat using acetone; rinse with ethanol.

12. Measure sample assembly thickness using a micrometer to determine the amount of material needed to be removed by grinding.

13. Glue polished side of the slab to a 3 mm in diameter molybdenum support ring with Gatan™ G-1 epoxy and cure epoxy on a hot plate for 10 minutes at 130°C using an 8 mm thick piece of Teflon™ to prevent attachment of the slab and ring to the hot plate itself.

14. Mount the slab and Mo ring to the center of a sapphire flat with a thin layer of Crystalbond™ mounting wax.

15. Measure the total thickness of sample assembly plus Mo-ring and sapphire flat.

16. Grind and polish the unpolished side of sample assembly to ~100 μm excluding the ~30 μm thickness of the Mo-ring with a series of diamond lapping films (same sequence as used in step 10).

Dimple slabs to 10~20 μm thick:

17. Mount and center the assembly on a VCR™ Group D500i Dimpler platen using an eccentric platen assembly.

18. Dimple the top surface of the Si based samples using a 15.5 mm stainless steel dimpling wheel with 1 μm diamond slurry in reservoir; or for the sapphire based samples, dimple using a 1 μm embedded-diamond lapping wheel with VCR™ lapping vehicle as the lubricant until obtaining a center thickness of about 10 to

20 μm.

19. Final polish with colloidal diamond (0.05 nm) to a specular (mirror like) surface.

20. Dismount the sample assembly from sapphire flat with acetone and rinse in ethanol and air-dried.

Note: The final dimpling depth of the cross-section was monitored by removing both the sample and platen and placing the assembly in a transmitted light microscope. At a thickness less than 10 μm, the silicon substrate will transmit red light. The thickness of the sapphire substrate is difficult to monitor since the sapphire itself is transparent. However it was found that the samples would have a tendency to crack before a thickness of 10 μm was reached due to a lack of dampening control on the dimpler. It was determined that the best way to monitor the depth was to calculate the depth using the approximation, $d = r^2/D$, relating the diameter of dimple (2r) and wheel diameter (D) to dimple depth (d). The dimple diameter was measured under the microscope using a calibrated reticule. Based on the amount of material removed the estimated thinnest portions of the discs prior to ion milling were approximately 20 μm.

Ion-mill samples to electron transparency:

21. Mount the sample assembly on a Gatan DuoPost^{TM} support and ion mill with a Gatan M691 PIPS^{TM} ion mill.

22. Initially ion mill the center of sandwich interface at ±3°~ ±4° beam incident angle with 5 keV Ar$^+$ while turning at 3 rpm until perforation.

23. Final ion mill at ±2° or less until samples were thin enough for HRTEM observations.

2.3 CHARACTERIZATION AND IMAGE ANALYSIS TECHNIQUES:

Cross-section transmission electron microscopy (TEM) has been widely recognized as one of the most powerful techniques to perform analysis of the layers and interfaces of magnetic multilayers and spin-valves. The combination of a local diffraction pattern with the cross-sectional image provides unique and direct information on the local multilayer structures. With the advancement of high-resolution TEM, direct atomic structural imaging can be achieved with proper specimen preparation techniques and computer image simulations.

2.3.1 Conventional Transmission Electron Microscopy (CTEM)

Conventional transmission electron microscopy (CTEM) was used to characterize the overall morphology of the cross-sectional thin foils. Both bright field and axial dark field imaging were carried out in conjunction with selected area electron diffraction (SAED) to characterize overall microstructure features, such as the uniformity of the layers, grain or crystallite size, the orientation and texture of the grains, and the propagating roughness of the layers as a function of growth. All samples analyzed were tilted to a low index zone of the Si or sapphire substrates in order to orient the substrate plane and the growth plane of layers edge on.

The cross-section TEM thin foils were also characterized by CTEM to determine if the samples were thin enough for high-resolution transmission electron microscopy (HRTEM) study.

In this study, CTEM observations were performed using a Hitachi H-800 operated at 200 keV with a double-tilt specimen stage. Additional CTEM images were recorded at

32

the University of Michigan Electron Microbeam Analysis Laboratory on a JEOL-4000EX microscope operated at 400 keV with a double-tilt top entry stage. Images and SAED patterns were recorded on Kodak^{TM} Electron Microscope film 4489 (200 keV) and SO-163 (400 keV).

2.3.2 High-resolution Transmission Electron Microscopy (HRTEM)

The cross-sectioned samples which were determined to be suitable for high-resolution TEM study were further examined using a JEOL-4000EX operated at 400 keV at the University of Michigan Electron Microbeam Analysis Laboratory. HRTEM was used to directly image the details of the individual layers at the atomic level, such as crystal lattice, interfaces, and defects.

In general, HRTEM imaging requires: (1) a low index zone; in this study, the polycrystalline and epitaxial samples, were tilted to low index zones normal to the (001) Si and ($11\bar{2}0$) Al_2O_3 substrate planes respectively, to orient the layers edge-on: (2) thin specimens (thickness < 50 Å); when the specimen is too thick (> 50 Å), the weak-phase object approximation is not satisfied.

HRTEM images are essentially phase-contrast images. Often, the contrast in such images is described by the contrast transfer function (CTF), which is a theoretical parameter that models the performance of the microscope objective lens. This function is applied to the Fourier transform of the wave function after it exits the sample. After application of the CTF, the Fourier transform is again applied, resulting in the sample image. The CTF is described as

$$T(\mathbf{u}) = 2A(\mathbf{u}) \sin \chi(\mathbf{u})$$

where $T(\mathbf{u})$ is the transfer function, $A(\mathbf{u})$ is the aperture function, $\mathbf{u}$ is a reciprocal-lattice vector (frequency spacings), and $\chi(\mathbf{u})$ is the phase shift of the electron that occurs in the sample. The best resolution corresponds to the first zero position of $T(\mathbf{u})$ vs. $\sin\chi$ curve, which results in optimized balancing of the effect of spherical aberration against a particular negative value of defocus, as shown in figure 2.3. In the resulting wide plateau, all frequencies are transferred in a nearly equal manner. This particular defocus is called Scherzer defocus. Therefore, to optimize the contrast, all HRTEM imaging was carried out near the Scherzer defocus condition, which is described as

$$\Delta f_{\text{Scherzer}} = \sqrt{C_s \lambda}$$

where C_s is the spherical aberration and λ is the wavelength. When operating under Scherzer condition with a properly oriented thin crystal, the image can be directly interpreted in terms of the projected potential corresponding to the positions of the atom columns.

The JEOL-4000EX has a 0.17 nm point-to-point Scherzer resolution. Within this limit only the <001> and <111> bcc Nb, and the <011> fcc Cu, Ag, Py, and FeMn zone axes are directly interpretable; the values above this limit are shown in bold in Table 2.3. In the hcp structure of Al_2O_3 the <0001> and <01$\bar{1}$0> axes have spacings above the Scherzer limit as well.

At different conditions of defocus, the frequencies will be transferred differently, resulting in different plots of $\sin\chi$ as a function of $\mathbf{u}$. However, these plots will be damped out by the envelope damping function which includes the spatial coherence spread of the electron source and chromatic aberration effects, as shown in figure 2.4. Therefore, above a certain frequency, no information will be passed, resulting in a new
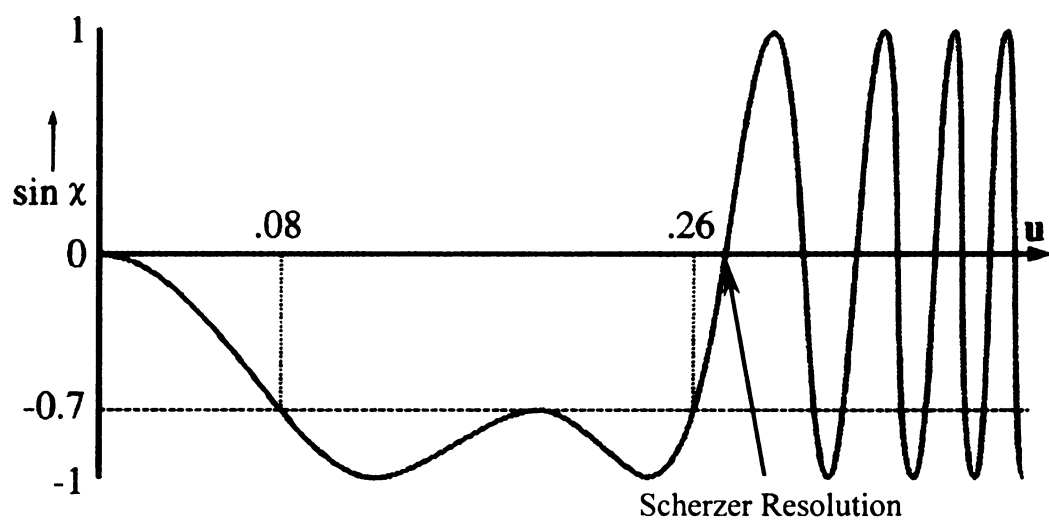
Figure 2.3 A schematic representation of $\sin\chi(\mathbf{u})$ versus $\mathbf{u}$ without damping of the higher spatial frequencies. The first zero position of $\sin\chi$ curve corresponds to Scherzer resolution [69].

Table 2.3 Unit Cell Parameters for Layer Materials

Materials	Crystal Structure	Lattice Parameter (Å)	Spacing (Å)	<001>	<011>	<111>
Nb	bcc	3.31	pt. to pt.	**2.34**	1.66	**2.70**
			line to line	1.66	1.66	**2.34**
Cu	fcc	3.61	pt. to pt.		**2.21**	1.47
			line to line		**1.81**	*1.28*
Ag	fcc	4.09	pt. to pt.		**2.50**	1.67
			line to line		**2.05**	1.45
Py	L1$_2$*	3.55	pt. to pt.		**2.17**	1.45
			line to line		**1.78**	*1.26*
FeMn	fcc	3.63	pt. to pt.		**2.22**	1.48
			line to line		**1.82**	*1.28*
Co	fcc	3.54	pt. to pt.		**2.17**	1.45
			line to line		**1.78**	*1.26*

Note: the Bold numbers represent the values above the Scherzer limit (1.7 Å), while values in Italics represent spacings below the information limit (1.4 Å).

* Bulk Permalloy™ (Py) displays the fcc derivative L1$_2$ structure. However, because of the fairly small differences in the atomic scattering factors and because the Py used in this study is significantly off-stoichrometric, the superlattice reflections are very weak and do not appear on the FFT diffractograms. For the same reasons, the L1$_2$ ordering is not evident in the HRTEM images. Thus, for the purposes of this work, Py will be treated as fcc.
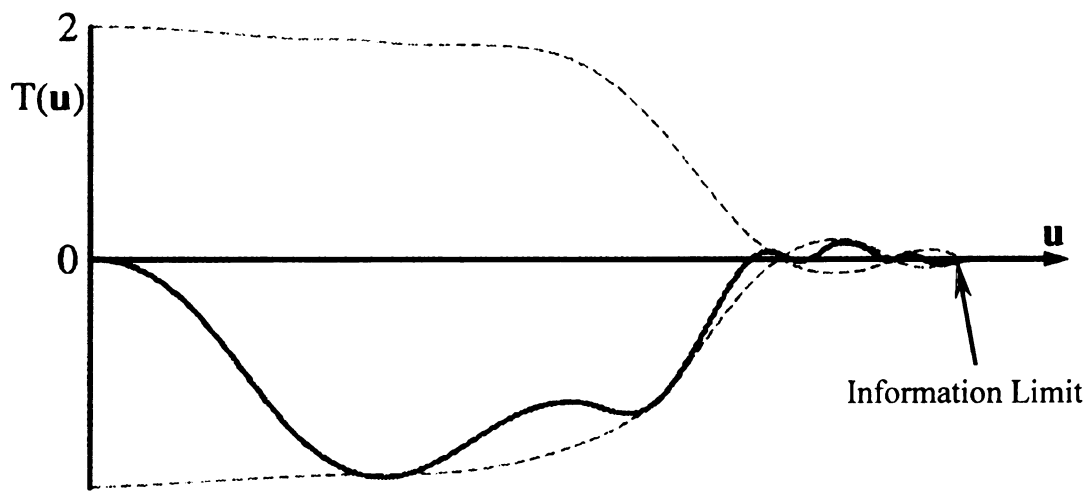
Figure 2.4 A schematic representation of T(**u**) versus **u** modified by the damping envelope (dash line) which ends up the information limit. [69]

resolution limit which is called the information limit. If the defocusing condition is properly modified, resolution limits can be improved down to the information limit. The available defocusing values are given by

$$\Delta f_n = \Delta f_{Scherzer} \sqrt{2n-1}$$

where $\Delta f_{Scherzer}$ is Scherzer defocus and n is an integer. When n=1, this relation represents the Scherzer defocus condition. When n is larger than 1, good contrast imaging is also possible by making use of "passbands" in the transfer function, which allows higher spatial frequencies to be included in the image and permits access to finer detail of the structure. However, the images so obtained may not give a true image of the specimen because information at certain frequencies, such as defects, could be lost. In this case, the image cannot be interpreted directly. Rather, image simulations, FFT diffractograms, and image processing are necessary to complement the analysis of HRTEM images. The JEOL-4000EX has an information limit of 0.14 nm; values below this limit are shown in italics in Table 2.3.

2.3.3 Fast Fourier Transform (FFT) Analysis

It is difficult to obtain electron diffraction patterns directly from areas within grains in the individual spin-valve layers due to their small width normal to the beam. Therefore, fast Fourier transform (FFT) image analysis has been employed to assist the interpretation of the HRTEM images. The FFT diffractograms of the experimental HRTEM images reveal equivalent plane spacing and angular information from those selected areas of the specimen.

In this study, FFT image analysis was accomplished by capturing selected area

of constant magnification HRTEM prints using a flat bed scanner, then processing and analyzing the images using the NIH Image [70] and/or Adobe PhotoShop[®]. The Si, Nb, and Al_2O_3 reflections were used as internal calibration standards to determine the effective camera lengths (for a given micrograph negative) for interpreting the FFT diffractograms. Based on these calibrations, the individual layers were then accurately characterized from the diffractograms by measuring the lattice parameters and interplanar angles of the layer phases.

HRTEM image simulations were carried out using the EMS software package [71] by J.W. Heckman of the department of Materials Science and Mechanics at Michigan State University, details have been described in [63]. These simulations have been carried out for changes of thickness and defocus, based on the fixed microscope parameters of: accelerate voltage 400 KeV, spherical aberration C_s 1.1 mm, beam convergence semi-angle 0.72 mrad, objective aperture 19 nm^{-1}, focus spread 9 nm, Scherzer defocus 52.08 nm.

CHAPTER III

STRUCTURAL STUDIES OF POLYCRYSTALLINE Cu/Py GMR SPIN-VALVES

3.1 INTRODUCTION

The first set of the polycrystalline exchange-biased spin-valves examined in the present study had the form of $Fe_{50}Mn_{50}$/Py/Cu/Py. Six Cu/Py spin-valves sputtered at different temperatures have been studied. Three of these spin-valves are in the form of $[Nb_{250}//Cu_{10}/FeMn_8/Py_3/Cu_{20}/Py_3//Nb_x]$ with thin (3 nm) Py layers, while the others are of form $[Nb_{250}//Cu_{10}/FeMn_8/Py_{24\sim30}/Cu_{20}/Py_{24\sim30}//Nb_x]$ (where x is 10 or 250 nm) with thick (24 nm and 30 nm) Py layers. The top and bottom Nb layers serve as superconducting contacts for perpendicular resistance measurements [64]. All of the spin-valves were produced by d.c. magnetron sputtering onto p-type (100) Si substrates with natural thin oxide coatings. The sputtering took place using a chilled substrate stage. With this stage, the sample temperature tends to increase a few degrees during the sputtering. The initial temperatures were approximately 18°C, -33°C, and -56°C for the three spin-valves with thin Py layers and 22°C, 6.5°C, and -65°C for those with thick Py layers.

In this study, CTEM and HRTEM have been performed on cross-sections of the six Cu/Py spin-valves. CTEM allows characterization of microstructural features such as crystallographic epitaxy and texture, layer quality, and interfacial roughness. HRTEM with associated quantitative image analysis techniques including image simulations and fast Fourier transform techniques, allows extraction of structural information at the atomic scale [72,73].

3.2 CTEM OBSERVATIONS

3.2.1 Spin Valves with Thick Py Layers

CTEM was used to characterize the overall structure of the spin valve multilayers. Figure 3.1 shows a cross-sectional brightfield/darkfield image pair of the spin valve with 30 nm Py layers sputtered at 6.5°C. In both images, the Si substrate, the top and bottom Nb contacts, and the spin valve (SV) multilayer can be distinguished. The Nb contacts and the spin valve both appear to be continuous, polycrystalline, and are uniform in thickness. Unfortunately, because of the low mass and diffraction contrasts between FeMn (Z = 25.5), Py (Z = 27.7), and Cu (Z = 29), the individual layers within the spin valve are not readily resolved.

The dark field image (figure 3.1 (b)), which was taken using an arbitrary diffraction direction, helps to establish some structural characteristics. Polycrystalline grains have a columnar structure with a wide range in crystal size perpendicular to the growth direction, with observable widths ≤ 90 nm. The individual grains generally have grown in columns, starting in the bottom Nb contact. In many cases, epitaxy within these grains has continued into, and sometimes through, the spin valves. In other cases, abrupt changes in image intensity (due to changes in diffraction contrast) at the Nb/SV interfaces indicate significant changes in orientation and loss of strict epitaxy during the growth process. In most areas, the grains within the spin valve appear epitaxial.

The overall structures of the spin valves with 30 nm Py layers sputtered at -65°C and with 24 nm Py layers sputtered at 22°C as shown in figure 3.2 and 3.3 also show excellent contrast between both polycrystalline Nb contacts and the spin valves, and weak contrast between the individual spin valve layers. The morphology is again columnar.
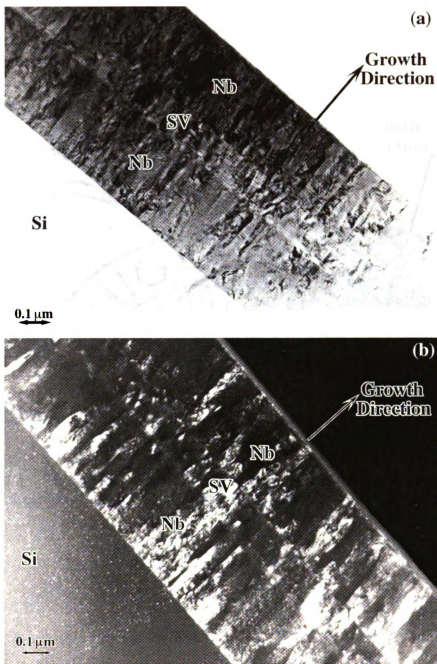
Figure 3.1 (a) Bright field and (b) dark field cross-sectional CTEM images of the $[Nb_{250}//(Cu/FeMn/Py/Cu/Py)//Nb_{250}]_{nm}$ spin valve with 30 nm Py layers sputtered at 6.5°C. The darkfield image was taken using an arbitrary diffraction direction.
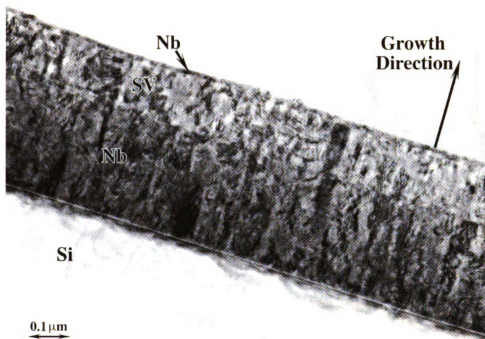
Figure 3.2 A cross-sectional brightfield CTEM image of the $[Nb_{250}//(Cu/FeMn/Py/Cu/Py)//Nb_{10}]_{nm}$ spin valve with 30 nm Py layers sputtered at -65°C.
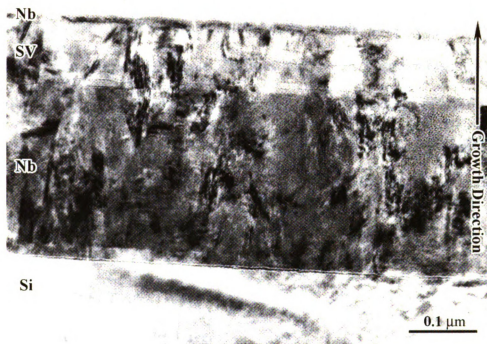
Figure 3.3 A cross-sectional brightfield CTEM image of the $[Nb_{250}//(Cu/FeMn/Py/Cu/Py)//Nb_{10}]_{nm}$ spin valve with 24 nm Py layers sputtered at 22°C.

3.2.2 Spin Valves with Thin Py Layers

Figure 3.4 shows a cross-sectional CTEM micrograph of the spin valve with 3 nm Py layers sputtered at -56°C. The overall structure is similar to that in the spin valves with thick Py layers. The Nb contacts and the spin valve appear continuous and are uniform in thickness. The grains are generally columnar with a significant degree of epitaxy, with in-plane grain diameters similar to those in the thick Py spin valves (less than 80 nm). Again, due to the degree of epitaxy and the low mass contrast, it is difficult to distinguish the individual spin valve layers although some evidence of layering can be seen, most likely due to the Fresnel effects. Similar overall structures were also observed in the spin valves with 3 nm Py layers sputtered at -33°C and 18°C as shown in figure 3.5 and figure 3.6.

3.3 HRTEM AND FFT ANALYSIS

3.3.1 Spin Valves with Thin Py Layers

A cross-sectional HRTEM image of the $(Cu_{10}/FeMn_8/Py_3/Cu_{20}/Py_3)_{nm}$ spin valve with 3 nm Py layers sputtered at -56°C is shown in figure 3.7. On this scale, it is apparent that the interfaces between the Nb contacts and the spin valve are wavy, displaying some interfacial roughness. The first Cu layer and FeMn layer are now weakly visible. The other individual layers are not readily distinguishable due to weak mass contrast. Consequently, only the nominal locations of the individual spin valve layers are indicated. Both the Nb contacts and the spin valve appear polycrystalline with columnar grains, consistent with the CTEM observations. While most of the grains display lattice fringes running perpendicular to the growth direction, only a fraction of the cross-section is
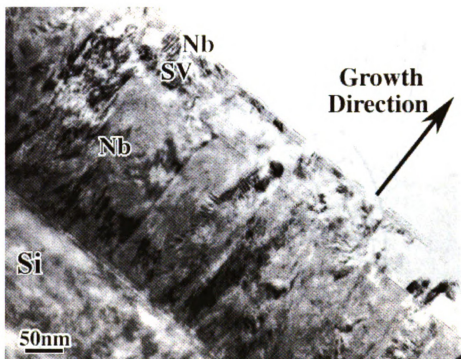
Figure 3.4 A cross-sectional brightfield CTEM image of the [Nb$_{250}$//Cu/FeMn/Py/Cu/Py//Nb$_{10}$]$_{nm}$ spin valve with 3 nm Py layers sputtered at -56°C.
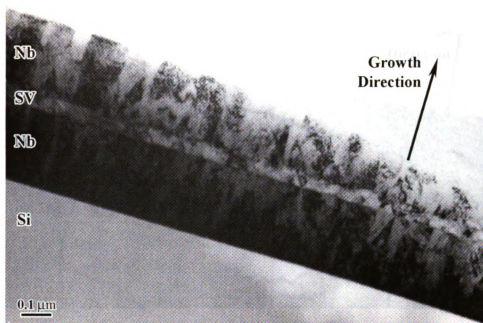
Figure 3.5 A cross-sectional brightfield CTEM image of the $[Nb_{250}//Cu/FeMn/Py/Cu/Py//Nb_{10}]_{nm}$ spin valve with 3 nm Py layers sputtered at -33°C.
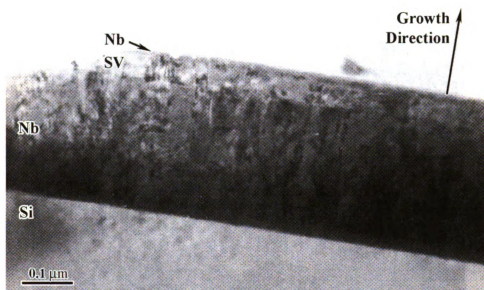
Figure 3.6 A cross-sectional brightfield CTEM image of the $[Nb_{250}//Cu/FeMn/Py/Cu/Py//Nb_{10}]_{nm}$ spin valve with 3 nm Py layers sputtered at 18°C.
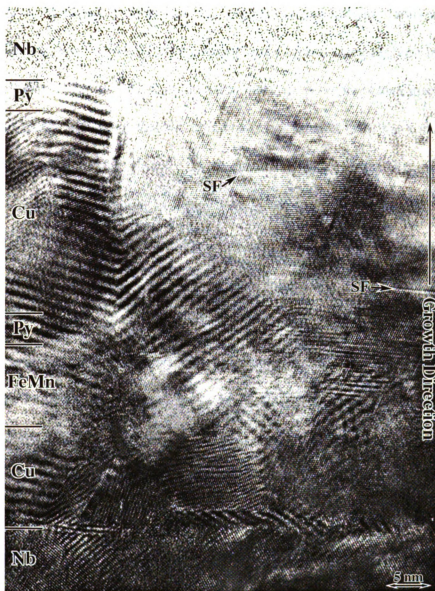
Figure 3.7 A cross-sectional HRTEM image of the [Nb//Cu$_{10}$/FeMn$_8$/Py$_3$/Cu$_{20}$/Py$_3$//Nb]$_{nm}$ spin valve with 3 nm Py layers sputtered at -56°C with nominal layer positions indicated. The first Cu layer and FeMn layer are weakly visible, while the other individual layers are difficult to distinguish due to the small differences in the average atomic numbers of the multilayer components. (SF – stacking fault)

oriented to zones favorable for HRTEM structural imaging. In addition to lattice image contrast, significant numbers of Moiré fringes appear on the image due to overlapping of grains in the cross-sectional TEM sample. Numerous dislocations, twins and stacking faults can also be seen. An HRTEM micrograph of a typical stacking fault in the second Cu layer is shown in figure 3.8. It is clear that there are no extra planes inserted parallel to the defect plane, indicating that the defect was not created from the condensation of vacancies, but instead formed directly during growth or as a consequence of dislocation slip. The Burgers circuit drawn in figure 3.8 reveals a net displacement of a/4[$\bar{1}2\bar{1}$] perpendicular to the electron beam direction, which is consistent with a perfect lattice translation of a/2[$\bar{1}10$] in an fcc lattice, with a component of a/4[$\bar{1}01$] in the beam direction.

To more fully assess the structures seen in the HRTEM images, fast Fourier transform (FFT) diffractograms were taken from selected areas within the nominal layer locations. These diffractograms allowed accurate analysis of the lattice parameters and interplanar angles of the different spin valve layers. An example of this type of analysis is shown in figures 3.9 and 3.10 for the spin valve with 3 nm Py layers sputtered at -56°C. To calibrate the FFTs, the Nb contacts have been used as internal standards. Figure 3.9 shows selected areas from the Nb contacts and their corresponding FFT diffractograms, which effectively give the diffraction patterns from these areas. The FFT patterns of the top and bottom Nb contacts show that these grains are imaged in <111> orientations, characterized by the 60° interplanar angles. The characteristic diffraction spots are {110} type (the first reflections allowed for bcc materials and the first diffraction vectors which lie in the {111} zone). In both the top and bottom Nb contacts, the growth directions are
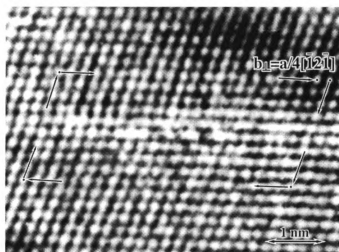
Figure 3.8 A HRTEM micrograph showing a stacking fault lying in the second Cu layer of the spin valve with 3 nm Py layers sputtered at -56°C. The Burgers circuit results a net displacement of a/4[$\bar{1}2\bar{1}$].
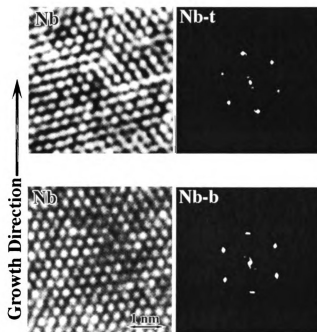
Figure 3.9 HRTEM images (left) and corresponding FFT patterns (right) of the top (upper) and bottom Nb contacts of the Cu/Py spin valve with 3 nm Py layers sputtered at -56°C. These patterns were used as a calibration for the patterns displayed in figure 3.10.

close to <110>, indicating the growth and subsequent epitaxy on the {110} (closest packed) bcc planes. The equilibrium {110} interplanar spacing for bulk Nb is 0.234 nm (a_{Nb}=0.331nm). From this value the spacing of the {110} spots has been used to calibrate an effective camera length for the subsequent FFTs.

The layers within a large number of columnar grains from the layers of the spin valve grown at -56°C with 3 nm Py layers have been analyzed, examples of which are shown in figure 3.10. Beginning with the first Cu layer, the measured angles are 55°, 55°, and 70°, indicating that the HRTEM image corresponds with a <110> fcc zone. The interplanar spacing of the {111} planes is measured to be 0.21 nm, which corresponds to an fcc lattice parameter of 0.359 nm. This is very close to the bulk value of 0.361 nm for fcc Cu. A consistent analysis is found for the second Cu layer. In both cases, the growth direction is near <111>. Using the same approach, the FeMn and the Py layers were also found to display fcc and $L1_2$ structures respectively, with <111> growth directions (the superlattice reflections from the Py $L1_2$ structure are extremely weak). This behavior suggests that the closest packed {111} planes in the fcc Cu, FeMn and $L1_2$ Py layers are epitaxial with the closest packed {110} planes in the bcc Nb contacts. The {111} interplanar spacing are measured to be 0.210 nm for FeMn and 0.204 nm for Py, which correspond to lattice parameters of 0.364 nm (a_{FeMn} = 0.363 nm) and 0.353 nm (a_{Py} = 0.355 nm).

Similar imaging and analysis was carried out on the spin valve with 3 nm Py layers sputtered at -33°C. A cross-sectional HRTEM image of this material (figure 3.11) again shows that the interfaces between the spin-valve and Nb contacts are wavy, and that the individual component layers within the spin-valve cannot be clearly identified. Once
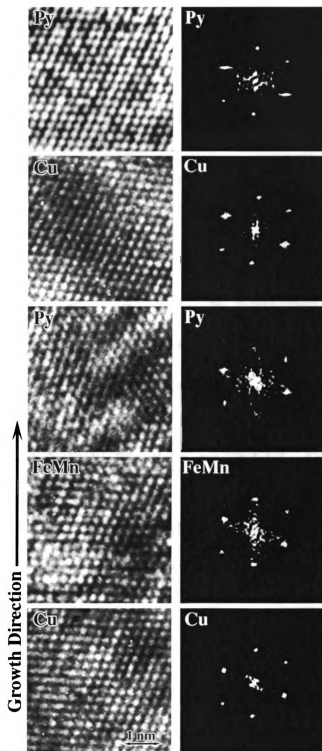
Figure 3.10 HRTEM images and FFT patterns of various layers of the Cu/Py spin valve with 3 nm Py layers sputtered at -56°C. All of the component layers display their equilibrium fcc (Cu, FeMn) or L1$_2$ (Py) <110> zone patterns.
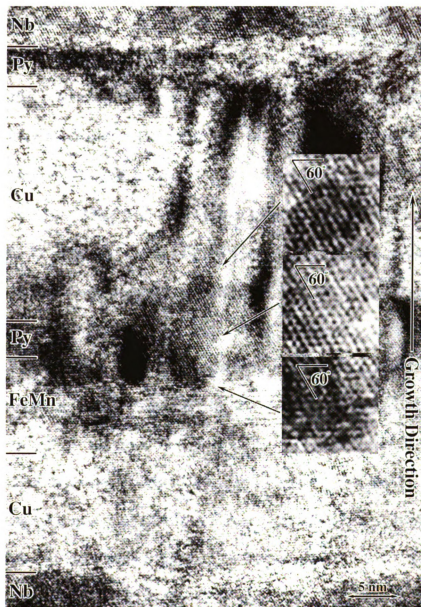
Figure 3.11 Cross-sectional HRTEM image of the Cu/Py spin valve with 3 nm Py layers sputtered at -33°C. Some of the columnar grains of the Cu, FeMn and Py layers display <111> symmetry characterized by 60° interplanar angles (inset column).

again full structural images cannot be resolved in all of the grains, but lattice fringes with consistent spacing can be seen running perpendicular to the growth direction in the bottom Nb contact, the spin valve, and the top Nb contact. This suggests epitaxial growth throughout the structure. Some defects can also be seen in the images, such as dislocations, twins and stacking faults.

In grains oriented favorably for structural imaging, some columnar grains are found to display interplanar angles of 55°and 70° (indicative of <110> cubic zones) within the spin valve, while other columns display interplanar angles of 60° (indicative of <111> cubic zones). While the observation of the <110> symmetry is expected, and consistent with the expectation of fcc and $L1_2$ structures for the Cu, FeMn and Py layers, the observation of the structural images displaying <111> cubic symmetry (as shown in inset column of figure 3.11) is very surprising. All of the spin valve components have the fcc or the fcc derivative $L1_2$ structure in their bulk states. However, due to instrument resolution limitations, it should be difficult, if not impossible, to resolve the atomic structure of the <111> orientation in these materials. The JEOL-4000EX used in this study has a Scherzer resolution of 0.17 nm with an information limit of approximately 0.14 nm; obtaining images at resolutions near these limits can be very difficult. Table 3.1 shows the projected atom column spacing (the limiting spacing to be resolved) of the materials examined in this study for the <111> and <110> zone axes. The table shows these spacings, assuming the equilibrium structures, along with the spacing expected if they are assumed to take up non-equilibrium bcc structures (the non-equilibrium spacings have been calculated based on a simple hard sphere atomic modeling approach to determine the atomic radii). This table illustrates that for the fcc structures, the projected

Table 3.1 Projected atomic spacings for the <111> and <110> zone axes for layer components in fcc and bcc forms.

Layer Components	a_o^{fcc}(nm)	a_o^{bcc}(nm)	Minimum Column to Column Spacing (nm)			
			$<111>^{fcc}$	$<110>^{fcc}$	$<111>^{bcc}$	$<110>^{bcc}$
FeMn	0.363	0.296	0.148	0.222	0.242	0.148
Py	0.355	0.290	0.145	0.217	0.237	0.145
Cu	0.361	0.295	0.147	0.221	0.241	0.148
Nb		0.331			0.270	0.166

point to point spacings of the atomic columns are well above the resolution limits of the instrument for the <110> zones, but well below the Scherzer limit, and very close to the information limit for the <111> zones. Conversely, if bcc structures are considered, the <111> zones can be readily imaged, while the <110> zones will be very difficult to resolve. Thus, the observation of <111> symmetry in the HRTEM images suggests crystal structures other than fcc, while observations of <110> symmetry in the images indicates non-bcc structures. This concept is further supported by the HRTEM image simulations. Figure 3.12 shows series of HRTEM image simulations comparing the image characteristics of the <111> and <110> zones for both fcc and bcc structures for the range of specimen thickness' and image foci encountered experimentally. The amplitudes of the <111> fcc and <110> bcc structure images are so low as to render them effectively unresolvable in practice.

Figure 3.13 shows FFT diffractograms taken from selected areas within the nominal layer locations in this spin valve that display this <111> symmetry. Using the Nb for calibration, the measured interplanar angles for the Cu, FeMn and Py layers again indicate a <111> zone is being imaged. The interplanar spacing determined from the FFTs (0.21 nm) appears to correspond with the spacing of {111} planes in fcc Cu (d_{111}=0.208 nm), FeMn (d_{111}=0.210 nm) and $L1_2$ Py (d_{111}=0.205 nm). However, these reflections cannot appear in <111> zone patterns. Thus, the observed structures cannot be the equilibrium fcc or $L1_2$ structures. If it is assumed that these columns of the spin-valve layers have instead taken on the bcc structure, the measured interplanar spacings (based on the hard sphere model) are consistent with those expected for {110} bcc reflections. Furthermore, while it is not possible to resolve <111> zones in fcc Cu,
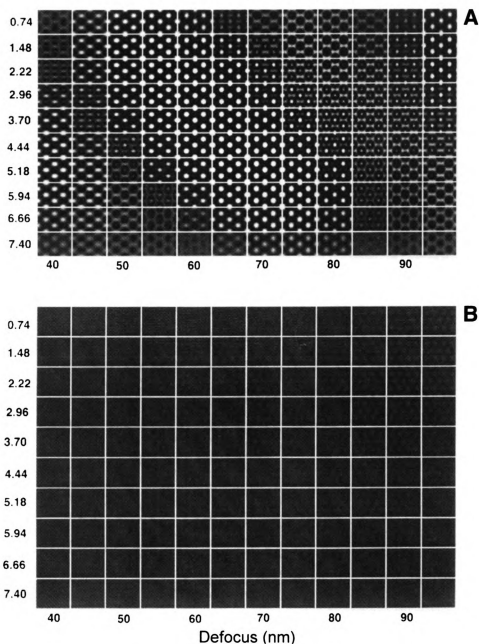
Figure 3.12 Bloch wave HRTEM simulations of copper in the fcc and bcc forms described in Table 3.1. The images simulate those viewed on a JEOL-4000 EX (400 KeV, C_s 1.1mm, beam convergence semi-angle 0.72 mrad, objective aperture 19 nm^{-1}, focus spread 9 nm, Scherzer defocus, 52.08 nm.) All images were printed using identical brightness and contrast ranges. (A) fcc Cu viewed along a <110> zone axis with specimen thickness and focus below Gaussian illustrated. (B) fcc Cu viewed along a <111> axis using identical operating conditions. (continued on next page)
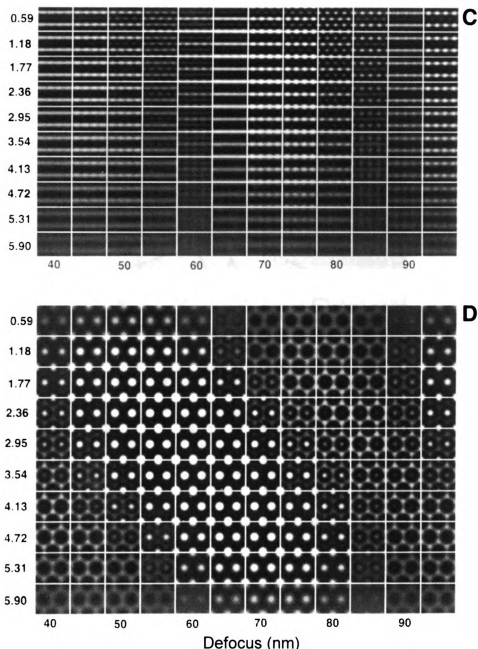
Figure 3.12 (C) The non-equilibrium bcc Cu viewed along a <110> axis. (D) The non-equilibrium bcc Cu viewed along a <111> axis. Although the microscope should allow the pass of fcc<111> and bcc<110> image information, in practice these images (especially fcc<111>) are likely to be unresolved due to the very low amplitude (≈ 0.07 of the average <110> axis in the simulated images) of the passed frequencies in this range. (Images and analysis are provided by J.W. Heckman.)
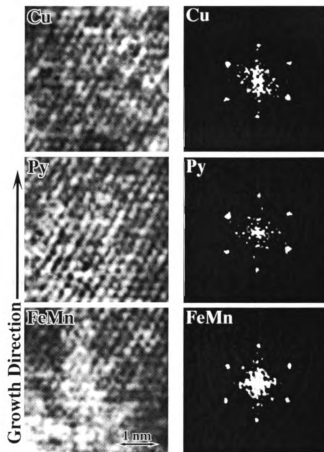
Figure 3.13 HRTEM images and corresponding fast Fourier transform diffractograms of various layers of the Cu/Py spin valve with 3 nm Py layers sputtered at -33°C showing <111> zone patterns in the Cu, FeMn and Py layers.

FeMn, and Py, bcc forms of those materials can be resolved in <111> orientations (Table 3.1). Thus, this analysis is consistent with the Cu, FeMn and Py layers taking up non-equilibrium bcc structures in this spin valve. Approximately six grain columns were examined in studying this spin-valve. Of these, two were found to display the bcc structure, while the rest displayed the equilibrium fcc structure. When either bcc or fcc structures were identified, the structure was maintained across the entire spin valve within that particular grain column.

A cross-sectional HRTEM image and similar analysis of the spin valves with 3 nm Py layers sputtered at 18°C as shown in figure 3.14 and figure 3.15 also revealed wavy interfaces between the polycrystalline Nb contacts and the spin valve, and weak contrast between the individual layers. The FFT analysis indicated that both Nb contacts and the spin valve appear in the equilibrium structures (bcc for Nb and fcc for spin-valves) with the close packed {111} planes in the fcc Cu, FeMn and Py layers epitaxial with the closest packed {110} planes in the bcc Nb. No bcc structures were found for this spin-valve. But since only four grain columns could be characterized in each sample, it is possible that non-equilibrium structures are present, but were not found in the small number of observations.

3.3.2 Spin Valves with Thick Py Layers

In general, the spin valves with thicker Py layers all displayed similar structures, including the existence of non-equilibrium structures in some columnar grains. A cross-sectional HRTEM image of the spin valve with 30 nm Py layers sputtered at -65°C (fig. 3.16) again shows excellent contrast between the polycrystalline Nb contacts and the spin valve, but weak contrast between the individual layers. A high density of planar defects

Figure 3.14 A cross-sectional HRTEM image of the $[Nb//Cu_{10}/FeMn_8/Py_3/Cu_{20}/Py_3//Nb]_{nm}$ spin valve with 3 nm Py layers sputtered at 18°C with nominal layer positions indicated. The individual layers of the spin valve are difficult to distinguish due to the small differences in the average atomic numbers of the multilayer components.
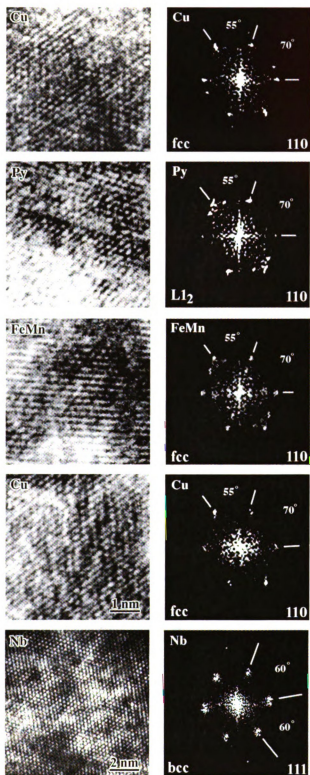
Figure 3.15 HRTEM images and FFT patterns of various layers of the Cu/Py spin valve with 3 nm Py layers sputtered at 18°C. All of the component layers display their equilibrium bcc (Nb) <111> and fcc (Cu, FeMn) or L1₂ (Py) <110> zone patterns.
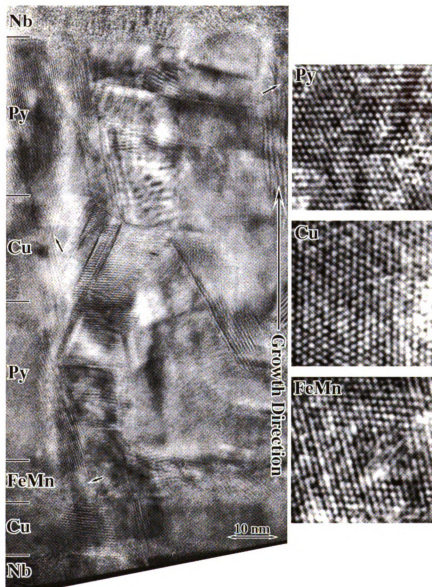
Figure 3.16 A cross-sectional HRTEM image of the spin valve with 30 nm Py layers sputtered at -65°C (left) and selected areas (indicated by arrows) from the FeMn, Cu and Py layers (right). The nominal layer locations are given in the image.

such as stacking faults and twins are evident in some columnar grains (in fact, these appear only in the fcc grains). A typical twin with a {111} coherent twin boundary from the second Py layer is shown in figure 3.17. As might be expected, some twin interfaces are parallel with the growth plane. However, twins are also observed on other {111} planes inclined to the growth direction. Characterization of the Nb contacts shows that, as expected, the Nb has grown with the bcc structure on the closest packed {110} planes (<110> wire texture).

As noted, HRTEM imaging and FFT analysis revealed both equilibrium fcc and non-equilibrium bcc structures in all three spin valves with thick Py layers. As was the case in the thinner spin valves, entire grain columns displayed the same structure across the spin valve. Figure 3.18 shows selected areas and their corresponding diffractograms from the spin valve with 30 nm Py layers sputtered at 6.5°C. The resolvable zones of this columnar grain in the Cu, FeMn, and Py layers are all characterized by 60° interplanar angles, indicating <111> zone axes. As explained earlier, the atomic structure for Cu, FeMn and Py cannot be readily resolved along <111> zones. Likewise, the interplanar spacing of 0.21 nm is not consistent with allowed reflections in fcc and $L1_2$ <111> zone patterns. Therefore, the spin valve appears to have some non-equilibrium bcc columnar grains. These grains grow on the {110} closest packed planes throughout the columnar grains. Likewise, in the spin valve with 30 nm Py layers sputtered at -65°C and with 24 nm Py layers sputtered at 22°C, resolvable <111> zones and corresponding bcc FFT diffractograms are found in some of the columnar grains (figure 3.19). This indicates that both of the spin valves can have the non-equilibrium bcc structures.
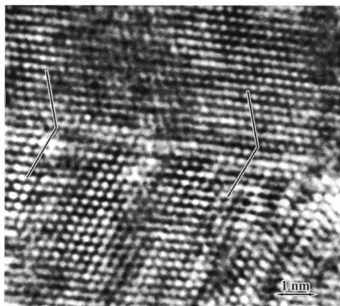
Figure 3.17 A {111} coherent twin boundary in the second Py layer in the Cu/Py spin valve with 30 nm Py layers sputtered at -65°C.
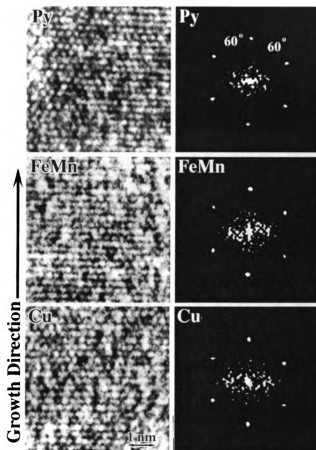
Figure 3.18 HRTEM images and FFT diffractograms of various layers of the Cu/Py spin valve with 30 nm Py layers sputtered at 6.5°C showing six-fold symmetry and lattice spacings consistent with bcc structures.
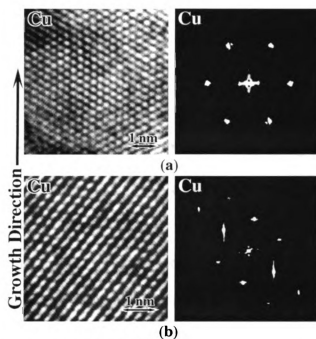
Figure 3.19 HRTEM images and FFT diffractograms of selected Cu layers within the Cu/Py spin valves (a) with 30 nm Py layers sputtered at -65°C and (b) with 24 nm Py layers sputtered at 22°C, indicating that both the spin valves can have the non-equilibrium bcc structures characterized by 60° interplanar angles in <111> zone patterns.

3.4 DISCUSSION

In all of the spin valves examined, growth appears to have occurred on the closest packed atomic planes; {110} planes in bcc and {111} planes in fcc. Such growth is expected since the close packed planes are typically characterized by low surface energies. However, the finding of non-equilibrium bcc forms of the spin valve components Cu, FeMn, and Py in some grain columns is somewhat surprising, and requires further discussion. Initially, it might be suspected that these findings are a consequence of chemical variations within the layers, which might lead to changes in crystal structure. However, high-resolution energy dispersive x-ray spectroscopy studies we have performed on similarly grown Ag/Py spin valves using a field emission gun STEM show that the layers are well defined chemically, with little or no interfacial mixing beyond the instrumental resolution of ~ 0.5 nm, and chemistries representative of the intended values in the interiors of the layers, away from the boundaries [58]. As the spin valves in the present study were all sputtered under similar conditions, differing only in the substitution of Cu for Ag, it is unlikely that chemical variations within the layers are responsible for the layers taking up non-equilibrium forms.

The HRTEM image simulations and FFT analysis clearly show that the Cu, FeMn, and Py in the spin valve with 3 nm Py layers sputtered at -33°C, and in all of three spin valves with thick Py layers, display some columnar grains that are not in their equilibrium fcc forms. The supposition that non-equilibrium structures occur in some of the spin valves follows from the identification of 60° interplanar angles in the HRTEM images and FFT analysis characteristic of cubic <111> zone axes, which cannot be resolved in the fcc structures. Furthermore, it should be recalled that these zone axes with three fold

symmetry (actually six in the FFTs due to ±g reflections) are identified in the cross-sectional orientation and the growth planes must lie close to perpendicular to this orientation. However, if the materials were fcc, the growth planes could not be {111} planes, as the angles between {111} planes in cubic materials are 70.5° and 109.5°. This is unlikely and inconsistent with the observed characteristic growth when fcc phases are present.

While it is clear that the layers noted above are not in their equilibrium forms, the suggestion that they have taken up the bcc crystal structure is thus far based only on the fact that the analysis is consistent with an assumed bcc structure. Thus, the conclusion that the layers are truly taking up bcc structures needs further justification. The key is again based on the observation of the three-fold symmetry of the HRTEM images in these layers. Such three fold symmetry can only be displayed by cubic (which display four 3 fold axes), hexagonal (truly 6-fold symmetry), and rhombohedral crystal structures.

However, if these layers were taking up a hexagonal structure, the growth direction perpendicular to the observed 3-fold axes would be of the form {XXX0}. These planes of the [0001] zone in general have low packing densities, with a maximum packing factors of 0.556 on the {1120} planes and 0.481 on the {1010} planes (as opposed to the maximum possible of 0.908 for {111} planes in fcc and {0001} planes in hcp). It is thermodynamically unlikely that growth would occur on such low-density planes. Similarly, if the layers took up a rhombohedral structure, the growth planes would have to be low-density irrational planes.

In contrast, if the non-equilibrium layers take up bcc structures, the growth can occur on {110} planes that are high density (packing factor of 0.833) and perpendicular to

the observed 3-fold zone axes. This situation is consistent with the observations noted above.

Epitaxial strains associated with the layer interfaces are the likely cause of the layers taking up non-equilibrium structures. The interfacial characteristics of $\{111\}_{fcc}:\{110\}_{bcc}$ interfaces have been studied extensively, beginning with the well known Nishiyama-Wasserman [74,75] and Kurdjumov-Sachs [76] relationships which characterize bcc:fcc epitaxy as $\{111\}_{fcc}//\{110\}_{bcc};<101>_{fcc}//<001>_{bcc}$ and $\{111\}_{fcc}//\{110\}_{bcc};<110>_{fcc}//<111>_{bcc}$ respectively. This analysis was furthered by Hall, Aaronson, and Kinsman [77], and Rigsbee and Aaronson [78] who found that a wide range of rotations around the $\{111\}_{fcc}:\{110\}_{bcc}$ normals could occur depending on the ratio of fcc to bcc lattice parameters. In all cases, only small regions of good matching at the interface can be achieved, separated by interfacial misfit dislocations and structural ledges. Consequently, the energies associated with the interfaces will be a function of the ratio of fcc and bcc lattice parameters. In the present study, it would appear that the fcc/bcc interfaces are close to the Kurdjumov-Sachs orientation as the <110> fcc zones are imaged simultaneously with the <111> bcc zones in the same columns. However, slight deviations from the actual zone axis [79] can be present and still result in HRTEM structural images as in figure 3.20. Thus, in practice, it can only be concluded that the observed interfaces are within ~ 4° of the Kurdjumov-Sachs orientation. As the Nishiyama-Wasserman orientation is actually only 5.27° from the Kurdjumov-Sachs orientation, it is impractical to distinguish these using HRTEM.

It is expected (and found) that both top and bottom Nb contacts have taken up their bulk bcc forms. As a result, both the first Cu layer and second Py layer will have
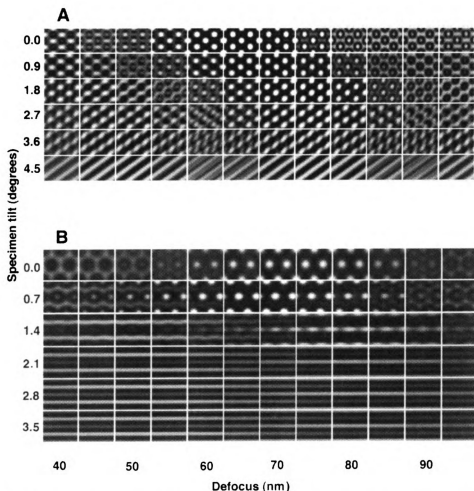
Figure 3.20 Bloch wave HRTEM simulations (using the same microscope conditions as in figure 3.12) of the effects of specimen tilt on the resulting image for a representative crystal viewed at various foci near Scherzer defocus. (A) fcc ($\approx$ 6 nm thick) Cu viewed along a <110> axis with the specimen tilted, progressively, parallel to the {111} growth planes. (B) bcc ($\approx$ 7 nm thick) Nb viewed along a <111> axis with the crystal tilted, progressively, parallel to the {110} growth planes. Although there is a distortion in the shape of the atom column images, the overall arrangement and lattice spacing remains unambiguous through at least 3.5 degrees of tilt for Cu and 1.4 degrees for Nb. (Images and analysis are provided by J.W. Heckman.)

misfit strains associated with their Nb interfaces if they take up their bulk fcc (and L1$_2$) crystal structures. These interfacial strains may be decreased if these layers instead take up non-equilibrium bcc structures. However, the decrease in strain energy is offset by an increase in the volume free energy associated with the non-equilibrium structure, and as the layer thickness increases, the volume free energy becomes dominant. In the case of Cu, it has been shown using full-potential muffin-tin orbital calculations [80] that the bcc structure has an energy only about 0.01 eV/atom greater than the equilibrium fcc form. Thus, the balance between bcc and fcc Cu might easily be shifted by interfacial strain. Mitchell, *et al.* [81] have used the critical thickness d$_c$ for the loss of coherency, which is the thickness at which the coherency of the interface begins to be disrupted by the requirement of interfacial dislocations, as a criterion for the point at which the crystal structure of a thin layer will revert to its equilibrium structure. This critical thickness has been given as:

$$d_c/b = (1/\alpha\varepsilon_o)[ln(d_c/b) + 0.5]$$

where b is the Burgers vector of the interfacial dislocations, ε_o is the misfit strain, and α is a geometric constant approximately equal to 4π. For Nb/Cu multilayers, Mitchell *et al.* [80] have determined this thickness to be only a few atomic layers, depending on the value of α. While this thickness was used as a general parameter for the point where the breakdown of the coherent Nb$_{bcc}$/Cu$_{bcc}$ would occur, it only considers the point at which dislocations will begin to be incorporated into the interface and does not consider the relative energies of the Nb$_{bcc}$/Cu$_{bcc}$ and Nb$_{bcc}$/Cu$_{fcc}$ interfaces. Thus, this parameter can give only a general indication of the point at which the interface loses coherency, which might lead to the transition from the non-equilibrium bcc to the equilibrium fcc structure

for the Cu. However, it does suggest that the thicknesses of the bcc Cu observed in the present study are well beyond that at which coherency should exist.

While the observation of bcc Cu may be surprising, it is not unprecedented. The first observation of bcc Cu was reported in 1973 by Goodman, Brenner and Low [82] for an Fe-1.4at%Cu alloy where coherent Cu precipitates up to 5.0 nm in diameter were identified in the bcc Fe matrix using field-ion microscopy. Since then, a number of other findings of fine-scale bcc Cu have been reported. Using reflection high energy electron diffraction (RHEED) Heinrich *et al.* [83] identified (001) oriented bcc Cu epitaxially grown on (001) bcc Fe. In Fe(001)/Cu(001)/Fe(001) trilayers, bcc Cu with thickness' between 6 and 12 monolayers (~0.9-1.8 nm) were grown. In Fe/Cu multilayers (60 bilayers) with 1.5 nm thick Fe layers Pizzini *et al.* [44] found Cu in the bcc form in layers up to 1.3 nm thick using x-ray adsorption spectroscopy (XAS). More recently, HRTEM has been used to characterize bcc Cu in Cu/Nb multilayers [81, 84]. In these studies, the bcc Cu was found to grow psudomorphically on the bcc Nb for Cu thickness up to 1.2 nm. For thicker layers, the Cu took up an fcc structure with a Kurdjumov-Sachs relationship with the Nb layers.

In contrast to the existence of bcc Cu at very fine scales that has been established, the scale observed in the present study is much larger. The two Cu bcc layers in the spin-valves are 10 and 20 nm thick, approximately an order of magnitude greater than previously observed. When the bcc FeMn and Py layers are considered in the spin valves, the total thickness of all of the non-equilibrium grain columns reaches approximately 44 nm in the spin-valve with 3 nm Py layers and 98 nm in the spin valves with thick Py layers. At present, it is not clear why the bcc structure exists to such large thicknesses in

these spin-valves.

Low target temperatures during sputtering might be suspected to contribute to the formation of non-equilibrium phases. However, these temperature variations do not seem to have influenced the formation of the bcc phases in the present study. Sputtering on targets with temperatures ranging from -65°C to +22°C have all resulted in some of the grain columns taking up non-equilibrium bcc structures. Mitchell *et al.* [81,84] suggests that the transformation from bcc to fcc in thin layers of Cu occurs martensitically, not diffusely. A low sputtering temperature would not be expected to restrict this transformation. It is worth noting that in the Nb/Cu multilayers [81,84] the bcc Cu was found to have a lattice parameter of 0.328 ± 0.007 nm, which is very close to the bulk value of bcc Nb of 0.331 nm. In the present study, the value of the lattice parameter of the bcc Cu measured from the FFTs is approximately 0.29 nm, close to calculated values of 0.287 and 0.296 nm [85,86]. This suggests that significantly more relaxation of the bcc Cu has taken place in the present study than in the Nb/Cu multilayers examined by Mitchell *et al.* [81,84].

Further, it is interesting to note that the bcc structures investigated here display a significant degree of stability. Neither the energy imparted by ion milling during thin foil preparation nor electron beam radiation during CTEM or HRTEM examination has resulted in rearrangement to the equilibrium fcc structure.

3.5 SUMMARY

Structures of Cu/Py GMR spin valves with different Py thickness sputtered at different temperatures have been characterized using HRTEM and CTEM complemented

with HRTEM image simulations and FFT analysis techniques. All of the spin valves displayed polycrystalline structures with columnar grains. The grains have grown on the close packed planes ($\{111\}$ planes in the bcc Nb contacts and $\{110\}$ planes in the fcc Cu, FeMn, and Py spin-valve layers) taking up a near Kurdjumov-Sachs $\{111\}_{fcc}//\{110\}_{bcc};<110>_{fcc}//<111>_{bcc}$ orientation relationship. The FFT analysis and HRTEM image simulations indicate that in some of the columnar grains, the Cu, FeMn, and Py take up non-equilibrium bcc structures, regardless of different layer thicknesses and sputtering temperatures. In these cases, the bcc Cu, FeMn, and Py layers grew on $\{110\}$ planes and were epitaxial with the Nb contacts.

CHAPTER IV

STRUCTURAL STUDIES OF POLYCRYSTALLINE Ag/Py GMR SPIN-VALVES

4.1 INTRODUCTION

In this chapter, results of the characterization of polycrystalline GMR spin-valves in the form of Ag/Py/Ag/Py/FeMn, sputtered either on to a Nb superconducting contact or directly on to a Si substrate, are presented.

The first sample of $[Ag_{10}/Py_3/Ag_{20}/Py_3/FeMn_8]_{nm}$ (with 3 nm Py layers) was produced by sequential dc magnetron sputtering onto a p-type (001) Si substrate with a duplex design as shown in figure 2.1. This sample was examined between the crossed Nb contacts and also on the adjacent Si substrate to investigate the effect of substrate material on the subsequent spin-valve layer growth. CTEM and HRTEM observations found that the first Ag (buffer) layer of the spin-valve grown directly on the Si substrate displayed an epitaxial single crystal, in contrast to the polycrystalline form seen between the Nb contacts. To further characterize this observed single crystal and to determine if this phase was unique to this particular sample or if the epitaxial phase is induced by the substrate, additional HRTEM and CTEM studies were performed on this first sample and other subsequently fabricated specimens. In addition, HREDS was used to qualitatively determine the chemical composition of the first Ag layer and the other individual layers of this spin-valve. The EDS spectra collected from the first Ag layer indicated the presence of a significant amount of indium, which may have been inadvertently sputtered on the Si substrate during the bottom Nb contact layer being deposited.

Three additional samples were fabricated under the same conditions as this first sample, but sputtered directly on an approximately 1 cm^2 area of Si substrate in the form $[Ag_{10}/Py_3/Ag_{20}/Py_3/FeMn_8//Nb_{20}]_{nm}$ and $[Ag_{10}/Py_x/Ag_{20}/Py_x//Nb_{10}]_{nm}$ with x = 6 nm or 24 nm. Further TEM investigations were performed on these structures to determine whether this phenomenon was reproducible or unique to the initial sample.

4.2 CTEM OBSERVATIONS

4.2.1 Spin-Valve Grown on the Nb Contact

Figure 4.1 shows a cross-sectional brightfield CTEM image of the $(Ag_{10}/Py_3/Ag_{20}/Py_3/FeMn_8)_{nm}$ spin-valve, with 3 nm Py layers, grown on a Nb superconducting contact. The figure clearly illustrates the Si substrate, both Nb contacts and the spin-valve. Note that, unlike the Cu/Py spin-valves, the individual layers within the spin-valve are resolvable due to the large differences in the average atomic numbers of the layer components (Z_{Ag} = 47, Z_{Py} = 27.7, and Z_{FeMn} = 25.5). Both the Nb contacts and the spin-valve were observed to be polycrystalline with columnar grains, oriented with the long axis in the growth direction. The grains had widths ranging up to 50 nm normal to the growth direction. This structure is consistent with that observed for Cu/Py spin-valves sputtered on Nb contacts [63].

4.2.2 Spin-Valves Grown Directly on the Si Substrate

Figure 4.2 shows a cross-sectional CTEM image taken from an area of the initial $(Ag_{10}/Py_3/Ag_{20}/Py_3/FeMn_8)_{nm}$ spin-valve with 3 nm Py layers grown directly on the Si substrate. As can be noted from the image, a significantly different morphology was
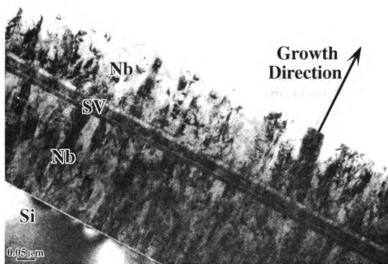
Figure 4.1 A cross-sectional brightfield CTEM image of the $[Nb_{250}//(Ag/Py/Ag/Py/FeMn)//Nb_{250}]_{nm}$ spin-valve with 3 nm Py layers grown on Nb. Note that the individual layers within the spin-valve can be distinguished.
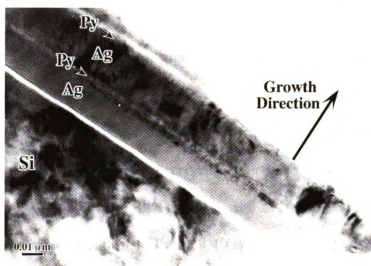
Figure 4.2 A cross-sectional brightfield CTEM image of the Ag/Py/Ag/Py/FeMn spin-valve with 3 nm Py layers grown directly on Si substrate showing the first Ag layer grew as a single crystal.

observed. The first Ag layer appeared as a continuous single crystal throughout the entire viewable area of the TEM sample, with the rest of the layers being polycrystalline and morphologically similar to the spin-valve grown on the Nb contact.

However, images of three similar spin-valve structures subsequently prepared on Si substrates do not show any layers with a similar single-grain growth pattern. An overall structure of another $(Ag_{10}/Py_3/Ag_{20}/Py_3/FeMn_8)_{nm}$ spin-valve (with 3 nm Py layers), grown directly on Si substrate, under the same sputtering conditions, was characterized using CTEM and is shown in figure 4.3. This spin-valve was polycrystalline throughout and morphologically similar to that seen in spin-valve layers grown between the Nb contacts in the first specimen. The individual layers within the spin-valves are, again, clearly visible (due to the contrast mechanisms described above) and appear continuous with uniform thicknesses. Additionally, a similar polycrystalline morphology was also observed in two other spin-valves of $(Ag_{10}/Py/Ag_{20}/Py/FeMn_8)_{nm}$ with 6 nm and 24 nm Py layers grown directly on Si substrates as shown in figure 4.4 (a) and (b). The epitaxial single crystal morphology was not found in either of these spin-valve samples.

4.3 HRTEM AND FFT ANALYSIS

4.3.1 Spin-Valve Grown on the Nb Contact

A cross-sectional HRTEM image of the $(Ag_{10}/Py_3/Ag_{20}/Py_3/FeMn_8)_{nm}$ spin-valve with 3 nm Py layers grown on the Nb contact is shown in figure 4.5. The sample was imaged with the Si substrate tilted to the <110> zone axis, which puts the (001) substrate plane and the spin-valve edge-on. The individual spin-valve layers can be distinguished clearly, even in sample areas thin enough to yield good HRTEM images, due to the above

82
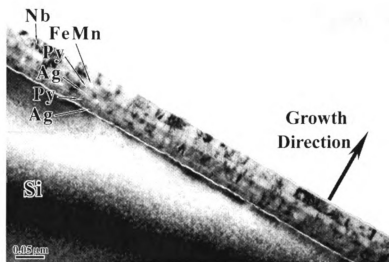
Figure 4.3 A cross-sectional brightfield CTEM image of a second Ag/Py/Ag/Py/FeMn/Nb multilayer with 3 nm Py layers grown directly on the Si substrate showing polycrystalline morphology with columnar grains for all the layers.
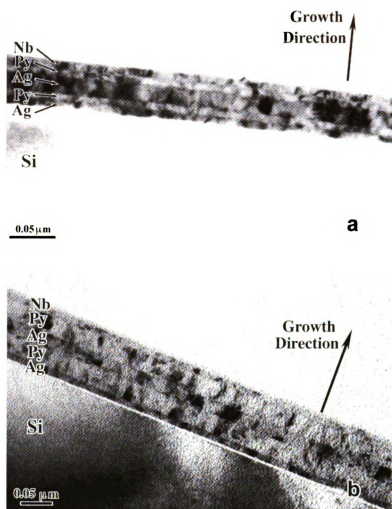
Figure 4.4 Cross-sectional bright field CTEM images of the Ag/Py/Ag/Py/Nb multilayers with (a) 6 nm Py layers and (b) 24 nm Py layers, grown directly on Si substrate showing polycrystalline morphology for all the layers.
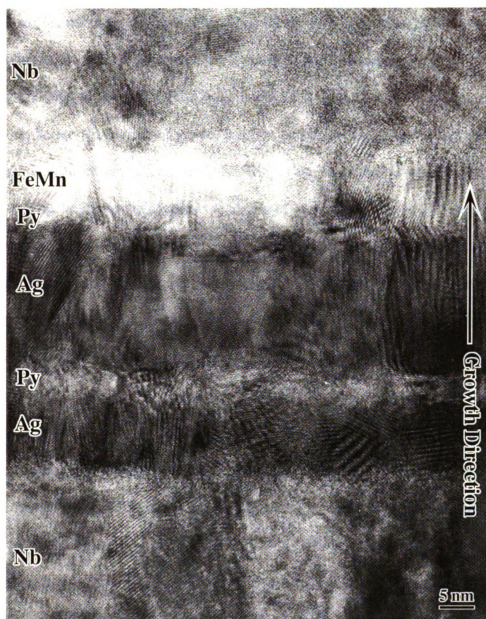
Figure 4.5 A cross-sectional HRTEM image of the first $(Ag_{10}/Py_3/Ag_{20}/Py_3/FeMn_8)_{nm}$ spin-valve, from an area between the Nb contacts. The individual layers are clearly distinguished due to the large differences in the average atomic numbers of the multilayer components.

mentioned range in Z of the layer materials. The observed period of the $[Ag_{10}/Py_3/Ag_{20}/Py_3/FeMn_8]_{nm}$ spin-valve layers in the image is consistent with that given by the nominal sputtered thickness (indicated in figure 4.5). As expected, only some of the grain columns are properly oriented for structural lattice imaging, because both the Nb contacts and the spin-valve exhibit a columnar polycrystalline morphology. However, continuous lattice fringes are observed, running perpendicular to the growth direction, in almost all of these columnar grains. These fringes run from the substrate to the top of the structure. This lattice fringe pattern is evidence of growth on close packed planes and of a highly textured structure. In grain columns suitably oriented for structural imaging, the lattice structure maintains an epitaxial morphology across the spin-valve layer interfaces. In addition to the lattice image contrast, numerous Moiré fringes appear in the image, due to overlapping of different grain columns in the plane of observation of the cross-sectional TEM samples.

It is difficult to obtain electron diffraction patterns directly from areas within grains in the individual spin-valve layers due to their small width normal to the beam. Therefore, fast Fourier transform (FFT) image analysis has been used to complement the interpretation of the HRTEM images. The fast Fourier transforms, taking the form of optical diffractograms of selected areas of the experimental HRTEM images, reveal equivalent plane spacing and angular information to electron diffraction patterns from those areas of the specimen. In this study, Nb or Si reflections were used as internal calibration standards to determine the effective camera lengths for interpreting the FFT diffractograms [63]. Based on these calibrations, the interplanar spacings and angles of the individual spin-valve layers were determined.

Portions of HRTEM images and FFT diffractograms for the $(Ag_{10}/Py_3/Ag_{20}/Py_3/FeMn_8)_{nm}$ spin-valve with 3 nm Py layers grown on Nb are shown in figure 4.6. In this case, the diffractogram of the Nb contact was first calibrated. The bottom Nb is characterized by 60° interplanar angles, indicating a <111> zone axis of bcc Nb. The {110} interplanar spacings from this layer were used as a standard to calculate an effective camera length for measuring subsequent diffractograms. In this bottom Nb contact the growth direction is close to <110>, indicating the growth has occurred on the closest packed bcc {110} planes. Using this Nb calibration, selected areas from the individual spin-valve layers have been analyzed as follows. Beginning with the first Ag layer, the resolvable zone is characterized by 55° and 70° interplanar angles. This indicates that this layer is imaged along a <011> zone axis and is found to display the fcc structure. The first reflections in the FFT diffractogram correspond to a real space interplanar spacing of 0.24 nm, which corresponds to the {111} planes of an fcc cell with a lattice parameter of 0.42 nm. This is very close to the bulk value of 0.41 nm for fcc Ag. A similar analysis applied to the second Ag layer also reveals it to be fcc. In both cases, the growth direction is near <111>, suggesting the close packed planes in the fcc Ag layers are epitaxial with the {011} closest packed planes in the bcc Nb. Subsequent analysis of the Py and FeMn layers also confirms these layers to be fcc structure[1] with <111> growth directions. The {111} interplanar spacings were measured to be 0.20 nm for Py and 0.21 for FeMn, which correspond to fcc lattice parameters of 0.35 nm (a_{Py} = 0.355nm in the Py bulk state) and

---

[1] Bulk Permalloy™ (Py) displays the fcc derivative $L1_2$ structure. However, because of the fairly small differences in the atomic scattering factors and because the Py used in this study is significantly off-stoichrometric, the superlattice reflections are very weak and do not appear on the FFT diffractograms. For the same reasons, the $L1_2$ ordering is not evident in the HRTEM images. Thus, for the purposes of this work, Py will be treated as fcc.
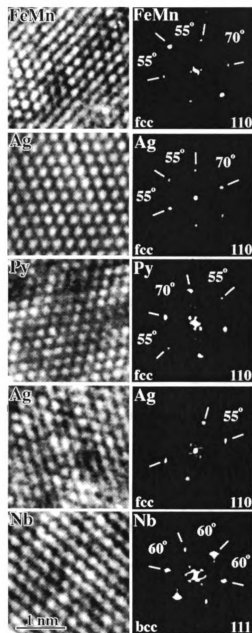
Figure 4.6 HRTEM images and FFT diffractograms of various layers of the $[Nb_{250}//(Ag_{10}/Py_3/Ag_{20}/Py_3/FeMn_8)//Nb_{250}]_{nm}$ spin-valve grown on Nb contact. All of the component layers display their equilibrium fcc (Ag, FeMn) or Ll_2 (Py) <110> zone patterns.

0.36 nm (a_{FeMn} = 0.363 nm in the FeMn bulk state) respectively.

4.3.2 Spin-Valve Grown Directly on the Si Substrate

A cross-sectional HRTEM image of the first $(Ag_{10}/Py_3/Ag_{20}/Py_3/FeMn_8)_{nm}$ spin-valve (with 3 nm Py layers) from an area grown directly on the Si substrate is shown in figure 4.7. It is evident that the crystal structure of the first Ag layer is quite different than that seen in those grown on the Nb contact (*cf.* figure 4.5). A thin amorphous region (probably SiO_2) is seen between the first Ag layer and the Si substrate. In this case the first Ag layer displays a single orientation throughout the entire region pictured (and throughout the entire thin area of the TEM sample). Epitaxial growth of (111) Ag on Si (001) has been reported and a mechanism for accommodating the lattice mismatch has been proposed, although the published single crystal domains were considerably smaller than those presented here [87]. However, this single, epitaxial layer also displays a striking contrast variation in the planes running parallel to the growth direction with a contrast period of every third atomic plane. All of the Ag non-magnetic layers in the present study had a nominal 10 nm thickness, as determined with a quartz crystal thickness monitor. However, this epitaxial layer appears approximately 45% thicker than both the nominal thickness sputtered and the Ag layer thickness found between the spin-valve and Nb contacts (figure 4.5). The rest of the spin-valve grown on this single crystal layer is polycrystalline and appears similar in morphology to the portion grown on the Nb contact.

The enlarged areas of the HRTEM images of both Ag layers and Si substrate, along with their corresponding FFT diffractograms are shown in figure 4.8. In this case (without the Nb contacts), the reflections from the Si substrate were used as internal calibration
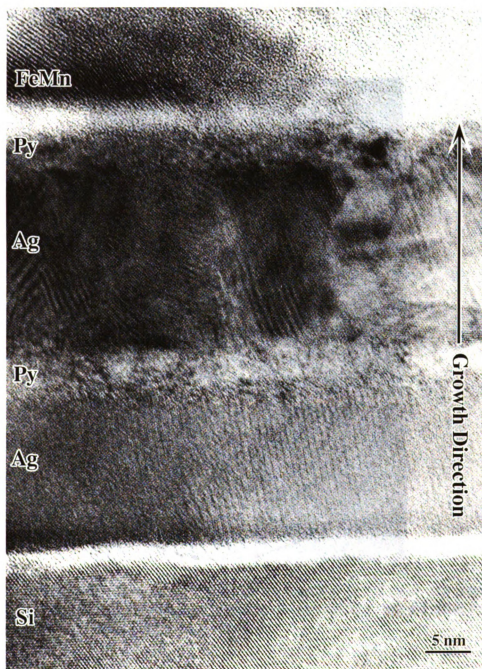
Figure 4.7 A cross-sectional HRTEM image of the $(Ag_{10}/Py_3/Ag_{20}/Py_3/FeMn_8)_{nm}$ spin-valve grown directly on Si. The first Ag layer displays a single orientation throughout the entire region of view (and throughout the entire thin area of the TEM sample).
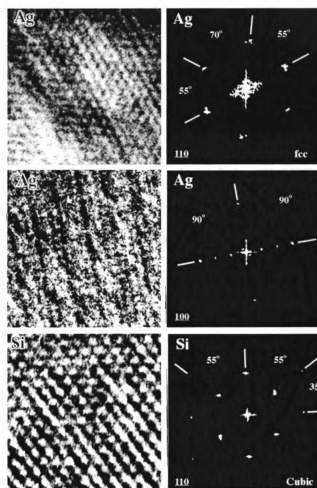
Figure 4.8 HRTEM images and FFT diffractograms of Si and Ag layers of the $(Ag_{10}/Py_3/Ag_{20}/Py_3/FeMn_8)_{nm}$ spin-valve grown directly on Si. The FFT from first Ag layer is inconsistent with an fcc equilibrium structure.

standards to determine the effective camera lengths for interpreting the FFT diffractograms of the Ag layer. Consistent with the contrast modulation noted from the HRTEM images, additional reflections at 1/3 and 2/3 of the primary reflection spacings are apparent in the directions perpendicular to the growth direction in the first Ag layer. The projected zone is characterized by 90° interplanar angles. If the additional 1/3 and 2/3 reflection spots were disregarded, the interplanar spacings of all four of the primary reflections would equal 0.23 nm. This spacing is consistent with the {111} interplanar spacing of 0.235 nm in bulk fcc Ag. However, the {111} planes cannot lie at 90° to one another. Thus, it appears this first layer is not an equilibrium fcc structure. Previous HRTEM studies of Cu/Py spin-valves showed that in some of the columnar grains, the Cu, Py and FeMn layers had been found taking up a non-equilibrium bcc structure [88]. In present situation, if the Ag had assumed a similar non-equilibrium bcc structure, the measured interplanar spacings (based on a hard sphere atomic radii calculated from the equilibrium fcc structure) would be consistent with those expected for {110} reflections (a_{Ag}^{bcc} = 0.334 nm thus $d_{110}^{bcc\ (Ag)}$ = 0.236 nm). These can easily be resolved in <100> orientation. However, packing density difference between the fcc and bcc structures (0.68 versus 0.74), alone, does not nearly account for the observed difference in the thickness of the first layer.

For comparison, a cross-sectional HRTEM image of the $(Ag_{10}/Py_3/Ag_{20}/Py_3/FeMn_8)_{nm}$ spin-valve with 24 nm Py layers grown directly on the Si substrate is shown in figure 4.9. Overall, the spin-valve has a morphology similar to the one grown on the Nb contact. The Si substrate, the spin-valve and top Nb layer can be distinguished clearly and the latter two appear to be polycrystalline, which is consistent with observed by CTEM study. The individual spin-valve layers are readily apparent and
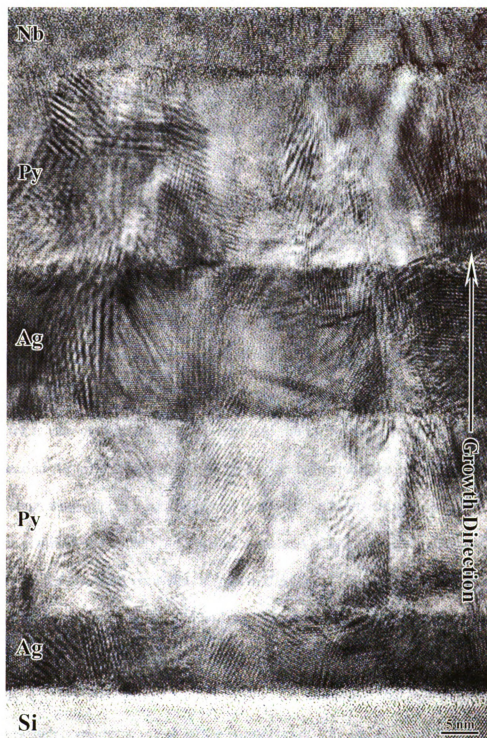
Figure 4.9 A cross-sectional HRTEM image of the $(Ag_{10}/Py_{24}/Ag_{20}/Py_{24}/Nb_{10})_{nm}$ multilayer grown directly on Si. The interfaces between the layers are sharp and flat, indicating less interfacial roughness and interdiffusion between the spin-valve components compared with the one grown on Nb.

their widths consistent with the nominal sputtered thicknesses. The selected areas of the HRTEM images and FFT diffractograms of the individual components are shown in figure 4.10. In this case (without the Nb contacts), again, the reflections from the Si substrate were used as internal calibration standards to determine the effective camera lengths for interpreting the FFT diffractograms of the rest spin-valve layers. As expected, the Si substrate is a single crystal grown on (100) plane. Using Si calibration, selected areas from the individual spin-valve layers have been analyzed as follows. The resolvable zone of the first Ag layer is characterized by 55° and 70° interplanar angles, indicating that this layer is imaged along a <011> zone axis and is found to display the fcc structure. The first reflections in the FFT diffractogram correspond to a real space interplanar spacing of 0.24 nm, which corresponds to the {111} planes of an fcc cell with a lattice parameter of 0.42 nm, which is very close to the bulk value of 0.41 nm for fcc Ag. A similar analysis applied to the second Ag layer also reveals it to be fcc. In both cases, the growth direction is near <111>, suggesting the close packed planes in the fcc Ag layers are epitaxial with the {100} substrate planes in the cubic Si. Subsequent analysis of both Py layers also confirms these layers to be fcc structure with <111> growth directions. The {111} interplanar spacings were measured to be 0.20 nm, which correspond to fcc lattice parameter of 0.35 nm (a_{Py}=0.355nm in the Py bulk state). The top Nb is characterized by 60° interplanar angles, indicating a <111> zone axis of bcc Nb. The {110} interplanar spacings were measured to be 0.23, which correspond to bcc lattice parameter of 0.33 nm (a_{Nb} = 0.331 nm in the Nb bulk state). The growth direction of this top Nb contact is close to <110>, indicating the growth has occurred on the closest packed bcc {110} planes. Therefore the FFT analysis indicated that the Ag, Py and Nb layers display their equilibrium fcc and bcc
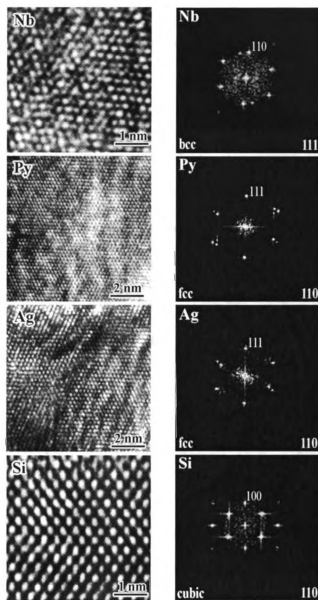
Figure 4.10 HRTEM images and FFT diffractograms of various layers of the $[(Ag_{10}/Py_{24}/Ag_{20}/Py_{24})//Nb_{10}]_{nm}$ spin-valve grown directly on Si. All of the component layers display their equilibrium fcc (Ag) or Ll$_2$ (Py) <110> and bcc (Nb) <111> zone patterns.

structures with <111> growth directions for fcc and <110> growth directions for bcc respectively.

4.4 HREDS RESULTS[2] (By J.W. Heckman)

After analysis by HRTEM, the first spin-valve sample (grown directly on the Si) was analyzed in the STEM. A brightfield STEM image of the area of the spin-valve analyzed by HREDS is presented in figure 4.11. The lighter areas in the micrograph (labeled) are due to an ablation of material and damage at each of the analysis points. X-ray spectra collected from the four points spanning the spin-valve are shown in figure 4.12. Figure 4.12 (A) is the spectrum from point A in figure 4.11, which is a reference spectrum that shows mainly a Si K family with a trace of O K and C K radiation. The spectrum from point B (figure 4.12 (B)) was captured within the single crystal first Ag layer. The edge of the beam ablated region for this analysis point is approximately 3 nm from the Ag layer /Py layer interface. The spectrum consists mainly of a series of L family peaks in the range of 2.5 to 4.5 keV and shows just a trace of Ni K^{α} and Cu K^{α} radiation. While this is the general range of values expected for the Ag L family, the relative intensities do not match those expected. If the contribution of the Ag L family is manually stripped from the spectrum (figure 4.12 (C)), the resulting series of peaks matches the distribution and intensities of Indium L peaks. Figure 4.12 (D) shows the spectrum obtained by positioning the probe directly on the first Py layer. The expected Fe and Ni peaks, with their intensities roughly consistent with the Py stoicheometry, dominate the spectrum. There is a persistence of the L family of lines from the Ag-In region, which is likely due to beam

---

[2] In order to have a better understanding of the structure of Ag/Py spin-valves, it is necessary to include HREDS analysis that was performed by John W. Heckman.
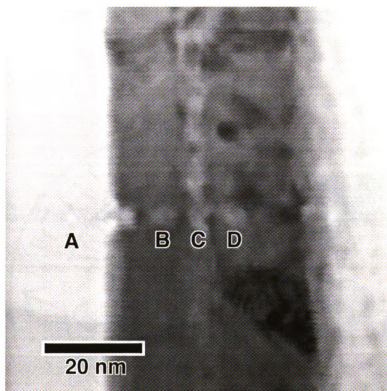
Figure 4.11 A cross-sectional brightfield STEM image of the initial Ag/Py spin-valve grown directly on the Si substrate. Points A-D indicate the loci of origin of the X-ray spectra acquired.
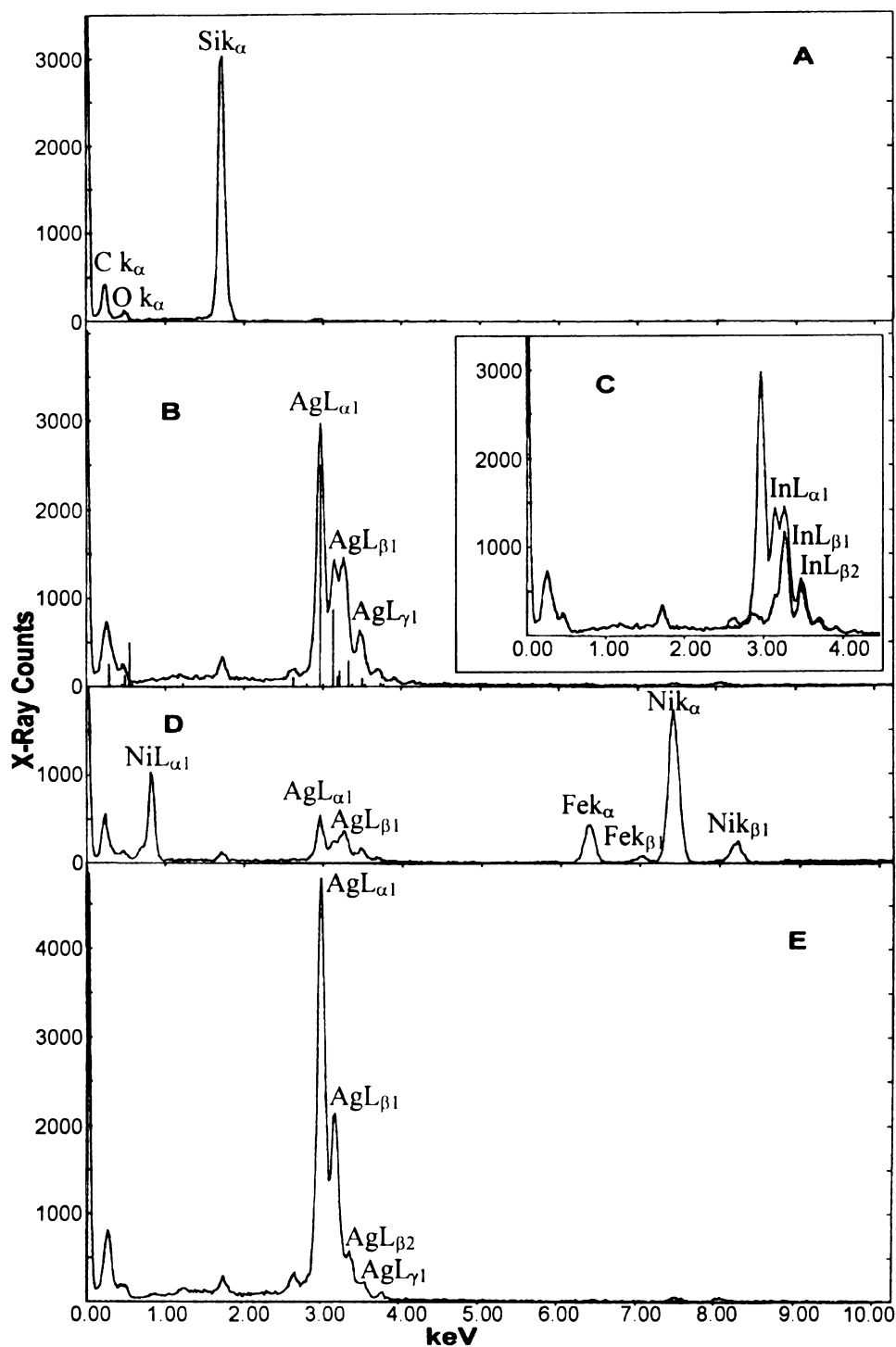
Figure 4.12 EDS X-ray spectra collected from the Si substrate and the first three layers of the Ag/Py spin-valve illustrated in Figure 4.11. (A) Spectrum collected from the silicon substrate. (B) Spectrum from the first Ag layer. (C) First Ag layer spectrum with the Ag L series contribution stripped. (D) Spectrum from the first (unpinned) Py layer. (E) Spectrum from the second Ag layer.

spreading, or beam overlap, of the layer boundary. In figure 4.12 (E), the beam was positioned on the polycrystalline (second) Ag layer. The spectrum obtained shows only the expected silver and residual O K and C K peaks with no evidence of indium.

The x-ray spectra of several discrete ratios of Ag:In were modeled to elucidate the stoicheometry in this region and the effect of altering this ratio on the resultant X-ray spectra can be seen in figure 4.13. The Ag_4:In ratio most closely matches the experimental data shown in figure 4.12 (B).

The observed differences in thickness of the first Ag layer when grown on Si versus Nb can almost be explained as follows: Not only is there an additional 20 atomic percent In in this layer, but based on the HRTEM images of this layer, it is reasonable to expect that the Ag-In phase is not a close packed structure. Thus, the observed dilatation of approximately 45% is not unreasonable. At present it has not been possible to reconcile the structure observed using HRTEM with any known Ag-In structures. According to the equilibrium phase diagram [89], compositions in the range of Ag_4In should lie in a two-phase field between the FCC Ag solid solution and the hexagonal ξ phase. Neither of these phases are consistent with the HRTEM images and FFTs of the observed phase, indicating that this layer is non-equilibrium in nature. As such, the source of the observed 3-fold contrast modulation in the single crystal structure of this layer is not clear.

The source of the In in the first Ag layer has not been unequivocally identified. However, indium is used as a solder in the sputtering target assemblies. Thus, it is likely that the indium contamination was a result of a small amount of excess In solder in the sputtering system. It is curious that the contamination only affected the Ag grown directly on the Si, but not on Nb. Thus suggests that the In may have contaminated the substrate
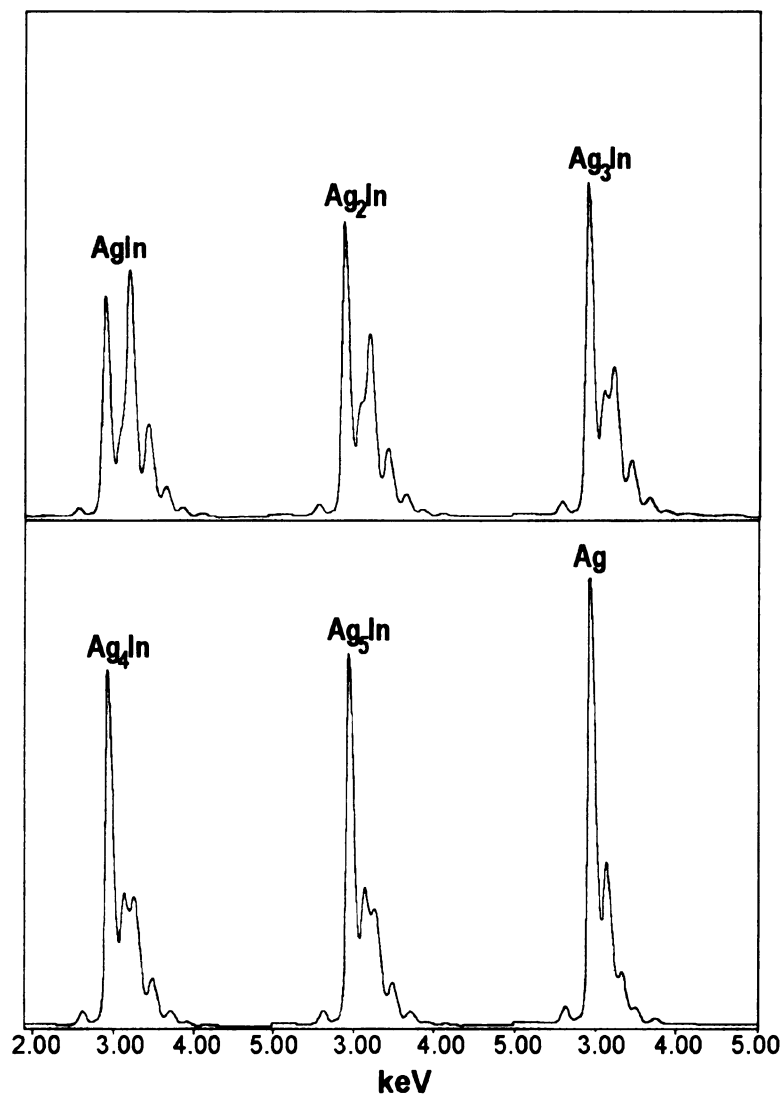
Figure 4.13 Simulated EDS spectra of simple stoicheometric ratios of Silver and Indium. The Ag_4:In ratio is the best integer match with the experimental spectrum.

during the sputtering of the bottom Nb layer. Unfortunately, sample limitations precluded EDS examination of the Si/Nb interface for the presence of In. It is important to note that no form of In contamination was observed in any of the other sputtered samples examined neither in this study nor in any other spin-valve studies to date.

Despite the accidental nature of how this Ag-In phase was produced, the fact that it grows epitaxially is intriguing. However, if this phase can be consistently grown, it may provide a basis for further epitaxial growth of additional structures that cannot be epitaxially grown directly on Si. In particular it may be possible to grow additional epitaxial layers in the Ag/Py spin-valve stack using this Ag_4In epitaxial layer as a buffer. As it is likely that this phase will be non-magnetic yet electrically conducting such an epitaxial buffer layer should not affect the magnetic nature of the spin-valve.

4.5 SUMMARY

The results here, in agreement with previous work, indicate that Ag/Py spin-valves show polycrystalline equilibrium structures throughout the device. Even at cross section thicknesses thin enough to allow HRTEM imaging, the Ag layers provide good contrast between adjacent layers. There appears to be no major differences between the spin-valves sputtered on the Nb contacts and those grown directly on the Si substrate. In one instance, when the spin-valve is grown directly on the Si substrate, the first Ag layer displayed an epitaxial single grain. HREDS has shown that this single crystal (epitaxial) layer is likely composed of Ag and In in a 4:1 atomic ratio. The In contamination may be due to the inadvertent sputtering or evaporation of target solder in the sputtering system prior to the Nb contact deposition. Indium contamination was only observed in this one

sample. In all other spin-valve samples examined to date, polycrystalline morphologies have been consistently observed regardless of substrate. If reproducible, epitaxial Ag_4In may be useful in growing epitaxial spin-valves or other structures on Si substrates.

CHAPTER V

STRUCTURAL STUDIES OF POLYCRYSTALLINE Cu/CoZr
GMR SPIN-VALVES

5.1 INTRODUCTION

In the previous two chapters, the details of the structural studies were focused on ferromagnetic Py based polycrystalline GMR spin-valves including Cu/Py and Ag/Py spin-valves. In this chapter, instead of a study of ferromagnetic Py based spin valves, ferromagnetic CoZr based spin valves of two different types will be investigated. One is a symmetrical exchange biased spin valve (EBSV) in the form of FeMn/CoZr/Cu/CoZr and the other is a hybrid spin valve with the nominal form of Py/Cu/CoZr/Cu. Both spin valves were characterized using CTEM.

5.2 CTEM OBSERVATIONS

Nb//Cu/FeMn/CoZr/Cu/CoZr/Cu//Nb EBSV (1043-7)

The symmetrical exchange biased spin valve in the nominal form of $(Nb_{250}//Cu_{10}/FeMn_8/CoZr_{20}/Cu_{20}/CoZr_{20}/Cu_{10}//Nb_{250})_{nm}$ was sputtered on a Si substrate. The cross-sectional brightfield and darkfield CTEM images of this Cu/CoZr spin valve are shown in figure 5.1 (a) and (b). In both images, the Si substrate, both Nb contacts, and spin valve multilayers, can be distinguished clearly. Unlike for the Cu/Py spin valves, the individual layers within the spin valve are also distinguishable. However, these layers are not clearly imaged as in the Ag/Py spin valves, due to the low mass and diffraction contrast between FeMn (Z = 25.5), CoZr (Z = 27.3), and Cu (Z = 29). All of the layers are continuous, smooth, and are uniform in thickness. The interfaces between
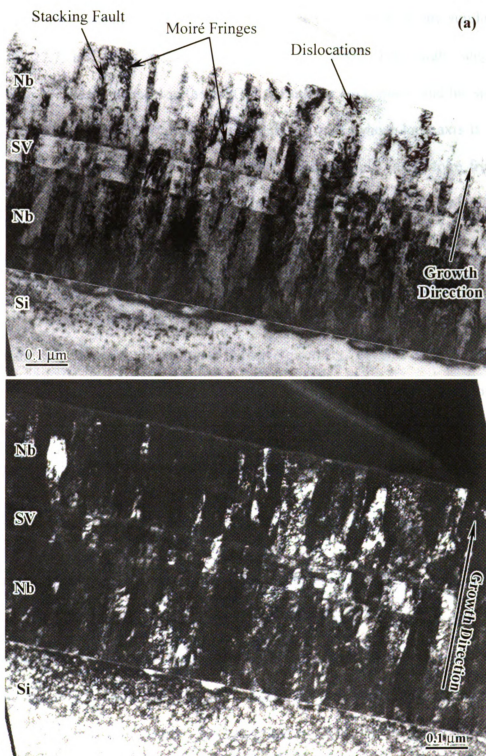
Figure 5.1 (a) Brightfield and (b) darkfield cross-sectional CTEM images of the $(Nb_{250}//Cu_{10}/FeMn_8/CoZr_{20}/Cu_{20}/CoZr_{20}/Cu_{10}//Nb_{250})_{nm}$ EBSV sputtered on Si substrate showing polycrystalline morphology with columnar grains.

the layers are straight and sharp when compared to the Cu/Py polycrystalline spin valves. This is interesting, because the Z differences in these two spin valves are similar (Z_{Cu} = 29, Z_{Py} = 27.7, and Z_{FeMn} = 25.5 for Cu/Py spin valves). This might suggest less intermixing or lower roughness in the Cu/CoZr. Both the Nb contacts and the spin valve were observed to be polycrystalline with columnar grains, whose long axis is oriented along the growth direction. Some dislocations, stacking faults, and Moiré fringes are observed in these columnar grains as indicated in figure 5.1 (a). The darkfield image more clearly illustrates that the sample grows mostly in a column morphology with grain widths ranging up to 50 nm normal to the growth direction. In most cases, epitaxy within these columns starts from the bottom Nb contact and continues into, and sometimes through the spin valve, all the way up to the top Nb contact. In some cases, at the Nb and spin valve interfaces, sudden changes in image intensity, due to changes in diffraction contrast, indicate significant changes in grain orientation and loss of strict epitaxy during the growth process. This morphology is consistent with that observed for polycrystalline Cu/Py and Ag/Py spin valves.

Nb//Cu/(Py/Cu/CoZr/Cu)×10/Cu//Nb Hybrid Spin Valve (1042-3)

The cross-sectional brightfield and darkfield CTEM images of the $(Nb_{250}//Cu_{10}/(Py_{24}/Cu_{20}/CoZr_{20}/Cu_{20})\times10/Cu_{10}//Nb_{250})_{nm}$ hybrid spin valve sputtered on Si substrate is shown in figure 5.2 (a) and (b). Again, the Si substrate, both Nb contacts, and the spin valve can be seen clearly. The individual layers within the spin valve are rather difficult to distinguish due to the small differences in the average atomic numbers of the

(a) SV: Cu//(Py/Cu/CoZr/Cu)x10/Cu
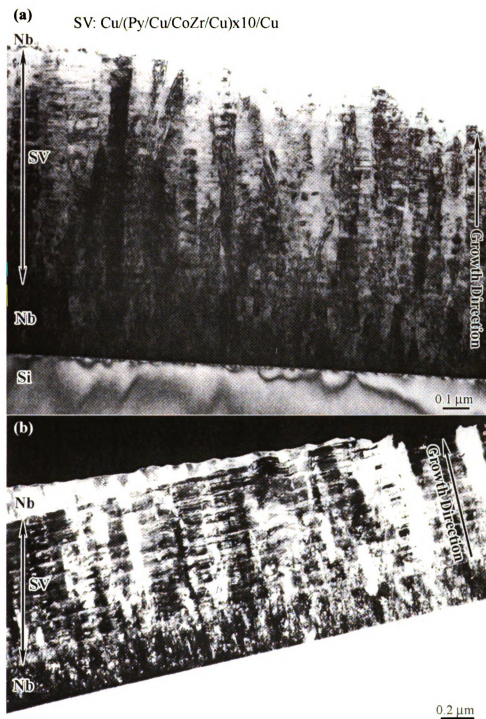
Figure 5.2 (a) Brightfield and (b) darkfield cross-sectional CTEM images of the $(Nb_{250}//Cu_{10}/(Py_{24}/Cu_{20}/CoZr_{20}/Cu_{20})\times10/Cu_{10}//Nb_{250})_{nm}$ hybrid spin valve sputtered on Si substrate showing polycrystalline morphology with columnar grains.

layer components ($Z_{Cu} = 29$, $Z_{Py} = 27.7$, and $Z_{CoZr} = 27.3$). The total thickness of the spin valve is consistent with its nominal thickness of 860 nm. It is evident that both Nb contacts and the spin valve are polycrystalline with columnar grains. Significant defects, such as stacking faults, Moiré fringes, and dislocations, result in substantial contrast in the columns. All the layers appear to be continuous with uniform thicknesses. It can also be seen clearly in the darkfield image that the diffraction contrast within the spin valve is consistent, with 10 quadrilayers of relative uniform thicknesses. In general, the quadrilayers are continuous and smooth. However, a number of bumps appear in some of the columns starting from the 5th quadrilayer and propagating all the way up to the top of the Nb contact, with increasing curvature towards the top. The source of these bump formations is not clear at this moment. HRTEM and analytical analysis are needed to further characterize these structures. Interestingly, the columns do not appear to get wider, high in the stack, unlike other previous cases (for example see figure 3.1). Possibly, for this hybrid spin valve, the widening occurs early in the stack, and reaches a stable point where all the columns are crystallographically/energetically the same. That is, the widening observed before (and possibly present in the first or second layer here) likely occurs from different columns growing preferentially at the expanse of others. Although the total thickness of this spin valve (860 nm) is much larger than all the ones previously studied (< 98 nm), epitaxy within the individual columns continues into and through the spin valve in most cases.

5.3 SUMMARY

The results here, in agreement with previous polycrystalline Cu/Py and Ag/Py CTEM observations, indicate that Cu/CoZr spin valves are polycrystalline with columnar grains for both EBSV and hybrid spin valve. Some defects, including dislocations, stacking faults, and Moiré fringes, are observed in both spin valves. However, in comparison to some previous polycrystalline exchange biased spin valves, the columns in the hybrid spin valve appear to grow straight up with uniform width.

CHAPTER VI

STRUCTURAL STUDIES OF EPITAXIAL GMR MULTILAYERS AND SPIN-VALVES GROWN BY DC SPUTTERING

6.1 INTRODUCTION

Initial structural characterization of GMR materials for magnetic devices concentrated on polycrystalline materials grown by dc magnetron sputtering, as discussed in last three chapters. Most of these multilayer incorporated Nb superconducting contacts, required for GMR measurements with the current perpendicular to the layer planes (CPP) geometry. Because of the non-equilibrium phases that were found in polycrystalline Cu/Py and Ag/Py multilayers and spin-valves, and because of the difficulties in imaging interfaces in polycrystalline samples, it is of interest to grow epitaxial magnetic multilayers and spin-valves instead of polycrystalline layers, to reduce structural defects associated with grain boundaries. However, as the program progressed, it became clear that growing such samples was not a trivial matter. Thus, the study became focused on assessing the structures of samples grown to be epitaxial. From a fundamental point of view, epitaxially grown samples should be useful for assessing the basic GMR parameters with respect to the film crystal structures. In general, molecular beam epitaxy (MBE) is widely used for growing epitaxial films. However sputter deposition offers higher growth rates and lower costs. In the present study, the group at MSU developed parameters to grow epitaxial CPP samples using sputter deposition. Through an iterative process, success has now been achieved in growing smooth epitaxial samples using this technique.

6.2 PRELIMINARY STUDIES ON EPITAXIAL SAMPLES

A preliminary study of epitaxial growth of GMR multilayers by magnetron sputtering was carried out by R. Loloee [33]. This study focused on determining the optimum growth techniques for epitaxial films on $(11\bar{2}0)$ sapphire substrates by sputter deposition, has shown partial success in growth of epitaxial Nb(110), Cu(111), Co(111), Py(111) films. That study characterized the films using atomic force microscopy (AFM) and electron backscatter patterns (EBSPs) [33]. AFM was used to characterize the surface topography while EBSPs were used to determine crystal structures, orientations, and growth epitaxy. The EBSP results showed that Nb films grow as high-quality epitaxial single crystals with $(110)_{bcc}$ orientations. The EBSP crystallographic characterization of Cu films revealed two in-plane twin variants corresponding to two different stacking sequences of {111} fcc planes. Subsequent growth of Co and Py films resulted in similar morphology. The orientation relationship between Nb and Cu was found to be the Nishiyama-Wasserman relationship. Although EBSPs can provide useful orientation information, it requires that films have a minimum effective film thickness of approximately 200 nm in order to be readily characterized. This film thickness is much greater than the thickness required for GMR devices (20 nm). Therefore, the details of the microstructure features of epitaxial magnetic multilayers and spin-valves need to be further characterized by high resolution microscopy such as CTEM and HRTEM.

A preliminary set of epitaxial Co/Cu multilayers was examined by J.W. Heckman [90]. In this study, the structures and composition of the epitaxial Nb//Cu/(Co/Cu)×6 multilayers were analyzed using CTEM, HRTEM, and HREDS. One of the conclusions reached was that when the Nb contact layer is deposited at high temperature and post

deposition annealed, a uniform epitaxially grown single crystal layer is formed with a high defect density as compared to the polycrystalline Nb layers, which are produced at room temperature. Another conclusion was that the structure of the Cu buffer layers of all the epitaxial samples deviates significantly from the nominal structure of the underlying Nb contact layer. Two different structural deviations were observed. For Cu deposition at low temperatures with post deposition annealing, the structure was continuous along a lateral direction (parallel to the base layer), but displayed a zone of composition variation at the interface of the Nb layer. For deposition at higher temperatures, formation of islands in the Cu buffer layer was observed. In the general case, the volume between islands was absent of any buffer material, and on some of the islands, there appear voids in the Cu buffer layer.

Successful methods for growing high quality epitaxial Nb contact layers on sapphire substrates were perfected by Loloee's research and confirmed by analysis and characterization performed by Heckman. However, attempts at growing high quality epitaxial layers of Cu, Py, and Co were not completely successful, particularly for the growth of the Cu buffer layer on the Nb contact layer which is the foundation for growing subsequent epitaxial films in a preferred orientation. Therefore, besides focusing on characterization of epitaxial multilayers and spin-valves, another objective of this study was to determine the correct parameters for growing a high quality Cu buffer layer on the epitaxial Nb contact.

6.3 ORIENTATION RELATIONSHIPS BETWEEN LAYERS DETERMINED BY EBSP [33]

EBSP is a straightforward approach for characterizing the orientation of the sputtered films. Loloee's research using EBSP determined the orientation relationship among the sapphire (Al_2O_3), Nb, and Cu layers. Although this information was obtained on samples with considerably thicker films than are typically used on an actual GMR device, the data were very useful as a guide for epitaxial relationships examined in further CTEM and HRTEM studies.

EBSP and AFM revealed that Nb films grow as high-quality epitaxial single crystals with (110) bcc single crystals. It has been shown that bcc Nb(110) planes can be grown epitaxially on sapphire (Al_2O_3) ($11\bar{2}0$) substrates [33]. EBSP results also revealed that Cu films grown on the epitaxial Nb contacts display two $\Sigma 3$ twin variants corresponding to different stacking orders of {111} fcc planes, i.e. ABCABC versus ACBACB. The two different orientation variants are also observed in Py and Co films.

The EBSP derived stereographic projections of the epitaxial Cu film and the epitaxial Nb under layer as well as Al_2O_3 substrate are shown in figure 6.1. It can be seen that the epitaxial relationship between Nb and Al_2O_3 was $(110)_{bcc}Nb \parallel (11\bar{2}0)Al_2O_3$ with $[1\bar{1}1]Nb \parallel [0001]Al_2O_3$ and $[1\bar{1}\bar{2}]Nb \parallel [1\bar{1}00]Al_2O_3$. The subsequent epitaxial relationship between the bcc Nb and fcc Cu variants was found to be $(110)_{bcc}Nb \parallel (111)_{fcc}Cu$, with $[001]_{bcc}Nb \parallel [0\bar{1}1]_{fcc}Cu$ and $[1\bar{1}0]_{bcc}Nb \parallel [2\bar{1}\bar{1}]_{fcc}Cu$, which is the well-known Nishiyama-Wasserman (N-W) relationship [91]. This relationship is different from that reported in section III of this dissertation on polycrystalline samples sputtered at room temperature, which used HRTEM imaging to show that the Nb/Cu

Figure 6.1 Stereographic projections of Al_2O_3, Nb, and Cu films. The epitaxial relationship between the Nb films and Al_2O_3 substrates was $(110)Nb \parallel (11\bar{2}0)Al_2O_3$ with $[111]Nb \parallel [0001]Al_2O_3$, while the epitaxial relationship between the bcc Nb and fcc Cu variants was the Nishiyama-Wasserman (N-W) relationship.
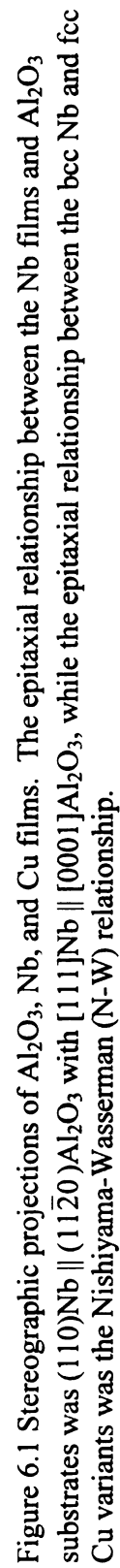
orientation relationship was close to the Kurdjumov-Sachs (K-S) relationship $(110)_{bcc}Nb$ || $(111)_{fcc}Cu$ with $[1\bar{1}1]_{bcc}Nb$ || $[0\bar{1}1]_{fcc}Cu$.

6.4 CTEM OBSERVATIONS

6.4.1 The Initial Series of Epitaxial Samples

Nb//Cu/Py/FeMn//Nb Multilayer (31-2)

The first epitaxial sample was grown in the nominal form of $(Nb_{250}//Cu_{100}/Py_{100}/FeMn_{50}//Nb_{100})_{nm}$. For this sample, the Cu buffer layer was grown at 150°C and post-annealed at 350°C; the Py layer was then grown at 350°C; no heat was applied during the growth of the rest of layers (FeMn and top Nb layers). A cross-sectional brightfield/darkfield image-pair of this epitaxial Cu/Py multilayer is shown in figure 6.2 (a) and (b). The sapphire substrate, both Nb contacts, and the spin-valve multilayer can be distinguished clearly. The individual layers are well defined and consistent with their nominal thicknesses. It can be seen that both bottom Nb and the spin-valve display epitaxial morphology which shows a single crystal Nb spanning the image, while the Cu, Py, and FeMn regions appear as large grains, up to 1 μm wide. Significant grooving appears between these grains, suggesting island growth of the Cu region with subsequent disruption of the Py and FeMn layers. In the darkfield image, different contrast is evident in the Cu, Py, and FeMn layers, which indicates orientation variants exist in these layers. In the first Cu buffer layer, it can be seen that there are some voids and discontinuities, suggesting poor epitaxial Cu layer grown on the Nb. A different morphology can be seen in comparison to that of the cross-sectional brightfield/darkfield image-pair of a polycrystalline Cu/Py spin-valve as shown
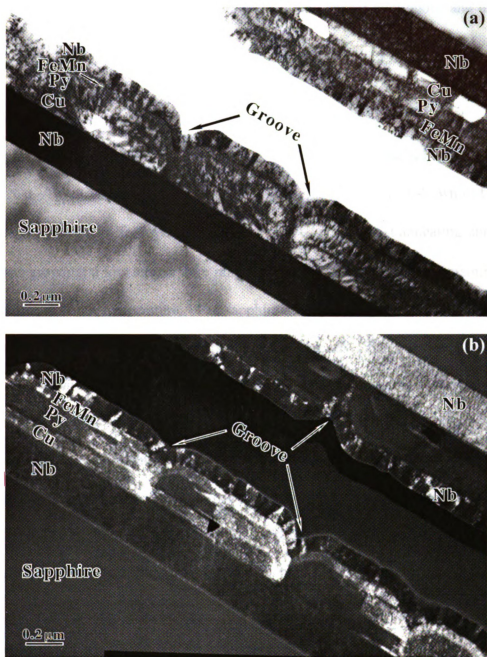
Figure 6.2 (a) Brightfield and (b) darkfield cross-sectional CTEM images of the epitaxial $(Nb_{200}//Cu_{100}/Py_{100}/FeMn_{50}//Nb_{100})_{nm}$ multilayer.

in figure 6.3 (a) and (b). In this polycrystalline sample, the Si substrate, the Nb contacts, and the spin-valve can all be clearly distinguished and appear continuous and uniformly thick with columnar growth.

Nb//Cu/Py/Cu/Py/FeMn//Au/Nb/Au Spin-valve (27-3)

A cross-sectional brightfield and darkfield CTEM image-pair of an epitaxial $[Nb_{250}//Cu_{20}/Py_{24}/Cu_{20}/Py_{24}/FeMn_8//Au_{15}/Nb_{100}/Au_{15}]_{nm}$ spin-valve is shown in figure 6.4 (a) and (b). The Cu buffer layer was grown at 450°C with no post annealing; the first Py layer was grown at a low temperature ranging from 80°C to 100°C; the remaining layers were grown at room temperature. The sapphire substrate, the two Nb contacts, both of the Au layers, and the spin-valve layers can be seen clearly. The individual Cu, Py, and FeMn spin-valve layers are relatively distinguishable and consistent with their nominal thicknesses. Similar with the first epitaxial Cu/Py/FeMn multilayer sample, a single crystal of Nb spans the image, while the Cu, Py, and FeMn layers appear as single crystals as well. The Au and top Nb contacts appear polycrystalline as expected. Only minor grooving is observed in this sample, but some voids and discontinuities appear in the Cu buffer layer, suggesting poor epitaxial Cu buffer layer grown on Nb.

Nb//Cu/Co/(Cu/Co)×20//Au/Nb/Au Multilayer (28-3)

A cross-sectional brightfield and darkfield CTEM image-pair of an epitaxial $[Nb_{250}//Cu_{20}/Co_{1.5}/(Cu_2/Co_{1.5})\times20//Au_{15}/Nb_{100}/Au_{15}]_{nm}$ multilayer is shown in Figure 6.5. For this sample, the Cu buffer layer was grown at 350°C with no post annealing; the first
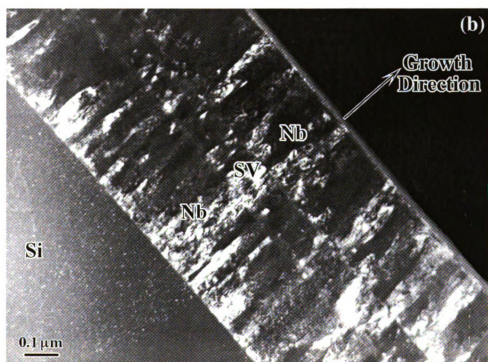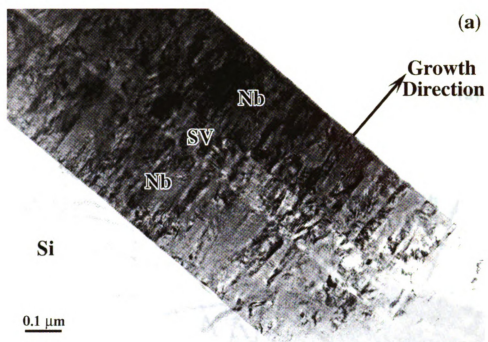
Figure 6.3 (a) Brightfield and (b) darkfield cross-sectional CTEM images of the polycrystalline $(Nb_{250}//Cu_{10}/FeMn_8/Py_{30}/Cu_{20}/Py_{30}/Nb_{250})_{nm}$ spin-valve.

Figure 6.4 (a) Brightfield and (b) darkfield cross-sectional CTEM images of the epitaxial $(Nb_{250}//Cu_{20}/Py_{24}/Cu_{20}/Py_{24}/FeMn_8//Au_{15}/Nb_{100}/Au_{15})_{nm}$ spin-valve.
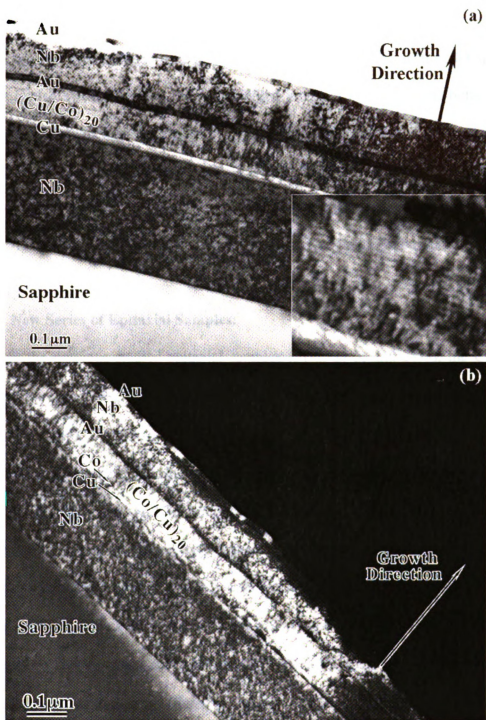
Figure 6.5 (a) Brightfield and (b) darkfield cross-sectional CTEM images of the epitaxial $(Nb_{250}//Cu_{20}/Co_{1.5}/(Cu_2/Co_{1.5})\times20//Au_{15}/Nb_{100}/Au_{15})_{nm}$ multilayer.

Co layer was grown at 400°C; no heat was applied during the growth of the remaining layers. The sapphire substrate, the Nb contact layers, both Au layers, and the Cu/Co bilayers can be readily distinguished. A weak contrast modulation in the 20 Cu and Co bilayers is also evident (see the inset of enlarged image in Fig. 6.5). The bottom single crystal Nb shows diffraction contrast consistent with a large number of dislocations. The Cu and Co layers appear single crystal as well. The Au and Nb contacts appear as polycrystalline as expected. A small amount of grooving also appears between these grains. Again, some voids and discontinuity are displayed in the Cu buffer layer.

6.4.2 A New Series of Epitaxial Samples:

In the previous studied epitaxial samples (31-2, 27-3, and 28-3), the Cu buffer layer was grown either at low temperature (150°C) then post-annealed at a relatively high temperature (350°C) or grown at a relatively high temperature (350°C or 450°C) with no annealing. Poor epitaxial morphology was observed in all these samples, especially for the Cu buffer layer grown on Nb. Loloee's AFM studies of similar samples have shown that the surface topography is strongly affected by the temperature and surface quality of the substrates. AFM images and line trace surface analyses show relatively smooth surfaces on 150 nm thick Cu films deposited at a substrate temperature of 475°C, and on 75 nm thick Cu films deposited at 150°C. All of the Cu films that were post-annealed displayed rougher surface. Therefore, based on these AFM studies and CTEM observations, it was decided that a new series of samples was needed to fully determine the effect of temperature on epitaxial growth.

To obtain good epitaxial Cu films grown on Nb, four new samples were fabricated, two with a high deposition temperature (500°C), and two with low deposition temperatures (100°C and 150°C). None of the samples were subjected to post-annealing.

6.4.2.1 Epitaxial samples grown at high deposition temperature

Nb//Cu/Py Multilayer (41-3)

A cross-sectional brightfield CTEM image of the $(Nb_{200}//Cu_{100}/Py_{200})_{nm}$ multilayer is shown in figure 6.6. For this sample, the Cu buffer layer was grown at 500°C and received no post-deposition annealing, while the Py layer was grown over a low temperature range from 80°C to 100°C. Similar with the first epitaxial sample (31-2), the Nb contact layer appears as a single crystal and spans the image, while the Cu and Py regions appear as large grains. Significant irregular grooving and a discontinuous morphology appear between these Cu and Py grains. The image also shows that the Cu buffer layer and Py layer were broken into islands, suggesting pin holes may occur in these layers and cause the potential for electrical shorts which should be avoided in magnetic devices. In some areas, the Cu buffer layer appears to be absent, with the Py layer in direct contact with the Nb layer. Some voids and dislocations are displayed in the Cu buffer layer. In the epitaxial Py layer, dark mottled contrast appears throughout the layers. This contrast is consistent with the effects of a very high density of dislocations and stacking fault fringes.
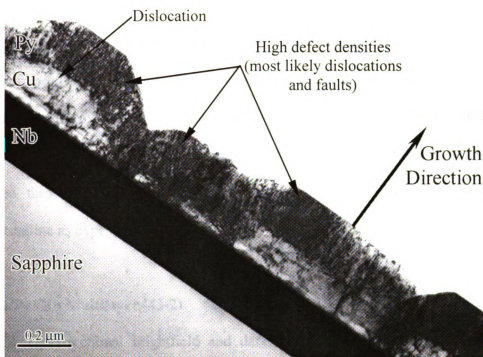
Figure 6.6 A cross-sectional brightfield CTEM image of the epitaxial $(Nb_{200}//Cu_{100}/Py_{200})_{nm}$ multilayer with Cu deposited at 500°C showing the poor epitaxial growth of Cu and Py layers.

6.4.2.2 Epitaxial samples grown at low deposition temperature

Nb//Cu/Py//Nb Multilayer (43-1)

Homogeneous and smooth epitaxial Cu layers grown on Nb were found in the multilayers when the Cu films were deposited at low temperatures (100°C and 150°C), and the rest of the layers were deposited at room temperatures. A cross-sectional brightfield CTEM image of the epitaxial $(Nb_{200}//Cu_{20}/Py_{20}//Nb_{20})_{nm}$ with Cu deposited at 100°C is shown in figure 6.7. The sapphire substrate, both Nb contacts, Cu, and Py layers can be distinguished clearly. It can be seen that all the layers are continuous, smooth and uniform in thickness, and no grooves or voids appear in the Cu buffer layer. The bottom Nb, Cu, and Py layers display epitaxial growth. Some dislocations are observed throughout the entire view of the cross-sections. The top Nb layer is polycrystalline as expected.

Nb//Cu/Py//Nb Multilayer (43-2)

A cross-sectional brightfield and darkfield CTEM image-pair of an epitaxial $(Nb_{200}//Cu_{20}/Py_{20}//Nb_{20})_{nm}$ multilayer with Cu deposited at 150°C is shown in figure 6.8. The sample was oriented with electron beam parallel to sapphire (0001) zone axis. It is evident that all the layers are continuous, smooth, and uniform in thickness. There are no grooves or voids in the Cu buffer layer. The bottom Nb, Cu, and Py layers display epitaxial growth throughout the entire view of the cross-sections. The top Nb layer is polycrystalline as expected. The inset shows the diffraction pattern of the entire multilayer which contains the Nb, Cu, and Py reflections. Only faint Cu and/or Py twin
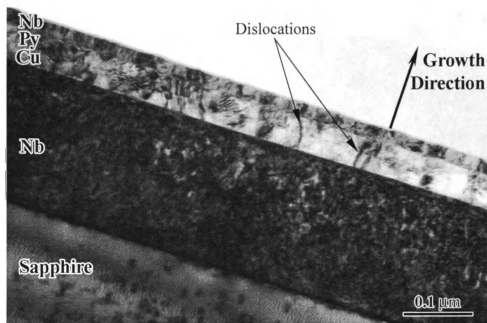
Figure 6.7 A cross-sectional brightfield CTEM image of the epitaxial $(Nb_{200}//Cu_{20}/Py_{20}//Nb_{20})_{nm}$ multilayer with Cu deposited at 100°C and rest of the layers deposited at room temperature. It shows the high-quality epitaxial growth of Cu and Py layers.
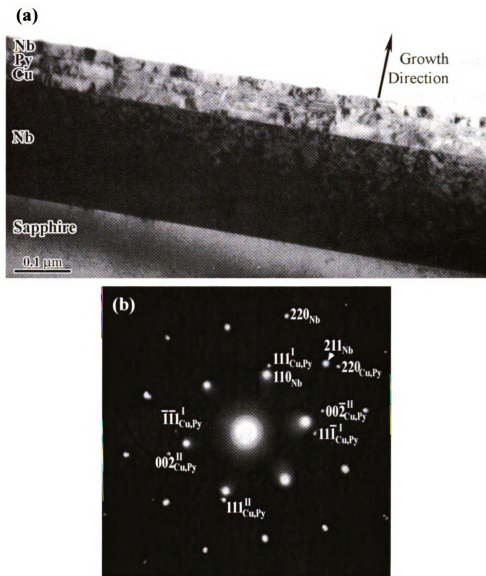
Figure 6.8 (a) A cross-sectional brightfield CTEM image of the epitaxial $(Nb_{200}//Cu_{20}/Py_{20}//Nb_{20})_{nm}$ multilayer with Cu deposited at 150°C and the rest of the layers deposited at room temperature. It shows high-quality epitaxial growth of Cu and Py layers. (b) The diffraction pattern taken from Nb-Cu-Py shows a portion of the <110> twin reflections of Cu and Py.

reflections appear in the pattern. From EBSP studies, it is known that there is an orientation relationship between Nb and Cu with 5.26° between the $(110)_{Nb}$ and $(111)_{Cu}$ directions (see figure 6.1). Therefore, to show the full <110> twin pattern of the Cu, the sample was tilted about 5° parallel to the growth planes. A cross-sectional brightfield and darkfield CTEM image-pair and corresponding diffraction pattern of the sample after tilting is shown in figure 6.9. It is now very clear that there are two different orientations in the Cu and Py layers. In the darkfield image, the two variants are more evident. Both the Cu(111) and Py(111) planes appear to be epitaxially grown on the single crystal Nb(110) layer. The diffraction pattern in figure 6.9 (c) shows two complete sets of the <110> twin pattern. This figure indicates that the Cu and Py layers were grown as two variants, consistent with the EBSP results.

A cross-sectional brightfield and darkfield CTEM image-pair of the same sample taken in the $(1\bar{1}00)$ zone axis of the sapphire is shown in figure 6.10. Again, all the layers can be distinguished clearly and display continuous and smooth structure and are uniform in thickness. No grooves or voids appeared in the Cu buffer layer. The inset diffraction pattern of the entire multilayer shows that $(110)_{bcc}$Nb is epitaxially grown on $(11\bar{2}0)_{hcp}Al_2O_3$ substrate, while $(111)_{fcc}$Cu and $(111)_{fcc}$Py are epitaxially grown on $(110)_{bcc}$Nb. No twin reflections were observed in this diffraction pattern.

6.4.3 Epitaxial Samples of Nb//Py/Cu//Nb Multilayers (43-3 and 43-4)

Two epitaxial samples were sputtered by growing Py on top of the epitaxial Nb contact instead of a Cu buffer layer: one was deposited at 150°C, and the other was
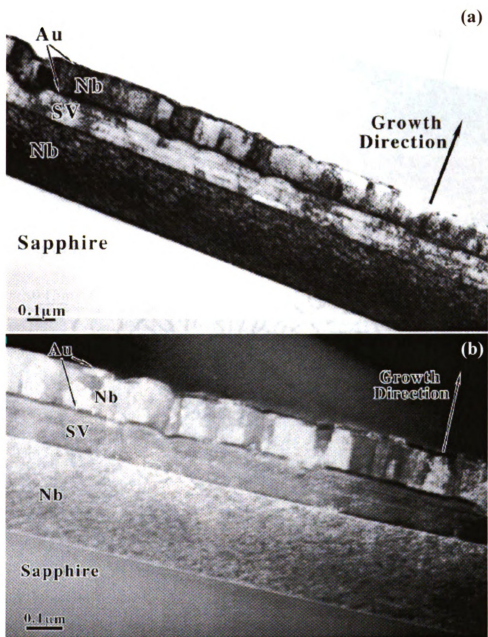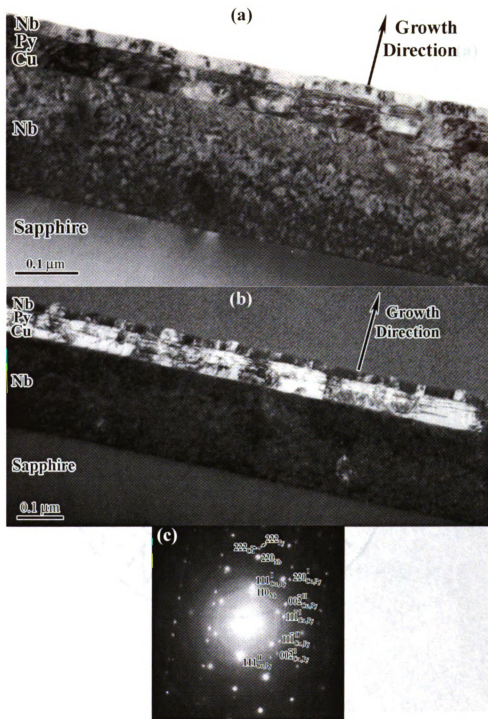
Figure 6.9 (a) Brightfield and (b) darkfield cross-sectional CTEM images of the epitaxial $(Nb_{200}//Cu_{20}/Py_{20}//Nb_{20})_{nm}$ multilayer with Cu deposited at 150°C showing the high-quality epitaxial growth of Cu and Py layers. The sample was tilted about 5° parallel to the growth planes. (c) The diffraction pattern is taken from Nb-Cu-Py layers which shows the full <110> twin pattern of Cu and Py after tilting.
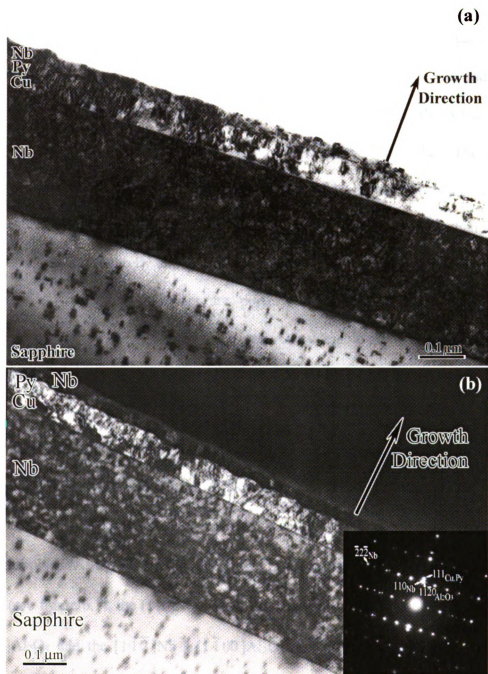
Figure 6.10 (a) Brightfield and (b) darkfield cross-sectional CTEM images of the epitaxial (Nb$_{200}$//Cu$_{20}$/Py$_{20}$//Nb$_{20}$)$_{nm}$ multilayer with Cu deposited at 150°C. The inset diffraction pattern shows the sample was oriented to the ($1\bar{1}00$) zone of sapphire substrate.

deposited at 350°C. Neither of these samples were post annealed. Figure 6.11 shows a cross-sectional brightfield CTEM image of (Nb_{200}//Py_{20}/Cu_{20}//Nb_{20})$_{nm}$ multilayer with Py deposited on Nb at 350°C. It is evident that irregular and rough grooves appear in the Py, Cu, and top Nb layers. It is difficult to distinguish the individual Py, Cu, and top Nb layers. A cross-sectional brightfield CTEM image of (Nb_{200}//Py_{20}/Cu_{20}//Nb_{20})$_{nm}$ multilayer with Py deposited on Nb at 150°C as shown in figure 6.12. The sapphire substrate, the top and bottom Nb contacts, the Py and Cu layers can all be clearly distinguished. The individual layers are well defined and consistent with their nominal thicknesses. However the Py and Cu layers do not appear to have epitaxial morphology as expected. Instead both layers are polycrystalline with large columnar grains throughout the entire view of the cross-sections. Considerable grooving appears between these grains.

6.5 HRTEM STUDIES AND FFT ANALYSIS

6.5.1 Epitaxial Nb Grown on Sapphire Substrates

The (110) Nb contacts were the first successfully grown epitaxial layers on the ($11\bar{2}0$) sapphire (Al_2O_3) substrates. As shown in the stereographic projections of Al_2O_3 and Nb (see figure 6.1), the (110)Nb and ($11\bar{2}0$)Al_2O_3 planes are parallel with [$1\bar{1}1$]Nb ∥ [0001]Al_2O_3 and the [$1\bar{1}\bar{2}$]Nb ∥ [$1\bar{1}00$]Al_2O_3 directions. Both of these directions offer a potential imaging axis, and cross-sections can be cut along either orientation.

A cross-sectional HRTEM image of the Nb-Al_2O_3 interface in the Cu/Py/FeMn multilayer is shown in figure 6.13. The Cu buffer layer was grown at 150°C and post-
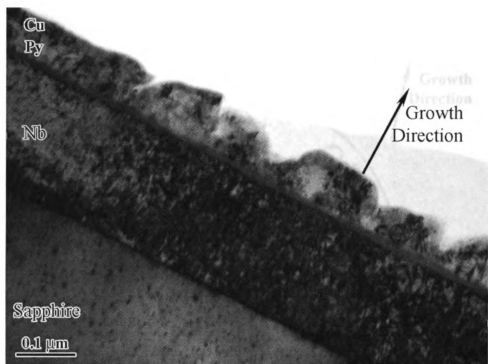
Figure 6.11 A cross-sectional brightfield CTEM image of the epitaxial $(Nb_{200}//Py_{20}/Cu_{20}//Nb_{20})_{nm}$ multilayer with Py deposited at 350°C on Nb showing poor epitaxial growth of the Py and Cu layers when Py grew on Nb first instead of Cu.

Figure 6.12 A cross-sectional brightfield CTEM image of the epitaxial $(Nb_{200}//Py_{20}/Cu_{20}//Nb_{20})_{nm}$ multilayer with Py deposited at 150°C on Nb showing the polycrystalline growth of the Py and Cu layers when Py grew on the Nb first instead of Cu.
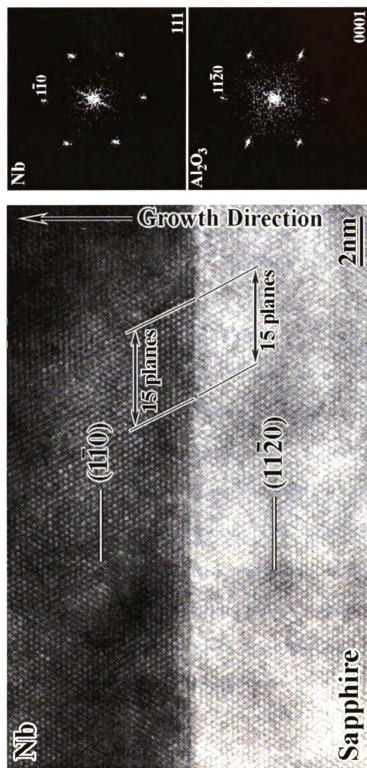
Figure 6.13 Cross-sectional HRTEM image of the Nb-Al$_2$O$_3$ interface and corresponding FFT patterns of the Nb and Al$_2$O$_3$ in the Cu/Py/FeMn multilayer, showing epitaxial single crystal ($1\bar{1}0$) Nb has grown epitaxially on the ($11\bar{2}0$) Al$_2$O$_3$ substrate.

deposition annealed at 350°C; the Py layer was then grown at 350°C; and no heating applied during the growth of the rest of the layers. The cross-section was oriented with the electron beam parallel to the [0001] Al_2O_3 direction. It can be seen that the Nb layer displays a single crystal morphology, consistent with the CTEM observations. The Nb-Al_2O_3 interface is structurally coherent, sharp, and defect free. The lattice planes transfer continuously from Al_2O_3 to Nb as indicated in the figure with no obvious epitaxy dislocations. The corresponding FFT diffractograms (see right column of figure 6.13) show a <111> zone in Nb aligned along the [0001] zone of the Al_2O_3, and show that the single crystal Nb has grown with the $(1\bar{1}0)$ planes epitaxial to the $(11\bar{2}0)$ Al_2O_3 substrate, consistent with the EBSP results.

A cross-sectional HRTEM image of the Nb-Al_2O_3 interface oriented with the electron beam parallel to the $[1\bar{1}00]$ Al_2O_3 direction is shown in figure 6.14. The lattice image also shows that the interface is atomically sharp and flat. The corresponding FFT analysis shows a <112> zone in Nb aligned along the $[1\bar{1}00]$ zone of the Al_2O_3, and shows that the single crystal Nb has grown with the (110) planes epitaxially to the $(11\bar{2}0)$ Al_2O_3 substrate, also consistent with the EBSP results. The (110) Nb planes and $(11\bar{2}0)$ Al_2O_3 planes lie parallel to the interface as indicated in the image. Only the (110) Nb planes with a spacing of 0.233 nm are resolvable due to the resolution limits of the microscopy. The (222) lattice planes, which have a spacing of 0.095 nm, is below the information limit of the JEOL-4000EX microscope used.
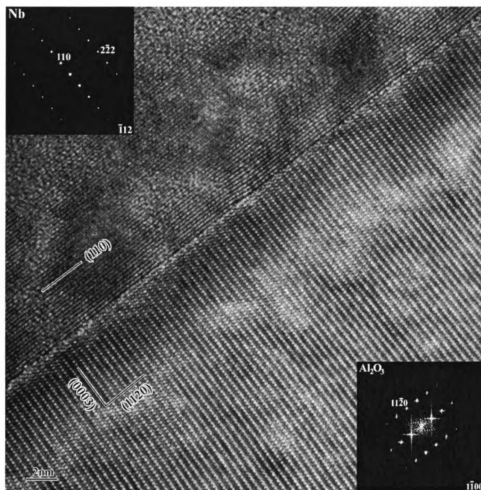
Figure 6.14 A cross-sectional HRTEM image of the Nb-Sapphire interface and corresponding FFT patterns of the Nb and sapphire in the Cu/Py/FeMn multilayer, showing epitaxial single crystal $(1\bar{1}0)$ Nb has grown epitaxially on $(11\bar{2}0)$ sapphire substrate.

6.5.2 Nb//Cu/Py/FeMn//Nb Multilayer (31-2)

A cross-sectional lattice image of the Cu-Nb interface in the Cu/Py/FeMn multilayer is shown in figure 6.15. The Cu buffer layer was grown at 150°C and post-annealed at 350°C, the Py layer was grown at 350°C, with no applied heat during the growth of the rest of layers. There are multiple small twins in the Cu region growing from the nucleation interface. As labeled in the image, some of these twins are in the $(111)_{fcc}Cu||(110)_{bcc}Nb$ epitaxial orientations (labeled as E), while others are not (labeled as N). Instead the volumes labeled N are oriented with the $\sim(3\bar{1}1)_{fcc}Cu||(110)_{bcc}Nb$. It is possible that these non-epitaxial orientations occur as a result of strain accommodation. The small twins exist with thicknesses up to $\sim$12 nm, beyond which large single $(111)_{fcc}$ variants exist over the remaining breadth of the 100 nm Cu layer.

A cross-sectional HRTEM image of the Cu-Py interface in the Cu/Py/FeMn multilayer is shown in figure 6.16. The interface between the Cu and Py is just barely distinguishable. The interface between the Cu and Py is relatively sharp and flat. Both layers display epitaxial morphology. The lattice planes grow continuously from Cu layer to Py layer. Selected HRTEM images and corresponding FFT diffractograms of Cu and Py are shown in figure 6.17. Both diffraction patterns are characterized by 55° and 70° interplanar angles, indicating <110> zone axes of fcc Cu and $L1_2$ Py. In both cases, the growth direction is near <111>, suggesting the close packed planes are epitaxial in the fcc Cu and Py. The {111} interplanar spacings were measured to be 0.21 nm for Cu and 0.20 nm for Py, which correspond to fcc lattice parameters of 0.36 nm (a_{Cu} = 0.361 nm in the Cu bulk state) and 0.35 nm (a_{Py} = 0.355 nm in the Py bulk state), respectively.
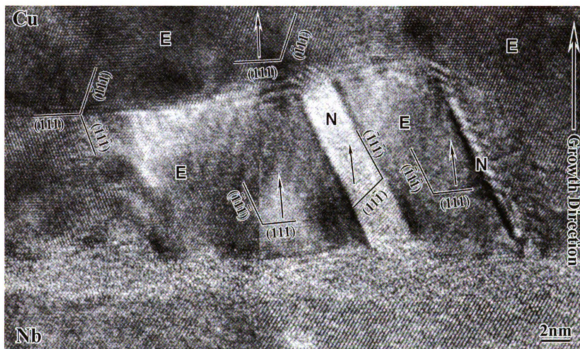
Figure 6.15 A cross-sectional HRTEM image of the Cu-Nb interface showing multiple small twin variants near the nucleation interface in the Cu layer of the Cu/Py/FeMn multilayer. Note that the regions labeled as E are oriented along $(111)_{fcc} \parallel (110)_{bcc}$ while those labeled N are not.
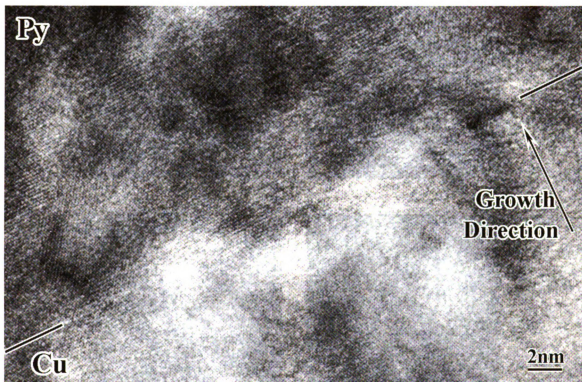
Figure 6.16 A cross-sectional HRTEM image of the Cu-Py interface in the Cu/Py/FeMn multilayer. The bars indicate the Cu-Py interface.
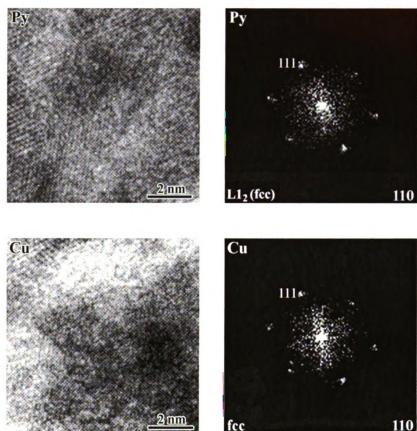
Figure 6.17 Selected HRTEM images and corresponding FFT diffractograms of Cu and Py showing <110> zones with growth planes of {111}.

6.5.3 Nb//Cu/Co/(Cu/Co)₂₀//Au/Nb/Au Multilayer (28-3)

In the (Cu/Co)×20 multilayer, high quality single crystal $(1\bar{1}0)$ Nb also grew epitaxially on the $(11\bar{2}0)$ Al_2O_3 substrate. Again the interface is found to be sharp, flat, and defect free. A cross-sectional HRTEM image of the Cu-Co bilayers in the (Cu/Co)×20 multilayer is shown in figure 6.18. Somewhat surprisingly, a contrast modulation between the Cu and Co layers is observed. Because Cu and Co have similar atomic scattering factors (as their atomic numbers differ only by 2), this contrast is not expected from differential scattering and the source of the contrast is not clear. However, the modulation period is consistent with the nominal thicknesses of the Cu (2.0 nm) and Co (1.5 nm) layers. The enlarged HRTEM images and corresponding FFT diffractograms shown in figure 6.19 indicate that both the Cu and Co are fcc. This is consistent with EBSP results [92] and prior studies on Co films [93], which reported that Co takes on an fcc structure rather than the bulk equilibrium hcp structure for thin films. However, the HRTEM results here show that the growth planes of both the Cu and Co in this (Cu/Co)×20 multilayer are {100} rather than the close packed {111} planes.

6.5.4 Nb//Cu/Py//Nb Multilayer (43-2)

A cross-sectional HRTEM image of the $(Nb_{250}//Cu_{20}/Py_{20}//Nb_{20})_{nm}$ multilayer with Cu deposited at 150°C and rest of the layers deposited at room temperature, is shown in figure 6.20. The bottom Nb, the Cu buffer layer, and the Py layer all display a single orientation throughout the entire area of the imaged cross-section sample. The top Nb displays a polycrystalline morphology with columnar grains. The interface between Cu and bottom Nb is relatively sharp, flat, and smooth. Although the interface between
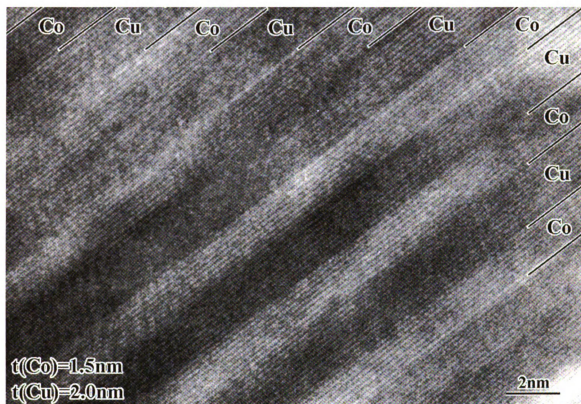
Figure 6.18 A cross-sectional HRTEM image of the Cu-Co bilayers in the (Cu/Co)×20 multilayer. Note that the observed Cu-Co periodicity is consistent with the nominal layer thicknesses.
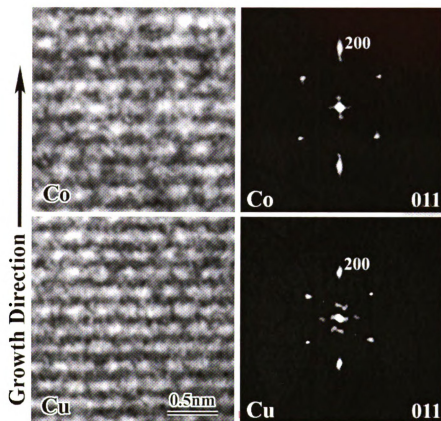
Figure 6.19 Selected HRTEM images and corresponding FFT diffractograms of Cu and Co showing <110> zones (slightly off axis) with growth planes of {100}.
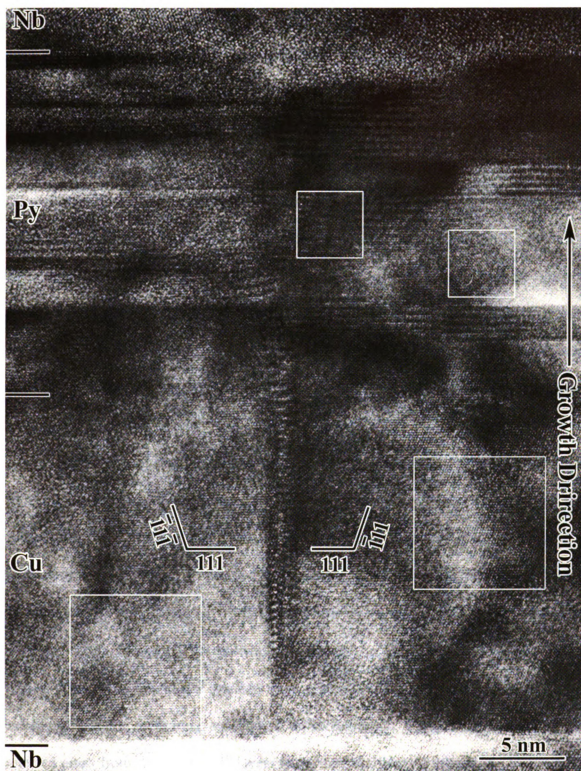
Figure 6.20 A cross-sectional HRTEM image of the $(Nb_{250}//Cu_{20}/Py_{20}//Nb_{20})_{nm}$ multilayer with Cu deposited at 150°C and rest of the layers deposited at room temperature.

the Cu and Py is not as evident as the Cu-Nb interface, it is distinguishable. It can be seen that the lattice planes grow continuously from the bottom Nb contact to the Cu buffer layer and up to the Py layer. The Cu layer displays a high quality epitaxial morphology with the Nb contact layer. It is evident from HRTEM observations that the Cu displays two orientation variants separated by a narrow slab which is perpendicular to the growth planes and starts from the bottom of Cu layer through into the Py layer. This narrow slab is an incoherent twin boundary between two single crystals of Cu. In the Py layer, there are some dark contrast variations running perpendicular to the growth direction. These areas occupied more than 50 percent of total observed Py cross-sectional areas and averaged about 10 nm in width. Given an approximate foil thickness of 10 nm, it is not surprising that these fringes appear in about 50% of the viewable cross-section.

For FFT analysis in this sample, the Nb reflections were used as internal calibration standards to determine the effective camera lengths for interpreting the subsequent FFT diffractograms. The enlarged HRTEM image and corresponding FFT diffractogram of bottom Nb is shown in figure 6.21. The interplanar angles are characterized by 60°, indicating a <111> zone axis of bcc Nb. The growth direction is close to <110>, indicating the growth has occurred on the closest packed bcc {110} planes. The {110} interplanar spacings were used as a standard to calculate an effective camera length for measuring subsequent diffractograms. Using this Nb calibration, selected areas from the Cu and Py layers have been analyzed as following. Figure 6.22 shows the HRTEM images from selected areas (labeled and indicated in figure 6.20) and corresponding FFT diffractograms of the Cu buffer layer. Figure 6.22 (a), (b), and (c)
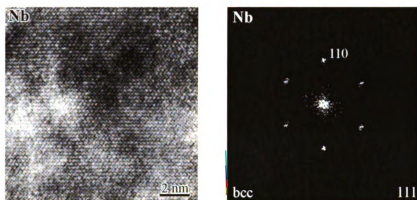
Figure 6.21 An enlarged HRTEM image and corresponding FFT diffractogram of the bottom Nb showing <111> zone axis of bcc Nb.

Figure 6.22 The HRTEM images from selected areas (a) from left side (b) from right side (c) twin boundary and corresponding FFT diffractograms of the Cu buffer layer showing <110> zones with growth planes of {111}.

correspond to the left side, the right side, and the twin boundary area of Cu. In figure 6.22 (a) and (b), both diffraction patterns were characterized by 55° and 70° interplanar angles, indicating <110> zone axes of fcc Cu. In both cases, the growth direction is near <111>, suggesting the close packed planes are epitaxial in the fcc Cu. The {111} interplanar spacings were measured to be 0.21 nm, which correspond to fcc lattice parameters of 0.36 nm (a_{Cu} = 0.361 nm for the Cu bulk state). In figure 6.22 (c) which corresponds to the area around the twin boundary between the two single grains of Cu, the FFT diffractogram shows the twin reflections with two common spots in growth direction. The interplanar spacing of these two common spots is calculated to be 0.21 nm, which corresponds to the {111} planes of fcc Cu. The resolvable zones of these twin spot patterns are characterized by 55° and 70° interplanar angles, indicating two <110> zone axes of fcc Cu with two common {111} reflections. These patterns show that the (111) close packed planes in the fcc Cu are epitaxial growth with the {110} closest packed planes in the bcc Nb and display two Σ3 twin variants corresponding to different stacking orders of {111} fcc planes, *i.e.* ABCABC versus ACBACB (as indicated in figure 6.20), consistent with the EBSP results from the thick films.

The HRTEM images from selected areas (indicated in figure 6.20) and the corresponding FFT diffractograms of Py layer are shown in figure 6.23. In some areas, the Py layer displayed epitaxial growth with their equilibrium phases as shown in figure 6.23 (a). FFT analysis shows that the diffractograms of these areas are <110> zone patterns and the growth planes are {111}, indicating the close packed {111} planes in the $L1_2$ Py are epitaxial growth with the {111} close packed planes in the fcc Cu. However

146
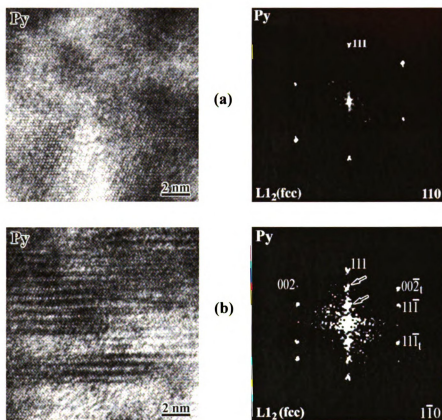
Figure 6.23 Selected HRTEM images and corresponding FFT diffractograms of Py showing (a) <110> zone with growth planes of {111} (b) a periodic lattice contrast with the interval of three {111} planes. The additional reflections at 1/3 and 2/3 of the primary (111) reflection spacings are indicated by arrows.

in some other areas as shown in figure 6.23 (b), a periodic lattice contrast with the three-layer interval running perpendicular to the growth direction is observed. The FFT diffractogram obtained from the periodic contrast region shows additional reflections (as indicated by arrows) at 1/3 and 2/3 of the primary (111) reflection spacings which are in the growth direction, and is consistent with the contrast modulation noted from HRTEM image. If the additional 1/3 and 2/3 reflection spots were ignored, the primary reflections are characterized as two <110> fcc patterns with two common {111} reflections similar with the one observed in Cu twin diffractogram.

6.6 DISCUSSION

6.6.1 The Effect of Growth Temperature and Post Deposition Annealing

The characterization results of the epitaxial magnetic multilayers and spin-valves demonstrated that the quality of the epitaxial growth of the Cu buffer layer is very temperature dependent. For example, in the first series of epitaxial samples (31-2, 27-3, and 28-3) poor epitaxial morphology was observed in all the samples when the Cu buffer layer was grown either at a low temperature (150°C) then post-annealed at a relatively high temperature (350°C), or when the buffer layer was grown at a relatively high temperature (350°C or 450°C) with no annealing. Loloee's AFM studies of similar samples have also shown that the surface topography is strongly affected by the temperature and surface quality of the substrates. In these studies, AFM images and line trace surface analyses show relatively smooth surfaces on 150 nm thick Cu films deposited at a substrate temperature of 475°C, and on 75 nm thick Cu films deposited at 150°C. However, all of the Cu films that were post-annealed displayed a rougher

surface. Therefore, based on this AFM study and the CTEM observations of the first series of epitaxial samples, a new series of samples was fabricated in order to fully determine the effect of temperature on epitaxial growth. Two samples were grown at a high deposition temperature (500°C) and two were grown at low deposition temperatures (100°C and 150°C). None of the samples was subjected to post-annealing. Following CTEM observations showed poor epitaxial morphology when Cu buffer layers were grown at 500°C. High quality epitaxial Cu buffer layers were obtained when Cu was grown at low temperatures (100°C and 150°C) without post annealing. Although the layers are smooth and continuous, significant contrast from faults and dislocations are observed. Ideally, one would like to reduce these. However, the results presented here indicate that annealing these layers to reduce the defects formed in sputtering is problematic, with post-sputtered annealing samples showing agglomeration. However, all of these post-sputtering annealing treatments occurred after the Cu was sputtered, but before any additional layers were laid down on the Cu. It might be possible to reduce the defects by annealing after capping layers are applied.

6.6.2 Overlapping Twins in Py

The three-layer periodic contrast observed in the epitaxial Py layer is somewhat surprising, although this kind of the contrast is not unusual and has been found and studied in other materials by many groups. Bender et al. [93] reported seeing triple periodicity along the [111] direction in very high dose phosphorus ion-implanted (011) Si wafers. This phenomenon was explained using the model of overlapped twins by

simulating the high resolution electron microscopic images with the real space method. Hutchison, et al. [95] and Vanhellemont, et al. [96] also observed the similar twinning structures in Si crystals by different techniques. A similar model to explain the same phenomenon in Au films was proposed by Hashimoto et al. [97]. Wu et al. observed triple periodicity in GaAs crystalline film grown on Si substrates by the MBE method [98]. They explained this periodicity by an overlapped twins model which was confirmed by image matching between observed HRTEM images and simulations using the multi-slice method. Abe et al. [99] reported three-fold periodicity of {111} in massively transformed γ-TiAl alloys and concluded that the contrast is caused by overlapping twin related crystals along the incident beam direction. An example of this three-layer periodic contrast in γ-TiAl alloys [99] is shown in Figure 6.24. It can be seen clearly from the HRTEM image shown in figure 6.24 (a) that the contrast corresponds to the periodic contrast of intervals of three close-packed $\{111\}_\gamma$ planes. The periodicity gives rise to extra reflections at positions of 1/3 and 2/3 of the primary $\{111\}_\gamma$ spot as indicated by the arrows in the FFT diffractogram in the inset of figure 6.24 (b). Figure 6.25 shows an enlargement of the framed part in figure 6.24 and simulated images of the overlapping twins. The simulations confirm that the contrast is due to double diffraction caused by overlapping twin-related crystals along the incident beam direction.

In this study, the HRTEM images and corresponding FFT diffractograms of Py show similar contrast and periodicity as those mentioned above. To explain this phenomenon in more detail, a schematic illustration of the overlapping twin model of Py is shown in figure 6.26. The projections of atoms of Py (NiFe) single crystal are along the [110] direction for twins of two stacking orders of {111} fcc planes, i.e. ABCABC
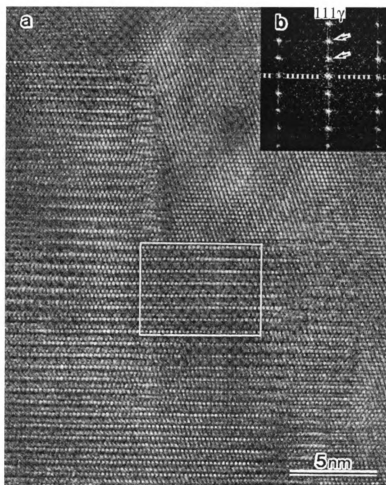
Figure 6.24 (a) A cross-sectional HRTEM image showing a periodic contrast with the three-layer interval and (b) its corresponding Fourier transform of the image in the massively transformed γ grain [99].
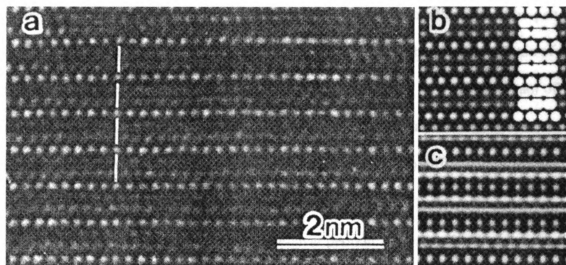
Figure 6.25 (a) Enlargement of the framed part of figure 5.24. Simulated images of the overlapping twins (b) for the total thickness of 4 nm at $\Delta f = -60$ nm and (c) for the total thickness of 16 nm at $\Delta f = -75$ nm [99].

versus ACBACB. The black and white dots indicate atoms of Fe and Ni respectively. When the atomic arrangements of these two planes are superimposed on each other as shown in figure 6.26 (b), it can be seen that the atom positions of both crystals become coincident with each other at every third plane as indicated by the arrows. The resulting periodicity is in good agreement with the HRTEM image of Py in figure 6.23. For this overlapping twin situation, Abe et al. [99] depicted the corresponding diffraction pattern as shown in figure 6.27 (a) which consists of reflections with the [110] zone axis of the matrix and its twin. The pattern is in good agreement with the FFT diffractogram of Py in figure 6.27 (b). The additional two reflections indicated by arrows are due to double diffraction. For example, the 1/3 spot can be the result of (002) diffraction of the matrix double diffracting with the ($11\bar{1}$) reflection of the twin. Therefore based on these comparisons, we can conclude that the three-layer periodic contrasts observed in epitaxial Py layer results from overlapped twins.

6.7 SUMMARY

The microstructure of the epitaxial magnetic multilayers and spin-valves using sputter deposition were characterized by CTEM and HRTEM.

The CTEM observations suggest that the quality of good epitaxial growth of Cu buffer layers depends strongly on deposition temperatures and post annealing. Poor epitaxial morphology was observed when Cu was grown either at low temperatures with post annealing or at high temperatures without annealing. The high quality of epitaxial Cu buffer layer was obtained when Cu was grown at low temperatures (100°C and
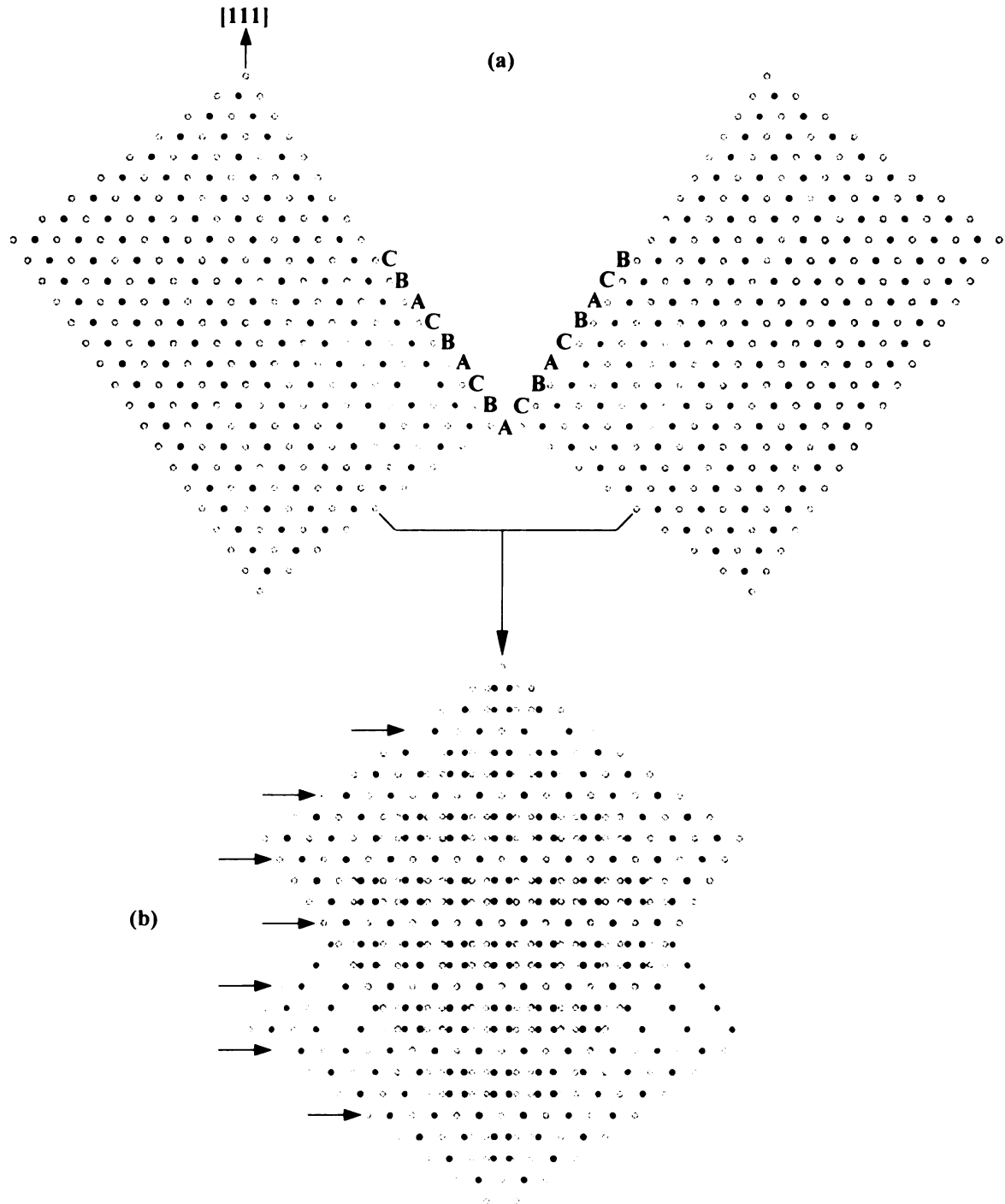
Figure 6.26 Schematic illustrations of the overlapping twin model to explain the periodic contrast with the three-layer interval. (a) A projection of atoms along the [1 1̄ 0] direction of the twin-related Py single crystal. (b) Two Py crystals superimposed to each other showing the atom positions of both crystals become coincident with each other at every third plane as indicated by arrows.
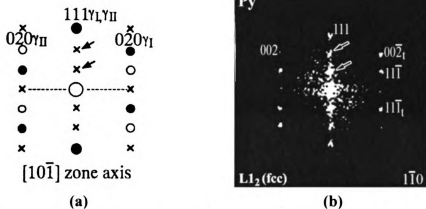
Figure 6.27 (a) Schematic illustration of the expected electron diffraction pattern from superimposed overlapping twin model in γ-TiAl [99] (b) The FFT diffractogram of the epitaxial Py showing overlapping twin reflections.

150°C) without post annealing. The diffraction patterns show that twin variants appear in epitaxial Cu and Py layers, consistent with EBSP results on thick films.

The HRTEM images revealed that the Cu buffer layer grown at 150°C appear as twin variants with two stacking sequences of {111} fcc planes, which is in agreement with CTEM observations. The three-layer periodic contrast observed in Py can be explained by overlapped twins along [110] direction with {111} twin planes.

CHAPTER VII

SUMMARY AND CONCLUSIONS

In this chapter, the structural studies of polycrystalline and epitaxial GMR magnetic multilayers and spin-valves will be summarized and the key experimental results from this research work will be drawn together. Furthermore, some areas for further research are outlined, including analytical analysis and growth of full epitaxial GMR multilayers and associated MR evaluation studies.

7.1 SUMMARY AND CONCLUSIONS

In order for the GMR effect in magnetic multilayers and spin-valves to be utilized for existing and potential technological applications in sensors and magnetic devices, a complete understanding of the relationships between processing, structure, and behavior is necessary. Previous works [5,62] have found that the GMR effect depends on structure at the micro and atomic level, including interfacial or layer roughness, layer quality, and layer orientation. Therefore, to gain a full understanding of the GMR effect, the initial motivation of this study was to characterize the interfacial structures of polycrystalline spin-valves using cross-sectional CTEM and HRTEM.

The first key experimental result was the finding of non-equilibrium bcc structures in the Cu/Py spin-valves in addition to the equilibrium fcc structures of Cu, FeMn, and $L1_2$ Py layers, as described in detail in Chapter III. In the Cu/Py spin-valves, structures with different Py thicknesses sputtered at different temperatures were characterized using CTEM and HRTEM complemented with HRTEM image simulations

157

and FFT analysis techniques. All of the spin valves displayed polycrystalline structures with columnar grains. The grains grew on close packed planes ({111} planes in the bcc Nb contacts and {110} planes in the fcc Cu, FeMn, and Py spin-valve layers) taking up a near Kurdjumov-Sachs $\{111\}_{fcc}//\{110\}_{bcc};<110>_{fcc}//<111>_{bcc}$ orientation relationship. FFT analysis and HRTEM image simulations indicate that in some of the columnar grains, the Cu, FeMn, and Py regions take up non-equilibrium bcc structures, regardless of a difference in layer thicknesses and sputtering temperatures. In this non-equilibrium case, the bcc Cu, FeMn, and Py layers grew on the {110} closest packed planes and were epitaxial with the Nb contacts.

Chapter IV discussed interesting results in polycrystalline Ag/Py spin-valves. In one instance, when the Ag/Py spin-valve was grown directly on the Si substrate, the first Ag layer grew as an epitaxial single crystal although the remaining layers displayed the expected polycrystalline morphology. HREDS has shown that this single crystal (epitaxial) layer is likely composed of Ag and In in a 4:1 atomic ratio. The In contamination may be due to the inadvertent sputtering or evaporation of target solder in the sputtering system prior to the Nb contact deposition. Indium contamination was only observed in this one sample. If reproducible, this epitaxial Ag_4In may be useful as a seed layer for growth of different epitaxial spin valves or other structures on Si substrates. In all of the other Ag/Py spin-valve samples examined to date, polycrystalline morphologies have been consistently observed regardless of substrate.

In agreement with polycrystalline Cu/Py and Ag/Py CTEM observations, Cu/CoZr spin valves are polycrystalline with columnar grains for both exchange biased spin valve (EBSV) and hybrid spin valve. Some defects, including dislocations, stacking

158

faults, and Moiré fringes, are observed in both spin valves. However, in comparison to some previous polycrystalline EBSVs, the columns in the hybrid spin valve appear to grow straight up with uniform width.

Because of the various non-equilibrium phases that were found in polycrystalline Cu/Py and Ag/Py spin-valves, and because of the difficulties in imaging interfaces in polycrystalline samples, the initial objective of this study was modified to focus on the interfacial structures in epitaxial multilayers to diminish the effect of structural defects associated with grain boundaries. By minimizing such defects, assessment of the interfacial structures should be facilitated. Furthermore, elimination of these defects should allow more fundamental CPP studies to be carried out. However, as the program progressed, it became clear that growing such samples was not a trivial matter. Thus, the final objective of this study was to assess structures of epitaxially grown samples using a sputter deposition technique.

The major achievement of the epitaxial samples study was the successful growth of a high quality Cu buffer layer on the epitaxial Nb contact, as detailed in Chapter VI. In this study, the CTEM observations suggest that the quality of good epitaxial growth of Cu buffer layers depends strongly on deposition temperatures and post annealing. Poor epitaxial morphology was observed when Cu was grown either at low temperatures with post annealing or at high temperatures without annealing. High quality epitaxial Cu buffer layers were obtained when the Cu layer was grown at low temperatures (100°C and 150°C) without post annealing. The corresponding diffraction patterns show that twin variants appear in epitaxial Cu and Py layers, consistent with EBSP results from thick films. The HRTEM images revealed that the Cu buffer layer grown at 150°C

appears as twin variants with two stacking sequences of {111} fcc planes, which is in agreement with CTEM observations. The three-layer periodic contrast observed in Py can be explained by overlapped twins along [110] direction with {111} twin planes. Those areas occupied more than 50 percent of total observed Py cross-sectional areas. These fine twin variants may not in themselves affect CPP measurements. However, they will be separated by incoherent twin boundaries in the growth direction which might result in some electron scattering.

With the extensive structural characterization of polycrystalline Cu/Py, Ag/Py, and Cu/CoZr, and epitaxial GMR magnetic multilayers and spin valves, new insights into the layer structures have been achieved. In particular, the parameters for growing a high quality epitaxial Cu and Py layers on Nb contact layers (required for GMR measurements with CPP geometry), which is the foundation for growing subsequent epitaxial films in a preferred orientation, have been established. This success confirms the validity of the sputter deposition technique for growing quality epitaxial thin films at high rates and presents a greater opportunity for designers and manufactures to realize further applications of epitaxial GMR devices.

Furthermore, the unique combination of this research with Loloee's study [33] on magnetic and magneto-transport properties of these materials has led to a more comprehensive understanding of the relationship between microstructures and magnetic properties associated with the GMR effect. One of the advantages of using epitaxial samples over polycrystalline ones is that they afford the capability of studying the magnetic anisotropy (in particular, magnetocrystalline anisotropy) and determining the direction of easy magnetic axis in the ferromagnetic layers. In particular for spin valves,

knowing the direction of easy axis and magnetocrystalline anisotropy can lead to stronger pinning between the antiferromagnetic and ferromagnetic layers by application of an external magnetic field along the direction of easy axis during the pinning process. Also, knowing the direction of easy axis in both hybrid and exchanged biased epitaxial spin-valve samples would allow establishing true parallel and antiparallel states. Another important advantage of epitaxial samples is that the grain boundary effect is greatly reduced. For polycrystalline samples, even in a small unit area, because of the large number of grains and corresponding grain boundaries, there will be many magnetic domains, which will have an effect on electron scattering for CPP measurements. Whereas for epitaxial samples, only large twins and single crystals are present. CPP measurements that use the optical-lithography-based sample preparation technique [100] provide a cross-sectional pillar of 2×2 μm area, which is even smaller than the average twin variant size. In this case, grain boundaries may not exist at all in the cross-section areas. Therefore, there would be no electron scattering caused by grain boundaries (as compared to the polycrystalline case) and the magnetic domains would extend across the width of the pillars.

These research results should further enhance the knowledge of the mechanisms of magnetic multilayer structures and establish a theoretical basis for GMR application in the fields of sensors and information storage devices.

7.2 FUTURE STUDIES

Analytical Analysis:

In this research study, a number of electron microscopy techniques were used to assess the layer structures and growth characteristics of GMR magnetic multilayers and spin valves. However, no one technique can provide a comprehensive measurement of all of the important characteristics of multilayer structures. Scanning transmission electron microscopy (STEM) Z-contrast imaging combination with analytical techniques as microdiffraction, electron energy loss spectroscopy (EELS), and high resolution energy dispersive x-ray spectroscopy (HREDS) is a powerful tool to assess the nanoanalytical results from the multilayer samples. This technique can provide chemical information of individual components at atomic resolution to determine if there is intermixing or interdiffusion occurring at the interfaces. In particular, Z-contrast with EELS should be able to achieve characterization of the interfaces, allowing assessment of the degree of interfacial mixing or roughness.

During the period of this study, access was not available to this type of analytical instrumentation. However, in the near future a new advanced analytical TEM/STEM with Z-contrast and EELS capabilities will be installed on the MSU campus. This new capability should assist in further characterization of the chemical nature of these materials.

Epitaxial Growth:

The successful growth of the epitaxial films by the sputter deposition technique has opened up remarkable possibilities for making epitaxial GMR devices at higher growth rates and lower costs. It may also provide unique electronic or magnetic properties in comparison to existing devices made by polycrystalline materials by eliminating defects that scatter electrons. This thesis demonstrated the feasibility of

162

growing high quality epitaxial layers. It should not be difficult to grow full epitaxial spin valves and multilayers from this foundation. Even in the samples that did not have good epitaxial Cu buffer layers, the remaining layers typically epitaxed well. Furthermore, the results presented here should provide a foundation for determining the fabrication variables which are necessary to improve the quality of epitaxial growth of GMR magnetic multilayers.

REFERENCES

[1] H. Sato, P.A. Schroeder, J.M. Slanghter, W.P. Pratt, Jr., and W. Abdul-Razzaq, *Superlattices Microstruct.* **4**, 45 (1987).

[2] E. Vélu, C. Dupas, D. Renard, J.P. Renard, and J. Seider, *Phys. Rev.* **B37**, 668 (1988).

[3] M.N. Baibich, J.M. Broto, A. Fert, F. Nguyen Van Dau, F. Petroff, P. Etienne, G. Creuzet, A. Friederich, and J. Chazelas, *Phys. Rev. Lett.* **61**, 2472 (1988).

[4] G. Binasch, P. Grünberg, F. Saurenbach, and W. Zinn, *Phys. Rev.* **B39**, 4828 (1989).

[5] B. Dieny, *J. of Magn. Magn. Mater.* **136**, 335-359 (1994).

[6] S.S.P. Parkin, *IBM J. Res. Dev.* **42**, no. 1, 3 (1998).

[7] C.H. Smith and R. W. Schneider, *Proceedings Sensors Expo Boston*, 139 (1997).

[8] J.M. Daughton, *J. of Magn. Magn. Mater.* **192**, 334 (1999).

[9] A. Barthelemy, *Phys. World. Nov.*, 35 (1994).

[10] B. Dieny, V.S.Speriosu, S.S.P. Parkin, B.A. Gurney, D.R. Wilhoit, and D. Mauri, *Phys. Rev.* **B43**, 1297 (1991).

[11] B.Dieny, V.S. Speriosu, B.A. Gurney, S.S.P. Parkin, D.R. Wilhoit, K.P. Roche, S. Metin, D.T. Peterson, and S. Nadimi, *J. Magn. Magn. Mater.* **93**, 101 (1991).

[12] A. Barthelemy, A.Fert, M.N. Baibich, P. Etienne, S. Lequien, and R. Cabanol, *J. Appl. Phys.* **67**, 5908 (1990).

[13] M. Pardavi-Horvath, *Magnetic Multilayers*, 355 (1994).

[14] P.M. Levy, *Solid State Physics* **47**, 367 (1994).

[15] W.P. Pratt, Jr., S.F. Lee, J.M. Slanghter, R. Loloee, P.A. Schroeder, and J. Bass, *Phys. Rev. Lett.* **66**, 3060 (1990).

[16] S.S.P. Parkin, N. More, and K.P. Roche, *Phys. Rev. Lett.* **64**, 2304 (1990).

[17] D.H. Mosca, F. Petroff, A. Fert, P.A. Schroeder, W.P. Pratt, and R. Loloee, *J. Magn. Magn. Mater.* **94**, L1 (1991).

[18] S.S.P. Parkin, R. Bhadra, and K.P. Roche, *Phys. Rev. Lett.* **66**, 2152 (1991).

[19] F. Petroff, A. Barthelemy, D.H. Mosca, D.K. Lottis, A. Fert, P.A.Schroeder, W.P. Pratt, R. Loloee, and S. Lequien, *Phys. Rev.* **B44**, 5355 (1991).

[20] S.S.P. Parkin, *Appl. Phy. Lett.* **60**, 512 (1992).

[21] B. Rodmacq, G. Palumbo, and Ph. Gerard, *J. Magn. Magn. Mater.* **118**, L11 (1993).

[22] T. Kai, K. Shiiki, *J. Magn. Magn. Mater.* **195**, 537 (1999).

[23] B. Dieny, V.S.Speriosu, S. Metin, S.S.P. Parkin, B.A. Gurney, P. Baumgart, and D.R. Wilhoit, *J. Appl. Phys.* **69**, 4774 (1991).

[24] V.S. Speriosu, B. Dieny, J.P. Nozières, B.A. Gurney, P. Humbert, H. Lefakis, P. Baumgart, and D.R. Wilhoit, *Digests INTERMAG '92*, St. Louis, paper CA-04.

[25] B. Dieny, V.S. Speriosu, J.P. Nozieres, B.A. Gurney, A. Vedyayev, and N. Ryzhanova, in: *Magnetism and Structure in Systems of Reduced Dimension*, eds. R. Farrow et al., *NATO ASI Ser. B: Physics* v. 309, (Plenum Press, NY 1993).

[26] B. Dieny, V.S. Speriosu, and S. Metin, *Europhys. Lett.* **15**, 227 (1991).

[27] B. Dieny, P. Humbert, V.S. Speriosu, and B.A. Gurney, *Phys. Rev.* **B45**, 806 (1992).

[28] B. Dieny, *Europhys. Lett.* **17**, 261 (1992).

[29] V.S. Speriosu, B. Dieny, P. Humbert, B.A. Gurney, and H. Lefakis, *Phys. Rev.* **B44**, 5358 (1991).

[30] B. Dieny, V.S. Speriosu, J.P. Nozières, and B.A. Gurney, *Appl. Phys. Lett.* **61**, 2111 (1991).

[31] T.C. Huang, J.P. Nozières, V.S. Speriosu, B.A. Gurney, and H. Lefakis, *Appl. Phys. Lett.* **62**, 1478 (1993).

[32] S.S.P. Parkin, *Phys. Rev. Lett.* **71**, 1641 (1993).

[33] R. Loloee, Ph.D. Dissertation, Michigan State University (2000).

[34] W.P. Pratt Jr., S.D. Steenwyk, S.Y. Hsu, W.-C. Chiang, A.C. Schaefer, R. Loloee, and J. Bass, *IEEE Transactions on Magn.* **33**, 3505 (1997).

[35] Y. Bruynseraede, K. Temst, R. Schad, C.D. Potter, P. Belien, G. Verbanck, G. Gladyszewski, J. Barnas, M. Baert, V.V. Metlushko, M.J. Van Bael, V.V. Moshchalkov, *Thin Solid Film* **275**, 1 (1996).

[36] V.S. Speriosu, J.P. Nozières, B.A. Gurney, B. Dieny, T.C. Huang, and H. Lefakis, *Phys. Rev.* **B47**, 11579 (1993).

[37] M.C. Cyrille, S. Kim, M.E. Gomez, J. Santamaria, Kannan M. Krishnan, and Ivan K. Schuller, *Phys. Rev.* **B62**, 3361 (2000).

[38] M.C. Cyrille, S. Kim, M.E. Gomez, J. Santamaria, C. Leighton, Kannan M. Krishnan, and Ivan K. Schuller, *Phys. Rev.* **B62**, 15079 (2000).

[39] F. Petroff, A. Barthelemy, A. Fert, P. Etienne, and S. Lequien, *J. Magn. Magn. Mater.* **93**, 95 (1991).

[40] E.E. Fullerton, D.M. Kelly, J. Guimpel, I.K. Schuller, and Y. Bruynseraede, *Phys. Rev. Lett.* **68**, 859 (1992).

[41] Y. Obi, K. Takanashi, Y. Mitami, N. Tsuda, and H. Fujimori, *J. Magn. Magn. Mater.* **104-107**, 1747 (1992).

[42] S.S.P. Parkin, *Appl. Phys. Lett.* **58(23)**, 2710 (1991)

[43] F. Petroff, A. Barthelemy, A. Fert, P. Etienne, and S. Lequien, *J. Magn. Magn.*

Mater. **104-107**, 1712 (1992).

[44] S. Pizzini, F. Baudelet, D. Chandesris, A. Fontaine, H. Magnan, J.M. George,

F. Petroff, A. Barthelemy, A. Fert, R. Loloee and P.A. Schroeder, *Phys. Rev.* **B46**,

1253 (1992).

[45] R. Nakatani, T. Dei, and Y. Sugita, *Jpn. J. Appl. Phys.* **31**, L1417 (1992).

[46] R. Nakatani, T. Dei, and Y. Sugita, MMM'92, EQ04.

[47] R. Jungblut, R. Coehoorn, M.T. Johnson, J. aan de Stegge, and A. Reinders, *J. Appl. Phys.* **75(10)**, 6659 (1994).

[48] T. Shinjo, in: *Magnetism and Structure in Systems of Reduced Dimension, eds. R. Farrow et al., NATO ASI Ser. B: Physics* 309, 323 (Plenum Press, NY 1993).

[49] A. Vedyayev, B. Dieny, N. Ryzhanova, J.B. Genin, and C. Cowache, *Europhys. Lett.* **25**, 465 (1994).

[50] W.F. Egelhoff Jr., T. Ha, R.D.K. Misra, C.J. Powell, M.D. Stiles, R.D. McMichael, C.-L. Lin, J.M. Sivertsen, J.H. Judy, *J. Appl. Phys.* **79**, 282 (1996).

[51] M.E. Gomez, J. Santamaria, M.C. Cyrille, E.C. Nelson, Kannan M. Krishnan, and Ivan K. Schuller, (submitted to *Phys. Rev. B*).

[52] B. Heinrich, M. From, J.F.Cochran, L.X. Liao, Z. Celinski, C.M. Schneider, and K. Myrtle, *Mat. Res. Soc. Symp. Proc.* **313**, 119 (1993).

[53] Z. Celinski and B. Heinrich, *J. Magn. Magn. Mater.* **99**, L25 (1991).

[54] R. Loloee, M.A. Crimp, W. Zhu, and W.P. Pratt Jr., *Mat. Res. Soc. Symp. Proc.* **528**, 203 (1998).

[55] R.D.K. Misra, T. Ha, Y. Kadmon, C. J. Powell, M.D. Stiles, R.D. McMichael, and W.F. Egelhoff, Jr., *Mat. Res. Soc. Symp. Proc.* **384**, 373 (1995).

[56] M. Chladek, V. Valvoda, C. Dorner, and W. Ernst, *J. Magn. Magn. Mater.* **172**, 209 (1997).

[57] J.P. Deville, A. Barbier, C. Boeglin, and B. Carriere, *Mat. Res. Soc. Symp. Proc.* **313**, 519 (1993).

[58] H. Geng, J.W. Heckman, R. Loloee, W.P. Pratt, Jr., J. Bass, and M.A. Crimp, *Mat. Sci. and Eng.* **B86**, 245 (2001).

[59] K. Sumiyama, T. Hihara, S.A. Makhlouf, K. Wakoh, M. Sakurai, Y. Xu, T.J. Konno, S.Yamamuro, and K. Suzuki, *Mat. Sci. and Eng.* **A217/218**, 340 (1996).

[60] F.M. Ross, K.M. Krishnan, N. Thangaraj, R.F.C. Farrow, R.F. Marks, A. Cebollada, S.S.P. Parkin, M.F. Toney, M. Huffman, C.A. Paz De Araujo, L.D. McMillan, J. Cuchiaro, M.C. Scott, C. Echer, F. Ponce, M.A. O'Keefe, and E.C. Nelson, *MRS Bulletin*, 17 (1996).

[61] P. Galtier and T. Valet, *Mat. Res. Soc. Symp. Proc.* **475**, 131 (1997).

[62] P. Bayle-Guillemaud, A.K. Petford-Long, T.C. Anthony, J.A. Brug, *IEEE Trans. On Magn.* **32**, No. 5, 4627 (1996).

[63] H. Geng, J.W. Heckman, W.P. Pratt, Jr., J. Bass, F.J. Espinosa, S.D. Conradson, D. Lederman, and M.A. Crimp, *J. Appl. Phys.* **86**, 4166 (1999).

[64] S.D. Steenwyk, S.Y. Hsu, R. Loloee, J. Bass, and W.P. Pratt, Jr., *J. Appl. Phys.* **81** (8), 4011 (1997).

[65] A.Romano, J. VanHellemont, H. Bender, and J.R. Morante, *Ultramicroscopy*, **31**, 183 (1989).

[66] A.Romano, J. VanHellemont, and H. Bender, *Mat. Res. Soc. Symp. Proc.*, **199**, 167 (1990).

[67] F. Shaapur and M. Park, *Mat. Res. Soc. Symp. Proc.*, **199**, 177 (1990).

[68] D.A. Howell, Master Thesis, Michigan State University (1995).

[69] D.B. Williams and C.B. Carter, *Transmission Electron Microscopy:* A textbook for materials science, Plenum Press, NY (1996).

[70] W.S. Rasband and D.S. Bright, *Microbeam Anal. Soc. J.* **4**, 137 (1995).

[71] P. Stadelman, *Ultramicroscopy* **21**, 131 (1987).

[72] K.L. Merkle, *Ultramicroscopy* **37**, 130 (1991).

[73] D.J. Smith, W.J. DeRuijter, M.R. McCartney, and J.K. Weiss, *Ultramicroscopy* **52**, 591 (1993).

[74] Z. Nishiyama, *Sci. Rept. Tohoku Univ.* **23**, 368 (1934).

[75] G. Wasserman, *Arch. Eisenhuttenwesen* **16**, 647 (1933).

[76] G.V. Kurdjumov and G. Sachs, *Z. Physik* **64**, 325 (1939).

[77] M.G. Hall, H.I. Aaronson and K.R. Kinsman, *Surface Science* **31**, 257 (1972).

[78] J.M. Rigsbee and H.I. Aaronson, *Acta Metall.* **27**, 351 (1979).

[79] D.J. Smith, W.O. Saxton, M.A. O'Keefe, G.J. Wood and W.M. Stobbs., *Ultramicrosocpy* **11**, 263 (1983).

[80] A.T. Paxton, M. Methfessel and H.M. Potatoglou, *Phys. Rev.* **B41**(12), 8127 (1990).

[81] T.E. Mitchell, Y. C. Lu, A. J. Griffen Jr., M. Nastasi, and H. Kung, *J. Am. Ceram. Soc.* **80(7)**, 1673 (1997).

[82] S.R. Goodman, S.S. Brenner, and J.R. Low, Jr., *Met. Trans.* **4**, 2363 (1973).

[83] Heinrich, *et al., In science and technology of nanostructured Materials.*, G.C. Hadjipanayis and G.A. Prinz. eds. Plenum, NY. p15 (1991).

[84] H. Kung, Y-C. Lu, A.J. Griffen, Jr., M. Nastasi, T.E. Mitchell, and J.D. Embury,

Appl. Phys. Lett. **71** (15) 2103 (1997).

[85] P.M. Marcus, V.L. Moruzzi, Z.Q. Wang, Y.S. Li, and F. Jona, *Mat. Res. Soc. Symp. Proc.*, **83**, 21 (1987).

[86] C. Schmidt, F. Ernst, M.W. Finnis, and V. Vitek, *Phys, Rev. Lett.*, **75**, 2160 (1995)

[87] F. K. LeGoues, M. Liehre, M. Renier, W. Krakow, *Phil. Mag. B.* **57** (2), 179 (1988).

[88] J. Kudrnovsky, V. Drchal, I. Turek, C. Blaas, P. Weinberger, and P. Bruno, *J. Mater.* **52 (7)**, 29 (2000).

[89] M. R. Baren, in: T. B. Massalski (Ed.), *Binary Alloy Phase Diagrams*: 2nd ed., ASM International, Materials Park, OH, pp. 47-48 (1990).

[90] J.W. Heckman, Master Thesis, Michigan State University (2001).

[91] Z. Nishiyama, *Sci. Rept. Tohoku Univ.*, **23**, 368 (1934).

[92] R. Loloee, W.P. Pratt, Jr., and M.A. Crimp, *Phil. Mag. A,* **81** (2), 261 (2001).

[93] A.E.M. De Veirman, F.J.G. Hakkens, and A.G. Dirks, *Ultramicroscopy*, **51**, 306 (1993).

[94] H. Bender, A. De Veirman, J. Van Landuyt, and S. Amelinckx, *Appl. Phys. A,* **39**, 83 (1986).

[95] J.L. Hutchison, G.R. Booker, and M.S. Abrahams, *Inst. Phys. Conf. Ser.*, **60**, 139 (1981).

[96] J. Vanhellemont, J. Van Landuyt, C. Claeys, G. Declerck, H.H. Babbar, D.N. Nichols, and C. Anagnostopoulos, *Inst. Phys. Conf. Ser.*, **76**, 195 (1985).

[97] H. Hashimoto, H. Endoh, M. Tomita, N. Ajika, M. Kuwalara, Y. Hata, Y. Tubokawa, T. Honda, Y. Arada, S. Sakurai, T. Etoh, and Y. Yokota, *J. Electron. Microsc. Tech.*, **3**, 5 (1986).

[98] X.J. Wu, F.H. Li, and H. Hashimoto, *Phil. Mag. B,* **63 (4)**, 931 (1991).

[99] E. Abe, S. Kajiwara, T. Kumagai, and M. Nakamura, *Phil. Mag. A,* **75 (4)**, 975 (1997).

[100] R.D. Slater, J.A. Caballero, R. Loloee, and W.P. Pratt, Jr., *J. Appl. Phys.* **90** (10), 5242 (2001).